

**ADVANCED IMAGE ANALYSIS
TECHNIQUES FOR AUTOMATED
GLAUCOMA DIAGNOSIS USING RETINAL
FUNDUS IMAGES**

Ph.D. THESIS

by

SHISHIR MAHESHWARI



**DISCIPLINE OF ELECTRICAL ENGINEERING
INDIAN INSTITUTE OF TECHNOLOGY INDORE**

AUGUST, 2019

**ADVANCED IMAGE ANALYSIS
TECHNIQUES FOR AUTOMATED
GLAUCOMA DIAGNOSIS USING RETINAL
FUNDUS IMAGES**

A THESIS

*Submitted in partial fulfillment of the
requirements for the award of the degree
of*

DOCTOR OF PHILOSOPHY

by

SHISHIR MAHESHWARI



**DISCIPLINE OF ELECTRICAL ENGINEERING
INDIAN INSTITUTE OF TECHNOLOGY INDORE
AUGUST, 2019**



INDIAN INSTITUTE OF TECHNOLOGY INDORE

CANDIDATE'S DECLARATION

I hereby certify that the work which is being presented in the thesis entitled “**Advanced Image Analysis Techniques for Automated Glaucoma Diagnosis Using Retinal Fundus Images**” in the partial fulfilment of the requirements for the award of the degree of **Doctor of Philosophy** and submitted in the **Discipline of Electrical Engineering, Indian Institute of Technology Indore**, is an authentic record of my own work carried out during the time period from May 2015 to August 2019 under the supervision of Dr. Vivek Kanhangad, Associate Professor, and Prof. Ram Bilas Pachori, Professor, Indian Institute of Technology Indore, India.

The matter presented in this thesis has not been submitted by me for the award of any other degree of this or any other institute.


27/08/2019

Signature of the student with date
(**Shishir Maheshwari**)

This is to certify that the above statement made by the candidate is correct to the best of my knowledge.





27.08.2019

Signature of Thesis Supervisor(s) with date
(**Dr. Vivek Kanhangad**)
(**Prof. Ram Bilas Pachori**)

Shishir Maheshwari has successfully given his Ph.D. Oral Examination held on **13-July-2020**.





Type text here





13.07.2020

Signature of Chairperson (OEB)

Signature of External Examiner

Signature of Thesis Supervisor(s)

Date: 13/07/2020

Date: **13-7-2020**

Date:



Signature of PSPC Member #1

Date: 13/07/2020



Signature of PSPC Member #2

Date: **13/07/2020**



Signature of Convener, DPGC

Date: 13-07-2020



13/07/2020

Signature of Head of Discipline

Date:

ACKNOWLEDGEMENTS

I take this opportunity to acknowledge my heartfelt gratitude to all those people who have directly or indirectly helped me throughout my PhD candidature. First and foremost, I want to thank **Almighty God** for giving me the strength, knowledge, and enlightenment to undertake this research work. Then, I would like to express my sincere thanks to my supervisors, **Dr. Vivek Kanhangad** and **Prof. Ram Bilas Pachori**, for their valuable guidance and constant support during the entire PhD work. It has been an inspiring and a great learning experience for me throughout my doctoral work under their supervision at IIT Indore. Dr. Vivek Kanhangad, especially, provided helpful career advice and suggestions, extending beyond academic boundaries, whenever needed.

Next, I would like to express my sincere thanks to my comprehensive evaluation of research progress committee members **Dr. Trapti Jain** and **Dr. Surya Prakash** for their encouragement, insightful suggestions and valuable comments, which helped me in improving my research work. I want to thank all the faculty members and the staff at IIT Indore for their cooperation throughout my thesis work. I want to express my sincere gratitude to the **Ministry of Human Resource Development (MHRD)**, Government of India, for providing the teaching assistantship during my PhD work.

It was my privilege to share the space with the members of the **Pattern Recognition and Image Analysis (PRIA)** group and creating a friendly and conducive environment. I gratefully acknowledge the companionship of Dr. Ankita Jain, Dr. Telgam Setti Sunilkumar, Dr. Shruti Bhilare, Mahesh Gour, and Vijay Anand. I appreciate their trustworthy help, constant encouragement, and moral support during my work. I am heartfully thankful to Dr. Sourabh Solanki, and Vibhum Singh for sharing all the valued and casual moments which helped me during the hardship of my this work.

Above all, the most valued gratitude is expressed towards my mother (Late Asha Gupta), my father (Dr. Upendra Gupta), my uncle (Er. Vishwaranjan Gupta), my brother (Aditya Maheshwari), my sister (Pragya Maheshwari), my uncles, my aunts, and my cousins for their unbounded love, endless support, and faith in me, without which I would not have been able to achieve the most significant milestone of my

life.

At last, I want to thank everyone who was part of this journey and has, in one way or another, helped me to successfully complete this research work. I am signing off with a quote of Albert Einstein -

“A person who never made a mistake, never tried anything new”.

Shishir Maheshwari

Dedicated to

My Mother

Late Mrs. Asha Gupta

ABSTRACT

Glaucoma, after cataracts, is the second most leading cause of vision loss. It develops due to increased intraocular pressure (IOP) that damages retinal nerve fibres (RNFs). Generally, glaucoma does not exhibit any indication of its progression in early stages until it becomes more advanced. Therefore, early diagnosis and routine checkup are required to prevent further vision loss.

Ophthalmologists employ certain clinical instruments to diagnose glaucoma. In addition to these clinical examinations, advanced computerised imaging devices are used to detect the presence of glaucoma. These imaging devices generate retinal and optic nerve head (ONH) images along with objective quantitative measures. Experts use these images and measures for further investigation of glaucoma condition. However, the aforementioned clinical methods are manual and require skilled supervision. Moreover, the computerised imaging devices are bulkier, fragile, expensive, require trained professionals, and are generally not available in rural and remote areas. Further, the retinal images obtained using these imaging devices require manual evaluation by qualified experts. This manual evaluation is subjective and introduces inter and intra-observer variability, which occurs due to inconsistent perception of different experts towards the structural and functional damages, which characterises glaucoma, within the eye.

Unlike the advanced computerised imaging devices, fundus camera is a basic imaging device without computational setup. Therefore, it is generally portable and economical. Retinal fundus image acquired using fundus camera can be employed to visualise optic cup, optic disk, and blood vessels. In this way, these images help diagnose glaucoma condition. However, as the number of glaucoma cases is increasing every year, it is a time-consuming and challenging task to examine individual retinal images manually. These challenges can be overcome by developing retinal fundus image based computer-aided systems that are fast and accurate. These systems do not involve human intervention and can assist experts in their diagnosis, thereby reducing the burden of mass-screening.

In recent years, with the development of advanced image analysis techniques and machine learning algorithms, there exists a huge potential for development of efficient, accurate, and state-of-the-art methods for computer-aided automated

diagnosis of glaucoma. These methods can be used to develop prompt, reliable, handy, and cost-effective glaucoma diagnostic systems.

Therefore, this thesis aims to propose computer-aided approaches for automated glaucoma diagnosis based on advanced image analysis techniques and machine learning algorithms. In general, such approaches involve following processing stages. The initial stage involves image preprocessing techniques such as resizing, filtering, etc. In the next stage, meaningful features from the input fundus image are extracted using image analysis techniques. This is followed by ranking and selection of the extracted features. Finally, the features are fed to a classifier to discriminate between normal and glaucoma classes.

The first three approaches presented in the thesis involve the aforementioned processing stages. The first two approaches for glaucoma diagnosis are based on adaptive non-stationary image analysis techniques. Specifically, empirical wavelet transform (EWT), and iterative variational mode decomposition (VMD) have been explored. A local bit-level texture descriptor based approach has also been developed for glaucoma diagnosis. Additionally, this thesis explores convolution neural network (CNN) based approach for glaucoma diagnosis. This approach automatically extracts relevant features and classifies the input fundus image.

The experimental results presented in this thesis demonstrate that the proposed approaches are effective for glaucoma diagnosis. Moreover, the proposed approaches achieve state-of-the-art performance on benchmark datasets.

Contents

List of Figures	xviii
List of Tables	xxii
List of Abbreviations	xxv
1 Introduction	1
1.1 Glaucoma	2
1.1.1 Glaucoma progression	2
1.1.2 Types of glaucoma	4
1.2 Clinical diagnosis of glaucoma	4
1.2.1 Clinical tests	5
1.2.2 Computerised imaging devices	5
1.3 Challenges and motivation	6
1.3.1 Challenges	6
1.3.2 Motivation	7
1.4 Related work	9
1.4.1 Objectives	13
1.5 Thesis contributions and organisation	13
2 Empirical Wavelet Transform Based Approach for Glaucoma Diagnosis	19
2.1 Introduction	19
2.2 Proposed approach	20

2.2.1	Overview of the proposed approach	21
2.2.2	Data preprocessing	21
2.2.3	Empirical wavelet transform	21
2.2.4	Feature extraction	25
2.2.5	Feature selection and ranking	30
2.2.6	Feature normalisation	31
2.2.7	Classification	32
2.2.8	Performance parameters & cross-validation	33
2.3	Dataset and experimental results	35
2.3.1	Dataset	35
2.3.2	Results & discussion	35
2.4	Summary	41
3	Iterative Variational Mode Decomposition of Fundus Images for Glaucoma Diagnosis	45
3.1	Introduction	45
3.2	Proposed approach	46
3.2.1	Overview of the proposed approach	46
3.2.2	Preprocessing step	47
3.2.3	Variational mode decomposition	48
3.2.4	Feature extraction	50
3.2.5	Feature Normalisation	53
3.2.6	Feature selection	54
3.2.7	Classification	56
3.3	Dataset and experimental results	56
3.3.1	Dataset	56
3.3.2	Results & discussion	56
3.4	Summary	61
4	Local Bit-Level Texture Descriptor for Glaucoma Diagnosis	63
4.1	Introduction	63
4.2	Proposed approach	64
4.2.1	Overview of the proposed approach	64

4.2.2	Preprocessing of fundus images	64
4.2.3	Bit plane slicing	65
4.2.4	Local binary patterns based feature extraction	66
4.2.5	Feature normalization	70
4.2.6	Feature Selection	70
4.2.7	Classification	74
4.2.8	Decision level fusion	74
4.3	Dataset and experimental results	74
4.3.1	Database	74
4.3.2	Results & discussion	75
4.4	Summary	76
5	CNN-based Approach for Glaucoma Diagnosis	83
5.1	Introduction	83
5.2	Proposed approach	84
5.2.1	Overview of the proposed approach	84
5.2.2	Convolutional neural network	85
5.2.3	Transfer learning	87
5.2.4	Data augmentation	88
5.3	Dataset & experimental results	89
5.3.1	Dataset	89
5.3.2	Results & discussion	89
5.4	Summary	93
6	Conclusions and Future Scope	95
6.1	Conclusions	95
6.2	Future scope	97
	References	101
	List of Publications	110

List of Figures

1.1	Human eye anatomy.	1
1.2	Field of view: (a) normal eye, and (b) eye with partial glaucoma.	2
1.3	(a) Flow of AH in normal eye condition. (b) Accumulation of AH in glaucoma condition.	3
1.4	Types of glaucoma: (a) open-angle glaucoma, and (b) angle-closer glaucoma.	4
2.1	Block diagram of EWT based approach for glaucoma diagnosis.	22
2.2	Sample fundus images: (a) normal, and (b) glaucoma.	23
2.3	Fourier spectrum segmentation in EWT.	23
2.4	Sub-figures (a) and (b) are R channel of Figs. 2.2(a) and 2.2(b), respectively. Sub-figures (c), (e), (g), and (i) are EWT components of (a). Similarly, sub-figures (d), (f), (h), and (j) are EWT components of (b).	26
2.5	Sub-figures (a) and (b) are G channel of Figs. 2.2(a) and 2.2(b), respectively. Sub-figures (c), (e), (g), and (i) are EWT components of (a). Similarly, sub-figures (d), (f), (h), and (j) are EWT components of (b).	27
2.6	Sub-figures (a) and (b) are B channel of Figs. 2.2(a) and 2.2(b), respectively. Sub-figures (c), (e), (g), and (i) are EWT components of (a). Similarly, sub-figures (d), (f), (h), and (j) are EWT components of (b).	28

2.7	Sub-figures (a) and (b) are Gr channel of Figs. 2.2(a) and 2.2(b), respectively. Sub-figures (c), (e), (g), and (i) are EWT components of (a). Similarly, sub-figures (d), (f), (h), and (j) are EWT components of (b).	29
2.8	Plot of accuracy versus kernel parameters using three-fold cross validation strategy for private database.	37
2.9	Plot of accuracy versus kernel parameters using ten-fold cross validation strategy for private database.	39
2.10	(a) Sample image (left) and its Fourier transform (right). (b) Sample image (left) and its Fourier transform (right). (c) Retinal fundus image (left) and its Fourier transform (right)	40
3.1	Overview of the iterative VMD based approach.	47
3.2	Top row: normal fundus images. Bottom row: glaucoma fundus images.	48
3.3	Illustration of iterative 2D-VMD. (*iter = iteration, *comp = component)	50
3.4	Iterative VMD components of G channel of fundus image in Fig. 3.2(a).	51
3.5	Iterative VMD components of G channel of fundus image in Fig. 3.2(e).	52
3.6	Plot of accuracy versus number of features for (a.) three-fold, and (b.) ten-fold cross validation strategies.	58
3.7	Plot of accuracy versus kernel parameter for first-thirteen features with (a.) three-fold, and (b.) ten-fold cross validation strategies.	59
4.1	Block diagram of the local bit-level texture descriptor approach.	65
4.2	Sample fundus images: normal (top row) and glaucoma (bottom row) class.	66
4.3	Bit planes of R channel of Fig. 4.2(e).	67
4.4	LBP images of bit planes shown in Fig. 4.3.	69
4.5	Plot of classification performance versus number of features for 2^{nd} order polynomial kernel.	78
4.6	Plot of classification performance versus number of features for 3^{rd} order polynomial kernel.	79
5.1	Overview of the CNN-based proposed approach.	85

List of Figures

5.2	Modified Alexnet architecture via transfer learning.	87
5.3	The t-SNE plot of: features learned by <i>conv5</i> layer (left), output of <i>fc6</i> (middle) and <i>fc7</i> (right) layers of the modified CNN model. . . .	93

List of Tables

1.1	Existing methodologies for computer-aided glaucoma diagnosis. . . .	14
2.1	Ranked correntropy features of R channel of private database. . . .	31
2.2	Ranked correntropy features of G channel of private database. . . .	31
2.3	Ranked correntropy features of B channel of private database. . . .	32
2.4	Ranked correntropy features of Gr channel of private database. . . .	32
2.5	Classification performance of the proposed approach using three-fold cross-validation for private database.	36
2.6	Classification performance of the proposed approach using ten-fold cross-validation for private database.	36
2.7	Classification performance of the proposed approach using three-fold cross-validation for public database.	38
2.8	Classification performance of the proposed approach using ten-fold cross-validation for public database.	38
2.9	Comparison of proposed approach with existing methodologies for automated glaucoma detection.	42
3.1	Results of features ranked using ReliefF method.	55
3.2	Comparison table of existing techniques for automated glaucoma detection.	60
4.1	Features extracted with t values for R channel.	71
4.2	Features extracted with t values for G channel.	72
4.3	Features extracted with t values for B channel.	73

4.4	Classification performance for different channels, and order of polynomial kernel function.	75
4.5	A comparative summary of the existing methods for automated glaucoma diagnosis.	80
5.1	Architecture of modified Alexnet CNN model.	88
5.2	Classification performance for LBP-based data augmentation.	90
5.3	Classification performance without LBP based data augmentation for 80:20 training:testing data split.	90
5.4	A comparative summary of the existing methods for automated glaucoma diagnosis for public database.	91
5.5	Description of legends used in Fig. 5.3.	92

List of Abbreviations

AH aqueous humour.

ANFIS adaptive neuro-fuzzy inference system.

ANN artificial neural network.

BPS bit plane slicing.

CDR cup-to-disk ratio.

CLAHE contrast limited adaptive histogram equalization.

CNN convolutional neural network.

CSLO confocal scanning laser ophthalmoscopy.

DWT discrete wavelet transform.

ECG electrocardiogram.

EEG electroencephalogram.

EMD empirical mode decomposition.

EWT empirical wavelet transform.

FD frequency-domain.

FT Fourier transform.

List of Abbreviations

HOS higher order spectra.

HRT heidelberg retinal tomograph.

IMED image euclidian distance.

IOP intraocular pressure.

LBP Local binary pattern.

LBP local binary pattern.

LBPs local binary patterns.

LCP local configuration pattern.

LDA linear discriminant analysis.

LDF linear discriminant function.

LS-SVM least squares support vector machine.

mfVEP multi-focal visual evoked potential.

OC optic cup.

OCT optic coherence tomography.

OD optic disk.

ODP optic disk photography.

ONH optic nerve head.

ONHSP optic nerve head stereo photograph.

ONHSPs optic nerve head stereo photographs.

PCA principal component analysis.

POD proper orthogonal decomposition.

RBF radial basis function.

List of Abbreviations

RNF retinal nerve fibre.

RNFL retinal nerve fibre layer.

RNFLs retinal nerve fibre layers.

RNFs retinal nerve fibres.

SLP scanning laser polarimetry.

STFT short time Fourier transform.

SVM support vector machine.

t-SNE t-Distributed Stochastic Neighbor Embedding.

TD time-domain.

TFD time-frequency domain.

VMD variational mode decomposition.

WHO world health organization.

WT wavelet transform.

Chapter 1

Introduction

Eyes are vital part of the human visual system responsible for generating vision when the light reflected from the surrounding objects enters the eye. Fig. 1.1 illustrates human eye anatomy. Initially, the reflected light enters the eye through the pupil and is focused on the retina by the eye lens. The reflected light then activates photo-receptors present beneath the retinal layer. The activated photo-receptors generate electrical impulses which are transmitted to the brain via retinal nerve fibres (RNFs) for further processing. However, improper functioning of the internal part of the eye may interrupt or permanently damage the vision. The vision loss may occur due to defect developed in eye lens in cataracts, damage to RNFs in glaucoma, or retinal damage in diabetic retinopathy.

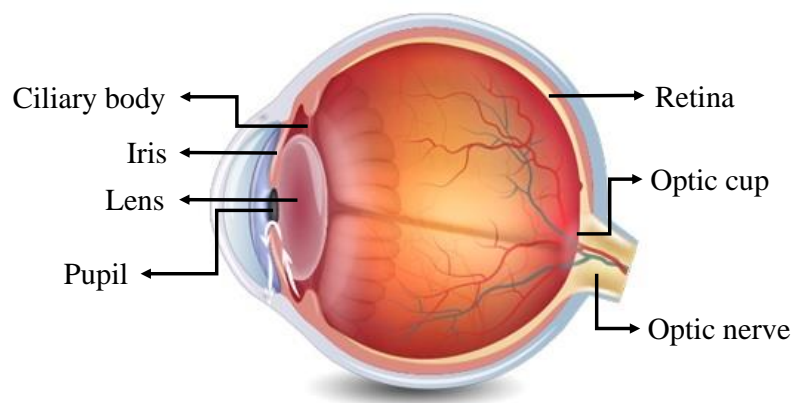


Figure 1.1: Human eye anatomy.
(Image source: <https://iristech.co/protect-yourself-from-glaucoma-with-iris>).

1.1 Glaucoma

Glaucoma is an ocular disorder which may lead to permanent vision loss, if not detected in its early stage. As per the world health organization (WHO), glaucoma is the second most leading cause of vision loss after cataract [1]. Glaucoma causes irreversible damage to the eye. The symptoms of glaucoma do not appear in the initial stage and can only be noticed when it progresses to advanced stage. As glaucoma develops slowly over time, it is referred to as *silent thief of sight* [2]. Due to glaucoma progression, the dark region gradually starts growing around the field of view of the eye and affects the vision. The artificially generated image in Fig. 1.2(b) illustrates how the field of view gets affected with partial glaucoma condition. Doctor advice regular eye checkups once every 2-4 years for people in the age group 40-64 years and once in 1-2 years for people older than 64 years [2]. Regular glaucoma screening followed by appropriate treatment may prevent further vision loss.



Figure 1.2: Field of view: (a) normal eye, and (b) eye with partial glaucoma.

(Image source:

<http://www.eyedocsottawa.com/services-special-vision/special-vision-concerns/glaucoma>).

1.1.1 Glaucoma progression

The vision loss in glaucoma occurs because of the damage caused to RNFs, which transmits visual information to the brain. The RNFs are damaged by increased intraocular pressure (IOP). Within the eye, IOP is regulated by the balance in the production of aqueous humour (AH) and its drainage through trabecular mesh

[3]. Fig. 1.3(a) illustrates the flow of AH in normal eye condition. IOP is largely influenced by the imbalance generated due to the malfunction of trabecular mesh, which partially or entirely blocks the flow of AH. Due to the blockage, the AH starts accumulating in the space between the cornea and the iris, as shown in Fig. 1.3(b). The imbalance increases the IOP, which in turn damages the RNFs [4]. The damaged RNFs become non-functional and do not transmit visual information. Moreover, the vision loss due to glaucoma cannot be reversed as no treatments are available to revitalise the damaged RNFs. The damage due to glaucoma is characterised by structural changes, which get reflected in the parameters such as optic disk (OD) diameter, OD area, optic cup (OC) diameter, rim area, and mean cup depth [5].

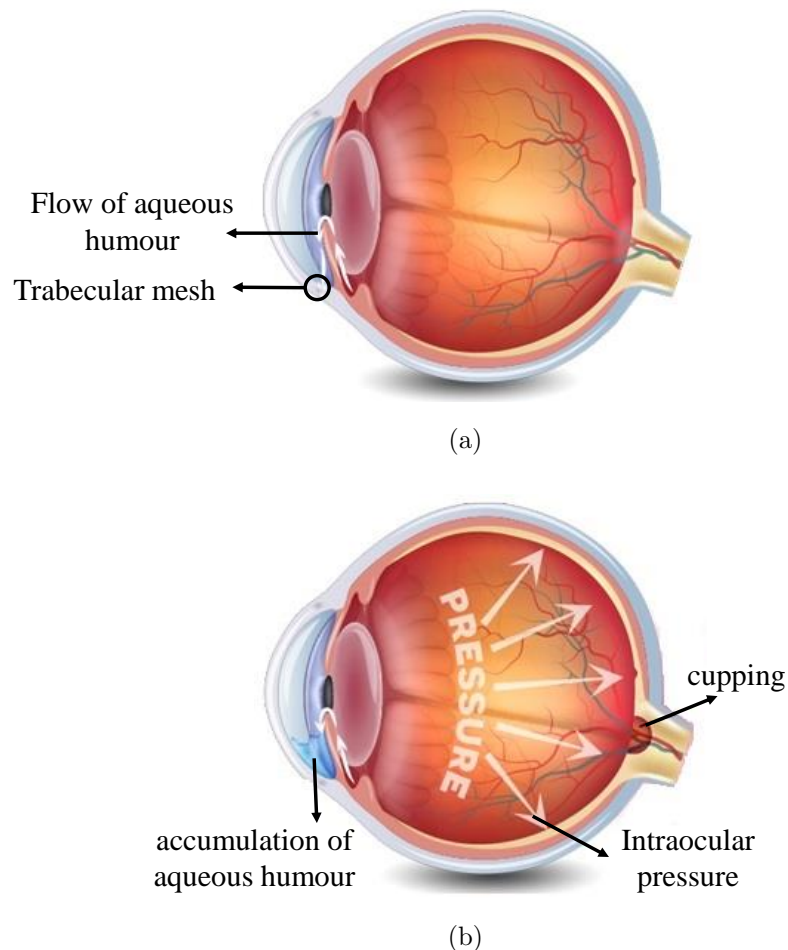


Figure 1.3: (a) Flow of AH in normal eye condition. (b) Accumulation of AH in glaucoma condition.

(Image source: <https://www.insightvisioncenter.com/treating-and-controlling-glaucoma>).

1.1.2 Types of glaucoma

There are two types of glaucoma, namely, open-angle glaucoma and angle-closure glaucoma, which are described below:

1. Open-angle glaucoma: It is the most common type of glaucoma, which has an open angle between iris and cornea, as shown in Fig. 1.4(a). It occurs due to slow congestion of the drainage canals, which gradually increases the IOP. Open-angle glaucoma develops slowly without any noticeable symptoms in the early stages.
2. Angle-closure glaucoma: This is a rare type of glaucoma, in which the angle between iris and cornea is closed, as shown in Fig 1.4(b). It occurs due to sudden blockage of the outflow of AH, which abruptly increases the IOP. The symptoms can be noticed in the form of red-eye and acute pain.

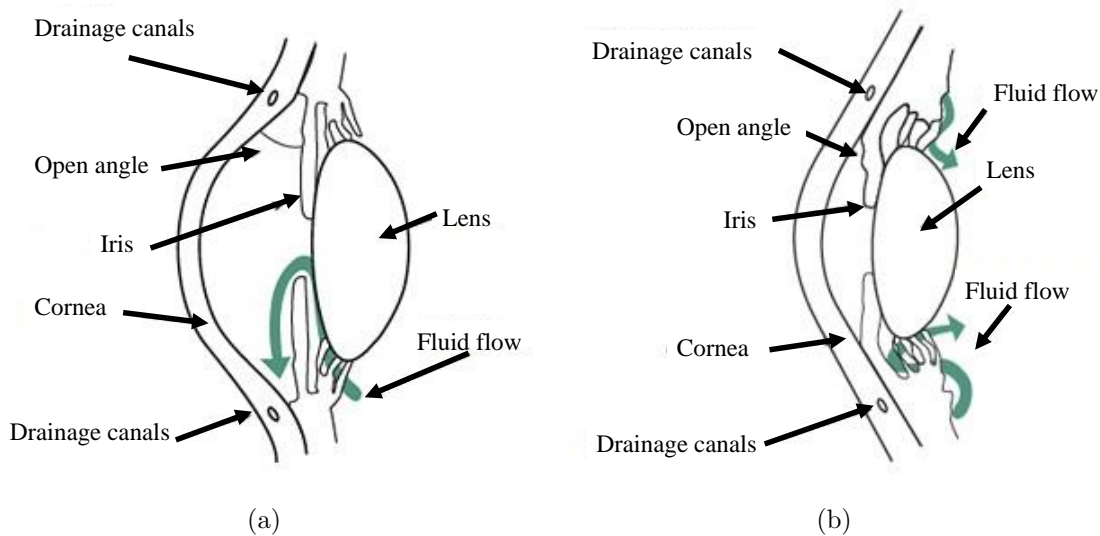


Figure 1.4: Types of glaucoma: (a) open-angle glaucoma, and (b) angle-closer glaucoma.

(Image source: <https://www.glaucoma.org/glaucoma/types-of-glaucoma.php>).

1.2 Clinical diagnosis of glaucoma

In the initial stage, the symptoms of glaucoma do not appear until it progresses to an advanced stage. This happens because the IOP develops slowly over time and

gradually damages the RNFs. The damage caused to RNFs will lead to vision loss. Therefore, to prevent further vision loss, experts advise routine check-up, followed by appropriate treatment. Ophthalmologists employ certain clinical instruments to diagnose glaucoma. In addition, they employ advanced computerised imaging devices to investigate the glaucoma condition. The clinical tests and computerised imaging devices are discussed in the following sub-section.

1.2.1 Clinical tests

The clinical tests involved in glaucoma diagnosis are as follows:

- **Tonometry:** In this test, IOP is measured with the help of tonometer. During the process, the eye is made numb using eye drops, and then tonometer is employed to measure IOP, which helps in identifying glaucoma condition in the eye. There is an increased risk of glaucoma when the pressure within the eye exceeds 22 mm Hg.
- **Ophthalmoscopy:** This test is used to examine the damage to RNFs. Eye drops are used to dilate the pupil, enabling the examiner to look into the eye to investigate the condition of RNFs.
- **Perimetry:** This is a visual field test of the eye. It involves the evaluation of the eye's visual field, which indicates the damage caused due to glaucoma progression.
- **Gonioscopy:** This test involves assessing the angle between the iris and the cornea. The open or wide-angle corresponds to a normal eye condition. On the other hand, narrow or close angle signifies the possibility of glaucoma.
- **Pachymetry:** In this test, a pachymeter measures the corneal thickness, which may influence the eye pressure readings.

1.2.2 Computerised imaging devices

In addition to these clinical tests, advanced computerised imaging devices are commonly employed to detect the glaucoma condition. These devices are expensive due

to the sophisticated optical and mechanical assemblies. The imaging setup needs to be accurately aligned and focused on the patient's eye to acquire glare-free images of retina and optic nerve head (ONH), along with a set of objective quantitative parameters. Experts rely on these measures and images to investigate glaucoma condition. Brief descriptions of different imaging devices are provided below:

- Scanning laser polarimetry (SLP): This device is used to measure the thickness of retinal nerve fibre layer (RNFL), which is related to the density of RNFs [6]. RNFL thickness leads to a decrease in the ganglion cell layer. RNFL damage may precede optic nerve damage in early glaucoma. The limitation of SLP is that it produces unreliable values for RNFL thickness in patients with other medical conditions.
- Confocal scanning laser ophthalmoscopy (CSLO): CSLO is an imaging tool that provides a 3D composite image of ONH and posterior segment [7]. CSLO generates stereometric parameters such as rim area, rim volume, cup shape measure, cup-disk (C/D) ratio, retinal height variation along the contour line and RNFL thickness. Limitations of CSLO include the requirement for the operator to manually outline the disk margin and the use of a reference plane in the calculation of many stereometric parameters.
- Optical coherence tomography (OCT): OCT performs cross-sectional imaging of nerve tissues. OCT can identify RNFL defects in areas corresponding to visual field defects.

1.3 Challenges and motivation

This section discusses major challenges involved in the diagnosis of glaucoma and presents the motivation behind the computer-aided approaches proposed in this thesis.

1.3.1 Challenges

In a worldwide survey, the number of people diagnosed with glaucoma was 60.5 million in 2010, and this number increased to 64.3 million in 2013. The estimated

global prevalence of glaucoma for the population aged between 40–80 years will reach to 76 million by 2020 and approximately 112 million by 2040 [8], [9]. This increase in the number of people with glaucoma affects the social economy and quality of life. Therefore, early diagnosis is necessary to prevent further vision loss due to glaucoma.

Many times, a single clinical diagnostic examination of the eye does not help in evaluating the characteristics of glaucoma. Therefore, experts rely on more than one clinical diagnostic tests to detect glaucoma. Multiple tests increase the initial cost of the diagnosis. Furthermore, clinicians perform a visual inspection of the retinal images produced by the advanced computerised imaging devices. These images aid the experts in evaluating the visual function and structural changes that characterises glaucoma.

The aforementioned clinical procedures are manual and require skilled supervision. Also, the computerised imaging devices are bulky, fragile, expensive, require trained professionals, and are usually not available in rural and remote areas [10]. Further, the retinal images generated using these computerised imaging devices require manual evaluation by qualified experts. The manual investigation tends to be subjective as it involves inter and intra-observer variability [4]. This variability occurs due to inconsistent perceptions of different experts towards the structural and functional damages that characterise glaucoma. Therefore, using these methods for mass-screening for glaucoma is likely to be infeasible in the future.

The aforementioned challenges discussed so far have motivated us to develop computer-aided methodologies for automated glaucoma diagnosis using advanced image analysis and machine learning algorithms.

1.3.2 Motivation

Unlike advanced computerised imaging devices, fundus camera is simple imaging device without computational setup. The fundus camera is generally portable and economical. The image acquired from a fundus camera can be employed to visualise optic cup, optic disk, and blood vessels. The fundus image-based computational methods for glaucoma diagnosis have proven to be prompt, cost-effective, and fairly accurate. In recent years, with the advancement in image analysis and machine

learning algorithms, there exists a huge potential for the development of effective and state-of-the-art computer-aided methods for automated glaucoma diagnosis using fundus images. These methods are expected to aid clinicians during mass screening.

Of late, various computer-aided methodologies have been proposed for automated glaucoma diagnosis. Some of the existing methodologies employ objective quantitative parameters generated from the computerised imaging devices such as SLP, CSLO, and OCT. Specifically, these imaging devices generate parameters such as RNFL thickness, RNFL cross-sectional area, optic disc and cup area, C/D ratio, cup depth, cup shape, etc., which are employed for glaucoma diagnosis. However, these parameters are obtained by marking the optic rim boundaries manually by the skilled operator in the retinal fundus image generated by the imaging device. Therefore, the obtained parameters are prone to operator error.

Moreover, the fundus images have also been employed for computer-aided methodologies for glaucoma diagnosis. Some of the existing methods are based on the segmentation of the fundus image. The segmentation based approaches employ morphological and thresholding operations to separate the desired region of interest in the fundus image. Further, this separated region is then processed to detect the presence of glaucoma. However, segmentation based approaches suffer from localisation and thresholding error. The small error in segmentation may lead to significant changes in measurements which result in the wrong diagnosis.

The texture feature based analysis of fundus image has also been investigated in some of the existing methods. In texture-based approaches, the image analysis methods convert the fundus image into simpler yet meaningful features. Recently, Fourier analysis, wavelet transform, higher order spectra (HOS), higher-order cumulant, Gabor transform, etc. are employed as texture-based image analysis methods. However, these image analysis methods have one or more pre-defined basis functions which are non-adaptive as they are designed independently of the processed signal. On the other hand, the aim of adaptive methods is to construct such a basis which is directly based on the information contained in the signal.

The aforementioned limitations of the existing methodologies have motivated us to explore adaptive techniques. Therefore, in this thesis, the adaptive non-stationary image analysis technique based approaches are proposed and experimentally investi-

gated for computer-aided automated diagnosis of glaucoma. The existing computer-aided methodologies for glaucoma diagnosis are discussed in the next section.

1.4 Related work

This section presents a brief discussion of the existing automated methodologies for computer-aided glaucoma diagnosis.

Of late, the objective quantitative parameters obtained from computerised imaging devices have been employed for to discriminate between glaucoma and non-glaucoma eyes. Nagarajan et al. [11] employed multi-focal visual evoked potential (mfVEP) data obtained from ObjectiVision perimetry device for glaucoma diagnosis. The mfVEP is a visual pathway data recorded from many regions of the visual field. The mfVEP is fed to a trained artificial neural network (ANN) for classification. Essock et al. [12] proposed wavelet-Fourier based approach, which is evaluated using RNFL thickness data obtained from GDx-VCC polarimetry. The 4th order wavelet transform is used in their approach to extract abnormalities and discontinuities. Further, Fourier transform (FT) is applied on the detail coefficients of the wavelet transform to obtain the Fourier amplitudes. The Fourier amplitudes and the approximation coefficients are combined to create a feature set, which is used for classification.

Huang et al. [13] developed an adaptive neuro-fuzzy inference system (ANFIS) to discriminate between glaucoma and non-glaucoma cases based on the quantitative assessment of OCT data reports of Taiwan Chinese population. The features extracted using orthogonal arrays of the RNFL thickness and ONH topography data obtained from OCT are fed to a classifier. The same group of authors, in their next work [14], developed an approach that improves the discrimination between glaucomatous and healthy eyes in Taiwan Chinese population. The evaluations have been performed on the RNFL thickness data generated from SLP. They employed entropy-based feature selection to remove irrelevant RNFL thickness parameters. The selected features are then fed to a classifier. The authors investigated linear discriminant analysis (LDA) and ANN for classification.

The optic disk topography parameters obtained using heidelberg retinal tomo-

graph (HRT) have been employed in [15] for glaucoma diagnosis. The authors explored neural network and linear discriminant function (LDF) for classification. They concluded that the neural network based approach provides better diagnostic accuracy for the glaucoma test. Greaney et al. [5] compared the discrimination capability of optic nerve head stereo photographs (ONHSPs), SLP, CLS, and OCT for glaucoma detection. Specifically, receiver operating characteristic (ROC) curves have been generated from the discriminant analysis of CSLO, OCT, SLP and ONHSP data. The authors observed that the analysis of ONHSP yields better performance than the quantitative methods such as CSLO, OCT, SLP for glaucoma diagnosis. They concluded that the combination of imaging methods would significantly improve glaucoma detection accuracy. Also, analysis involving quantitative methods is subjective due to the involvement of experts.

Merickel et al. [16] computed cup-to-disc ratio of the optic nerve head from the fundus image. The authors employed a soft pixel classification method to generate the probability map of the optic disc. Further, a cost function is developed to maximise the probability of the region within the disc. The image is then segmented by graph search algorithm capable of detecting the border by maximising the probability of disc. Nayak et al. [17] performed morphological operations on fundus images to detect glaucoma. The authors extracted features such as cup-to-disk ratio, the ratio of the distance between the optic disc centre and ONH to the diameter of the optic disc, and the ratio of blood vessel area in inferior-superior side to the area of blood vessels in the nasal-temporal side. The extracted features are then fed to the neural network for classification.

Swindale et al. [18] modelled the shape of ONH by a smooth 2D surface described by ten parameters. Parameters such as the degree of the surface curvature of the disc region surrounding the cup, the steepness of the cup walls, measures of cup width and cup depth have been extracted from fundus images. These parameters have been used to discriminate between normal and glaucoma images. Joshi et al. [19] performed OD and OC segmentation in fundus images for glaucoma diagnosis. They computed vertical cup-to-disk diameter ratio and cup-to-disk area ratio for glaucoma assessment.

Balasubramanian et al. [20] proposed a method for glaucoma diagnosis based on

the pixel-wise changes for glaucoma detection. The authors compared the reference and the follow-up ONH of each eye. Initially, to describe the structure of ONH of the eye, proper orthogonal decomposition (POD) is employed to create a baseline topograph for each eye. Further, the follow-up ONH topograph is compared with the baseline topograph that was constructed earlier. The changes in the pixel-wise ONH comparison was quantified by correlation, L1-norm and L2-norm, and image euclidian distance (IMED). This pixel-based method produces an error when the topographical position of ONH changes.

Kolar et al. [21] developed a fractal dimension based methodology for glaucoma diagnosis. In this method, the power spectrum of the fundus image is generated by the periodogram. Further, the fractal dimension is extracted as a feature from the power spectrum. The extracted features are fed to the support vector machine (SVM) classifier. The methodology proposed by Bock et al. [22] extracts raw pixel intensities, FT coefficients, and spline coefficients as features from fundus images. They formed a separate feature vector corresponding to each feature. Further, the principal component analysis (PCA) is applied to reduce the dimension of each feature vector. In this work, the authors employ a two-stage classification process. SVM is investigated as a classifier to evaluate the performance of the proposed method. In the first stage, each feature vector is fed to the separate SVM classifiers and obtains a probability score. The probability scores of separate SVMs are combined and fed to the second stage of the classification process.

Acharya et al. [23] explored texture features such as entropy, mean, energy, contrast, moments extracted from the fundus image. The HOS features, along with texture features, have been investigated for glaucoma diagnosis. The extracted features are ranked and fed to the classifiers. The authors observed that the classification performance of their methodology improves when ranked features are fed to the classifier. Dua et al. [24] proposed discrete wavelet transform (DWT) based method, which employs 2D DWT to decompose fundus images. The authors explored three well-known wavelet filters, namely, Daubechies (db3), symlets (sym3) and the biorthogonal (bio3.3, bio3.5, and bio3.7). The fundus images are decomposed into DWT components, and the mean and energy features are extracted from each of the decomposed components. The extracted features are ranked and fed to

a classifier for glaucoma diagnosis.

Mookiah et al. [25] developed HOS and DWT based methodology for glaucoma diagnosis. The fundus images have been preprocessed by histogram equalisation followed by radon transform. Further, the HOS and DWT are applied on the pre-processed fundus images. The entropy features from HOS components, and mean, and energy features from DWT components are extracted. The extracted features are fed to the SVM classifier. The authors investigated the classification performance for radial basis function (RBF) and polynomial kernel function. Noronha et al. [26] investigated higher-order cumulant features for glaucoma diagnosis using fundus images. The authors extracted third-order cumulant features from pre-processed fundus images. Further, LDA and Fisher's discrimination index are used for feature reduction and selection, respectively. The ranked features are fed to the SVM classifier. In the proposed work, authors investigated the classification performance of 2^{nd} and 3^{rd} order polynomial, and RBF as a kernel function.

Acharya et al. [27] developed Gabor transformation based methodology for glaucoma diagnosis using fundus images. Various textural features such as mean, variance, skewness, kurtosis, and entropies have been extracted from the Gabor transform coefficients. The extracted features are subjected to PCA to reduce the dimensionality of the feature vector. Authors employed various feature ranking methods, and the ranked features are fed to the SVM classifier. In this work, the authors evaluated SVM classifier performance by employing various classifier kernels. Authors in [1] proposed texton and local configuration pattern (LCP) based methodology. The textons are produced from fundus images by convolution of various filter banks. Further, the LCP features are extracted from the textons. The extracted features are ranked and fed to classifiers for glaucoma and non-glaucoma classification.

The methodologies proposed for glaucoma diagnosis generally involves features extraction and classification. The selection of relevant features and classifiers is a tedious job. The design of such hand-crafted features is time-consuming, strongly related to experts knowledge and have restricted representation power. On the other hand, convolutional neural network (CNN) integrates automatic feature extraction and the classification process. CNN is the advanced neural network developed of image analysis and classification task. It is employed in various application such as face

recognition [28], brain abnormality in MR images [29], liver cancer detection [30], myocardial infarction [31], mammogram image segmentation [32]. Recently, CNN is employed for glaucoma diagnosis and found effective as they provided promising classification performances. Authors in [33] and [4] proposed 6-layer and 18-layer CNN architecture for glaucoma diagnosis, respectively.

Transfer learning technique based approaches are also employed for glaucoma diagnosis. This technique uses a pre-trained CNN model to re-train on a new dataset for a similar classification task. GoogLeNet model is employed in [34] via transfer learning technique for glaucoma diagnosis. Authors in [35] used a combination of CNN and SVM. The features are extracted from CNN and fed to the SVM classifier.

Table 1.1 presents a summary of various methodologies developed for glaucoma diagnosis.

1.4.1 Objectives

The prime objective of this thesis is to propose state-of-the-art approaches for glaucoma diagnosis. Specifically, we propose approaches based on advanced image analysis techniques in combination with machine learning algorithms to explore texture features for glaucoma diagnosis using fundus images. The specific objectives of this thesis are as follows:

1. To propose and investigate the effectiveness of adaptive non-stationary image analysis based approaches for glaucoma diagnosis.
2. To develop a local bit-level texture descriptor method for diagnosis of glaucoma and investigate its effectiveness.
3. To employ advanced machine learning algorithm for glaucoma diagnosis that integrates both the automatic feature extraction and classification process.
4. To evaluate the performances of the proposed approaches on larger datasets.

1.5 Thesis contributions and organisation

The current chapter provides background about glaucoma, outlines the thesis motivation, briefly introduces previous methodologies developed for glaucoma diagnosis,

Table 1.1: Existing methodologies for computer-aided glaucoma diagnosis.

Authors	Techniques employed
Nagarajan et al. [11]	multi-focal visual evoked potential & artificial neural network
Essock et al. [12]	Discrete wavelet transform & Fourier transform
Huang et al. [13]	Adaptive neuro-fuzzy inference system
Huang et al. [14]	Linear discriminant analysis & artificial neural network
Bowd et al. [15]	Neural network & linear discriminant function
Greaney et al. [5]	Discriminant analysis
Merickel et al. [16]	pixel classification & graph search
Nayak et al. [17]	Morphological operations & neural network
Swindale et al. [18]	Optic nerve head modeling
Joshi et al. [19]	Active contour model
Balasubramanian et al. [20]	Proper orthogonal decomposition
Kolar et al. [21]	Power spectral & fractal dimension
Bock et al. [22]	Raw pixel intensities, Fourier transform & spline coefficients
Acharya et al.[23]	Higher-order spectra & texture features
Dua et al. [24]	Discrete wavelet transform based energy features
Mookiah et al. [25]	Higher-order spectra & discrete wavelet transform
Noronha et al. [26]	Higher-order cumulant
Acharya et al.[27]	Gabor transformation
Acharya et al.[1]	Texton & local configuration pattern
Cheng et al. [33]	6-layer convolutional neural network
Raghavendra et al. [4]	18-layer convolutional neural network
Cerentini et al. [34]	GoogLeNet CNN model
Bander et al. [35]	Convolutional neural network & support vector machine

and discusses the thesis objectives. The subsequent chapters of the thesis and their contributions are organised as follows:

- In **Chapter 2**, we present an adaptive non-stationary image decomposition based approach for glaucoma diagnosis. Previously, the glaucoma diagnosis methodologies employ image analysis methods such as DWT, FT, and HOS. These image analysis techniques are non-adaptive methods which process the images irrespective of the information contained in them. On the other hand, adaptive image analysis techniques depend upon the information contained in an image. Therefore, in this chapter, the effectiveness of an adaptive non-stationary image decomposition based approach is investigated for glaucoma diagnosis using fundus images. Specifically, empirical wavelet transform (EWT) based approach is proposed.
- In **Chapter 3**, we propose an adaptive image analysis approach applied iteratively on fundus image for glaucoma diagnosis. Intermittently, the image analysis techniques may fail in extracting all the relevant details from fundus images at once. To extract the fine details in the form of closely related pixel intensity variations which corresponds to glaucoma, we analyse the performance of an iterative approach. Therefore, this chapter analyses the variational mode decomposition (VMD) based approach applied to the fundus images iteratively.
- In **Chapter 4**, we develop and analyse the effectiveness of local bit-level texture descriptor based approach for glaucoma diagnosis. Texture based approaches play an important role in classification [36], [37]. The local binary pattern (LBP) is a gray level texture descriptor which is found to be effective in applications such as face recognition [38], palmprint recognition [39]. In this chapter, unlike grey-level texture, the local bit-level texture descriptor is developed. The proposed approach employs bit plane slicing (BPS) followed by LBP.
- Computer-aided approaches typically involve the process of the hand-crafted feature extraction and classification. In **Chapter 5**, the proposed approach integrates the automatic feature extraction and the classification process. Specif-

ically, the effectiveness of CNN based is explored for glaucoma diagnosis. This approach employs transfer learning and LBP based data augmentation.

- Finally, **Chapter 6** provide the conclusions of the work proposed in this thesis and the directions for future research.

Empirical Wavelet Transform Based Approach for Glaucoma Diagnosis

This chapter presents the empirical wavelet transform (EWT) based approach for glaucoma diagnosis. In the proposed approach, the EWT is explored as an adaptive technique for the analysis of non-stationary signal. Specifically, EWT decomposes the fundus image into EWT components of various spatial frequency. Further, the correntropy based features are extracted from the EWT components and are fed to the classifier for discriminating between normal and glaucoma classes.

2.1 Introduction

Signal analysis plays an important role in studying the behaviour and properties of the signal by converting them into simpler yet meaningful entities. Stationary signals can be analysed by representing them in time-domain or frequency-domain. In time-domain representation, the signal is recorded with respect to time. For example, the electrical activity of the brain and the heart is recorded for every time instant in electroencephalogram (EEG) and electrocardiogram (ECG), respectively. Fourier transform (FT) is used to represent the time-domain signal into frequency-domain and effectively captures the frequencies present in the signal. But, it does not provide any information about the location of frequencies in time. On the other

hand, the analysis of non-stationary signal requires time and frequency information simultaneously. Therefore, FT is not suitable for the analysis of non-stationary signals [40].

The time-frequency domain (TFD) is a signal representation technique where the non-stationary signal can be simultaneously analysed in time and frequency. The short time Fourier transform (STFT) is one of the TFD methods for representing a non-stationary signal [40]. It is a windowed version of FT. However, due to the fixed window size, it can either have a good frequency or time localisation [40]. This limitation is overcome by wavelet transform, which is another TFD technique extensively used for analysing the non-stationary signal at different scales with the help of translation and dilation process. In the wavelet transform, the signal is represented as a weighted sum of wavelets. However, the selection of mother wavelets is a challenging task [41]. Moreover, these non-stationary signal analysis techniques have pre-defined basis functions which are designed irrespective of the signal to be processed.

The empirical mode decomposition (EMD), on the other hand, is an adaptive non-stationary signal analysis technique [42]. Unlike Fourier and wavelet transform, it does not rely on pre-defined basis functions and constructs a basis which is directly based on the information contained in the signal [43]. However, EMD suffers from mode mixing, lack of mathematical formulation, and the stopping criteria [41]. The EWT is also an adaptive non-stationary signal analysis technique. Therefore, in this chapter, the EWT based approach is proposed for glaucoma diagnosis.

The rest of the chapter is organised as follows: Section 2.2 presents the proposed approach. This section introduces EWT, the feature extraction, and the classification process. The fundus image dataset employed in the proposed approach is described in Section 2.3, which also presents the discussion on the experimental results. Finally, the chapter is summarised in Section 2.4.

2.2 Proposed approach

In this section, the steps involved in the proposed approach are explained briefly. Firstly, this section provides an overview of the proposed approach. Then, pre-

processing of data is followed by the description of EWT technique. Further, the feature extraction and selection technique are presented. The classification process is discussed at last.

2.2.1 Overview of the proposed approach

In this chapter, the EWT based approach is proposed for glaucoma diagnosis. EWT is an adaptive technique for the analysis of non-stationary signal. The 2D version of EWT developed for images [44] has been employed in this approach. The EWT is applied to each of the fundus image channels to obtain EWT components. Further, the correntropy [45] is extracted as a feature from the EWT components. The extracted features are normalised and ranked using Student's t test. Finally, the ranked features are fed to the least squares support vector machine (LS-SVM) classifier. Various classifier kernels such as RBF, Morlet and Mexican-hat wavelet have been investigated for the performance evaluation of the proposed approach. Three-fold and ten-fold cross-validation strategies have been used to validate the classifier performance. The block diagram of the proposed approach is shown in Fig. 2.1.

2.2.2 Data preprocessing

The sample colour fundus image for normal and glaucoma class is shown in Fig. 2.2. In the first step of the proposed approach, the red (R), green (G), and blue (B) channels are separated from colour fundus image. In addition, the grey-scale image is also obtained from the fundus image. The grey-scale image is referred to as grey (Gr) channel in the rest of the chapter. Further, the EWT is applied to R, G, B, and Gr channels. The EWT is discussed in the next section.

2.2.3 Empirical wavelet transform

EWT [43] is an adaptive technique for the analysis of non-stationary signals. It decomposes the signal into time-frequency components. Unlike FT and WT, EWT is signal-dependent method and do not have predefined basis functions.

In EWT, the Fourier spectrum of the signal, in the range 0 to π , is segmented into M number of parts as shown in Fig. 2.3. Each segment limit is denoted by

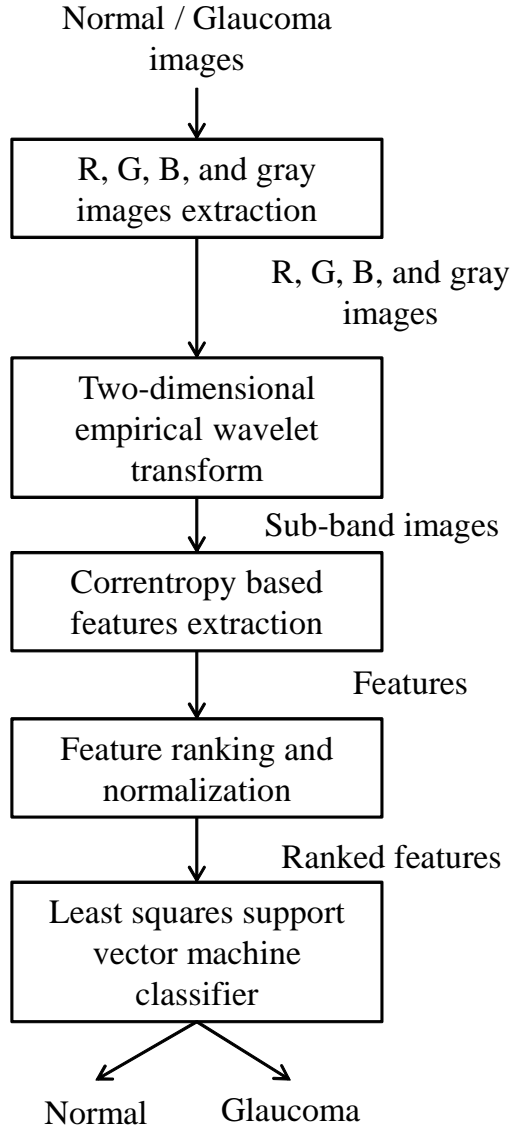


Figure 2.1: Block diagram of EWT based approach for glaucoma diagnosis.

ω_m , where $\omega_0 = 0$ and $\omega_M = \pi$. Each segment is denoted by $S_m = [\omega_{m-1}, \omega_m]$. The transition phase T_m is centered around ω_m , and has a width of $2\varrho_m$, where ϱ_m is expressed in terms of ω_m as $\varrho_m = \lambda\omega_m$ with $0 < \lambda < 1$.

After segmenting the Fourier spectrum, bandpass filters are designed on each segment S_m . These bandpass filters are called empirical wavelets. The empirical scaling function $\xi_m(W)$ and the empirical wavelets $\varsigma_m(W)$ can be mathematically expressed as [43]:

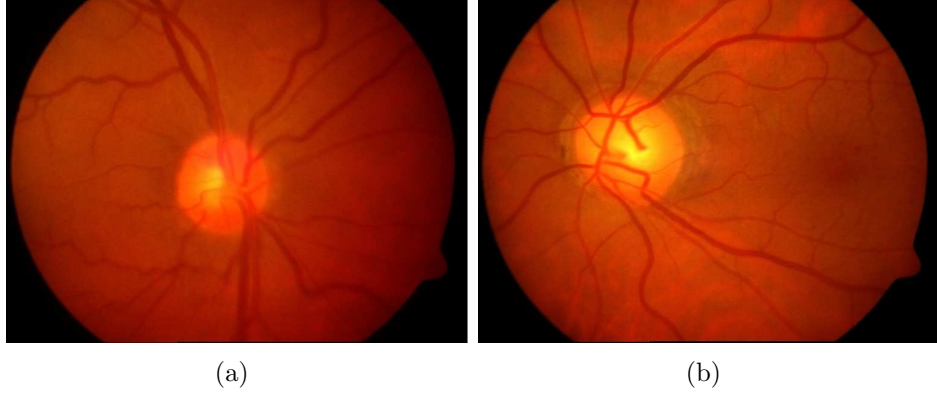


Figure 2.2: Sample fundus images: (a) normal, and (b) glaucoma.

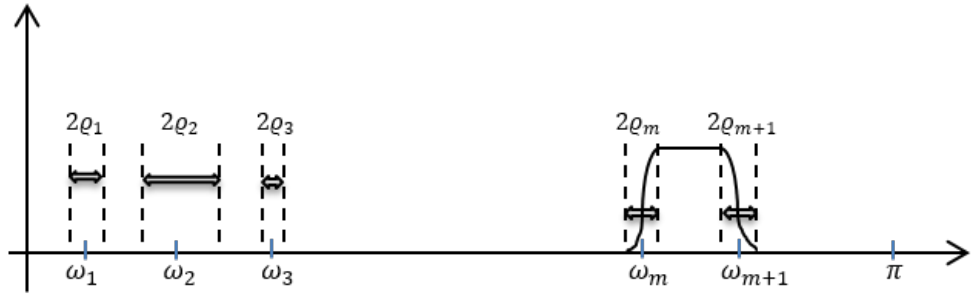


Figure 2.3: Fourier spectrum segmentation in EWT.

$$\xi_m(W) = \begin{cases} 1, & \text{if } |W| \leq (1 - \lambda)\omega_m \\ \cos \left[\frac{\pi}{2} F(\lambda, \omega_m) \right], & \text{if } (1 - \lambda)\omega_m \leq |W| \leq (1 + \lambda)\omega_m \\ 0, & \text{otherwise} \end{cases} \quad (2.1)$$

and

$$\varsigma_m(W) = \begin{cases} 1, & \text{if } (1 + \lambda)\omega_m \leq |W| \leq (1 - \lambda)\omega_{m+1} \\ \cos \left[\frac{\pi}{2} F(\lambda, \omega_{m+1}) \right], & \text{if } (1 - \lambda)\omega_{m+1} \leq |W| \leq (1 + \lambda)\omega_{m+1} \\ \sin \left[\frac{\pi}{2} F(\lambda, \omega_m) \right], & \text{if } (1 - \lambda)\omega_m \leq |W| \leq (1 + \lambda)\omega_m \\ 0, & \text{otherwise} \end{cases} \quad (2.2)$$

where $F(\lambda, \omega_m)$ and $F(\lambda, \omega_{m+1})$ can be expressed as [43]:

$$F(\lambda, \omega_m) = F\left(\frac{1}{2\lambda\omega_m} (|W| - (1 - \lambda)\omega_m)\right) \quad (2.3)$$

$$F(\lambda, \omega_{m+1}) = F\left(\frac{1}{2\lambda\omega_{m+1}} (|W| - (1 - \lambda)\omega_{m+1})\right) \quad (2.4)$$

The $F(z)$ satisfies the following criteria [43],

$$F(z) = \begin{cases} 0, & \text{if } z \leq 0 \\ 1, & \text{if } z \geq 1 \\ F(z) + F(1 - z) = 1 & \forall z \in [0, 1] \end{cases} \quad (2.5)$$

The scaling function and the empirical wavelet is then used to obtain EWT, denoted by $W_f(m, t)$. The EWT approximation coefficients are obtained by the inner product with the scaling function as follows:

$$W_f(0, t) = \langle f, \xi_m \rangle \quad (2.6)$$

Similarly, the EWT detailed coefficients are obtained by the inner product with the empirical wavelet as follows:

$$W_f(m, t) = \langle f, \varsigma_m \rangle \quad (2.7)$$

where f is FT of the signal.

In the proposed approach, the 2D version of EWT is employed on the fundus images. Let x be a 2D signal, then 2D EWT approach is expressed as follows [44]:

1. Compute 1D Fourier transform for each row of r of x and compute mean row

spectrum as:

$$X_R = \frac{1}{N_{Rw}} \sum_{r=0}^{N_{Rw}} X(r, \Omega) \quad (2.8)$$

2. Similarly, compute 1D Fourier transform for each column of c of x and compute mean column spectrum as:

$$X_C = \frac{1}{N_{Cl}} \sum_{c=0}^{N_{Cl}} X(\Omega, c) \quad (2.9)$$

where number of rows and columns are denoted by N_{Rw} and N_{Cl} in Eq. 2.8 and Eq. 2.8, respectively.

3. Perform boundaries detection on X_R and X_C and build the corresponding filter bank $\{\xi_1^R, \{\zeta_m^R\}_{m=1}^{N_R}\}$ and $\{\xi_1^C, \{\zeta_m^C\}_{m=1}^{N_C}\}$ respectively where N_R and N_C are the number of mean row and column sub-band respectively.
4. Filter x along the rows $\{\xi_1^R, \{\zeta_m^R\}_{m=1}^{N_R}\}$ which provides (N_R+1) output images.
5. Filter (N_R+1) output images along the columns with $\{\xi_1^C, \{\zeta_m^C\}_{m=1}^{N_C}\}$, this provides $(N_R+1)(N_C+1)$ sub-band images.

The 2D version of EWT has been applied on fundus images. The 2D EWT components are obtained using 2D empirical Littlewood-Paley wavelets [44]. Figs. 2.4-2.7 show the decomposed EWT components of R, G, B, and Gr channels, respectively. The pseudo-colour representation in Figs. 2.4-2.7 is used to create the visual difference between the EWT components.

2.2.4 Feature extraction

Feature extraction plays a vital role in the development of computer-aided diagnosis methods. It is the process of transformation of original data to an attribute with a reduced number of variables, which contains the most discriminatory information. In the proposed approach, the effectiveness of the correntropy is investigated as a feature extracted from the decomposed EWT components.

Correntropy: Correntropy is a non-linear kernel based measure of similarity which preserves both statistical and temporal information [45, 46, 47]. It measures correlation in the nonlinear domain of multiple delayed samples of the signal.

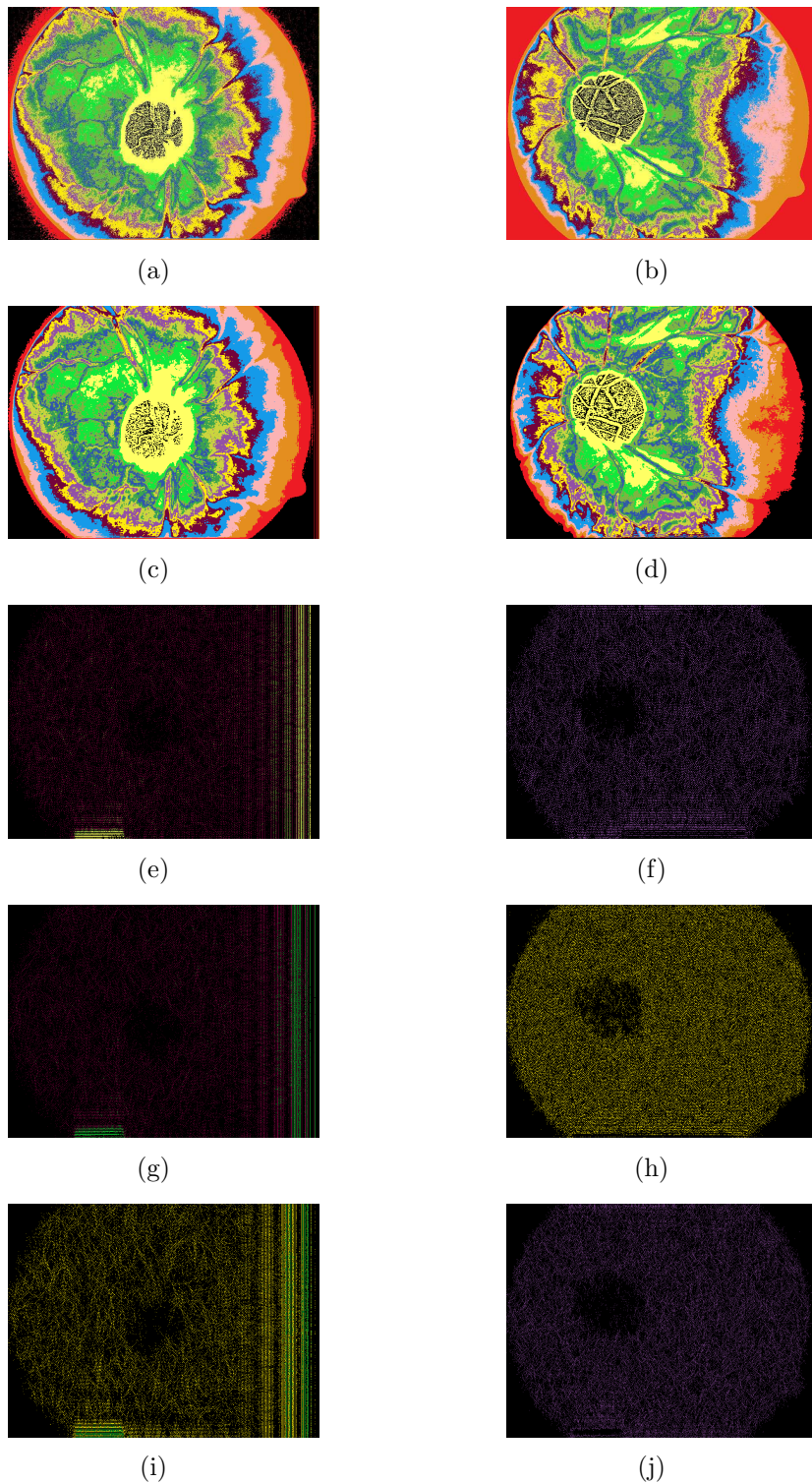


Figure 2.4: Sub-figures (a) and (b) are R channel of Figs. 2.2(a) and 2.2(b), respectively. Sub-figures (c), (e), (g), and (i) are EWT components of (a). Similarly, sub-figures (d), (f), (h), and (j) are EWT components of (b).

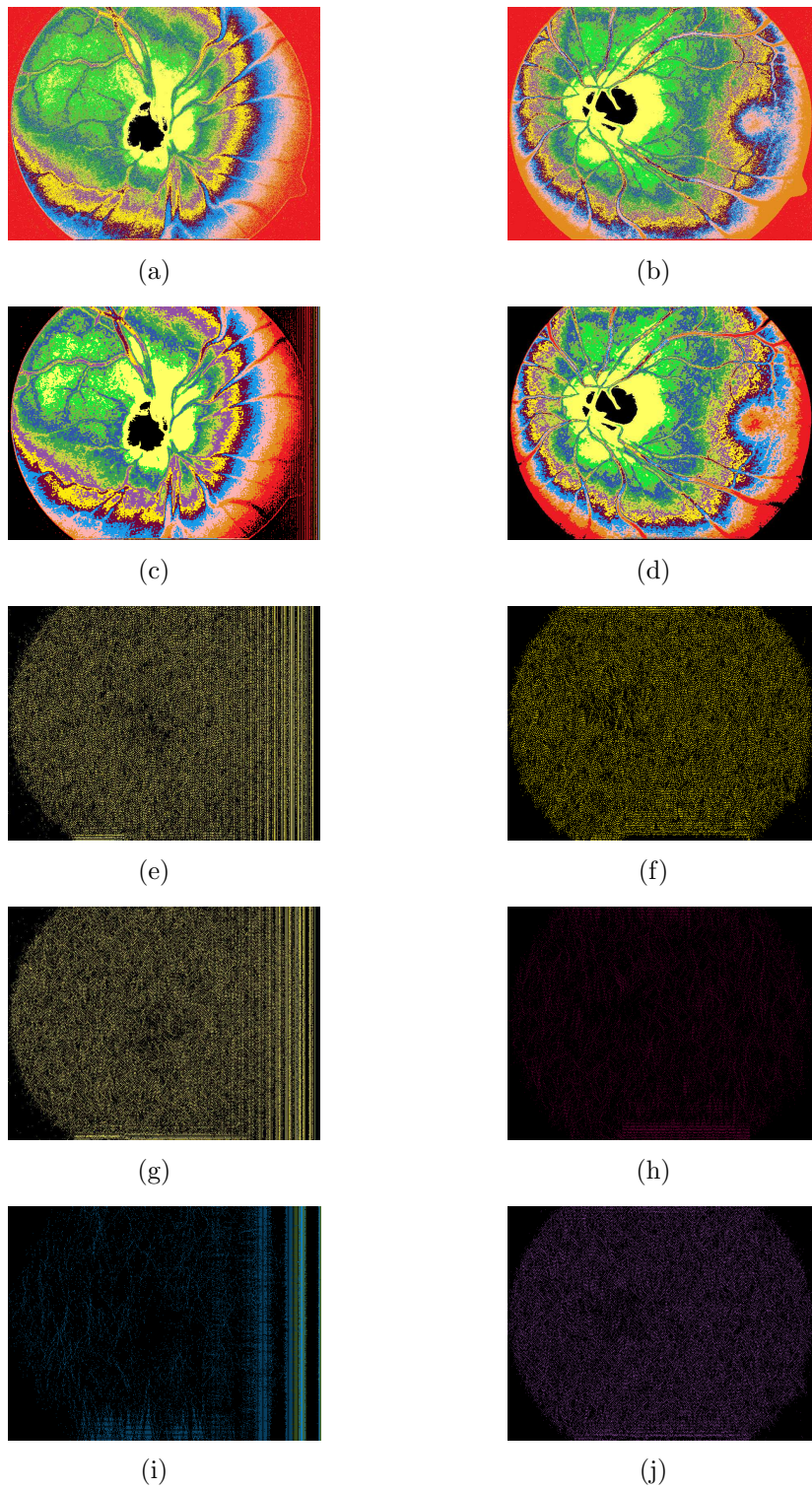


Figure 2.5: Sub-figures (a) and (b) are G channel of Figs. 2.2(a) and 2.2(b), respectively. Sub-figures (c), (e), (g), and (i) are EWT components of (a). Similarly, sub-figures (d), (f), (h), and (j) are EWT components of (b).

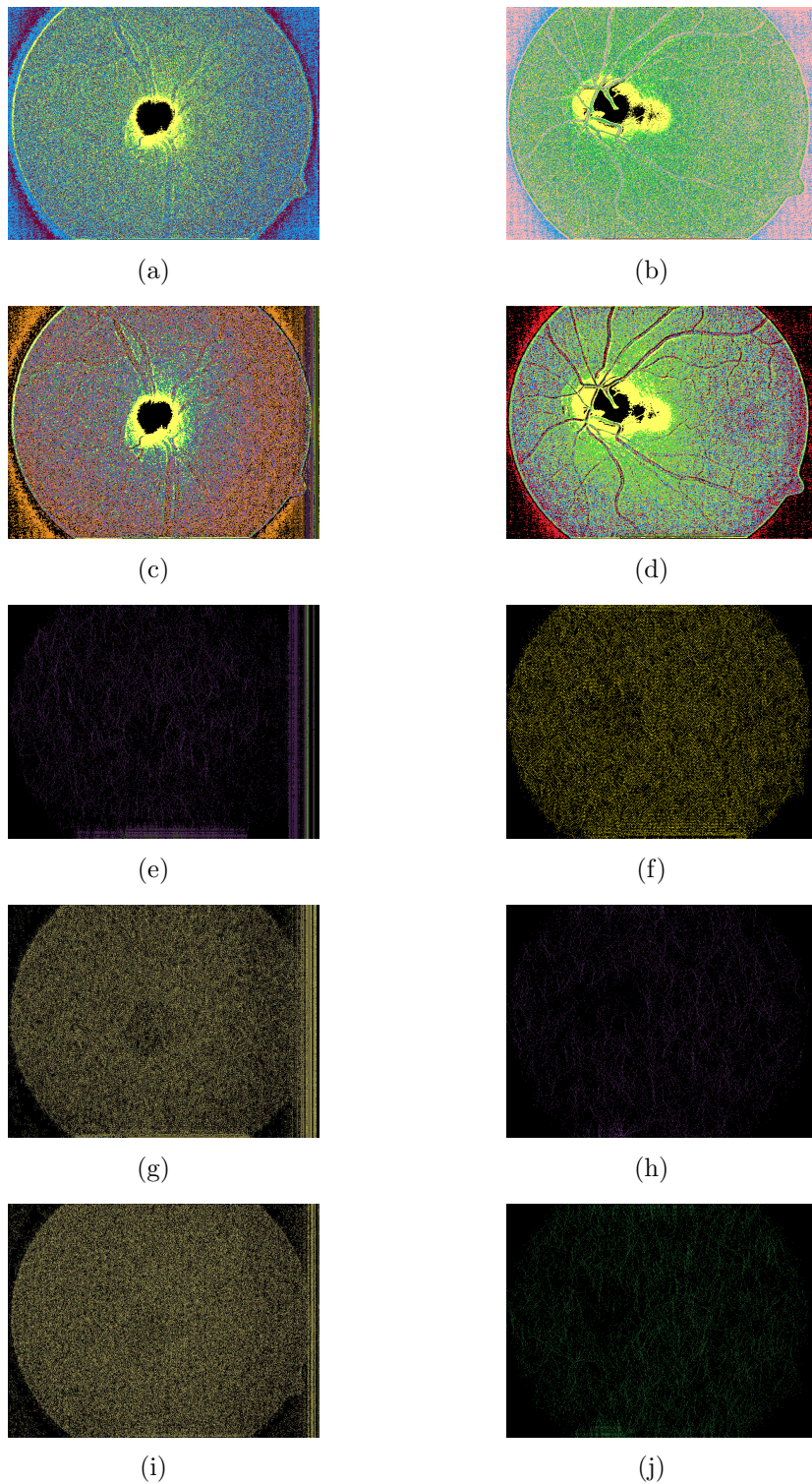


Figure 2.6: Sub-figures (a) and (b) are B channel of Figs. 2.2(a) and 2.2(b), respectively. Sub-figures (c), (e), (g), and (i) are EWT components of (a). Similarly, sub-figures (d), (f), (h), and (j) are EWT components of (b).

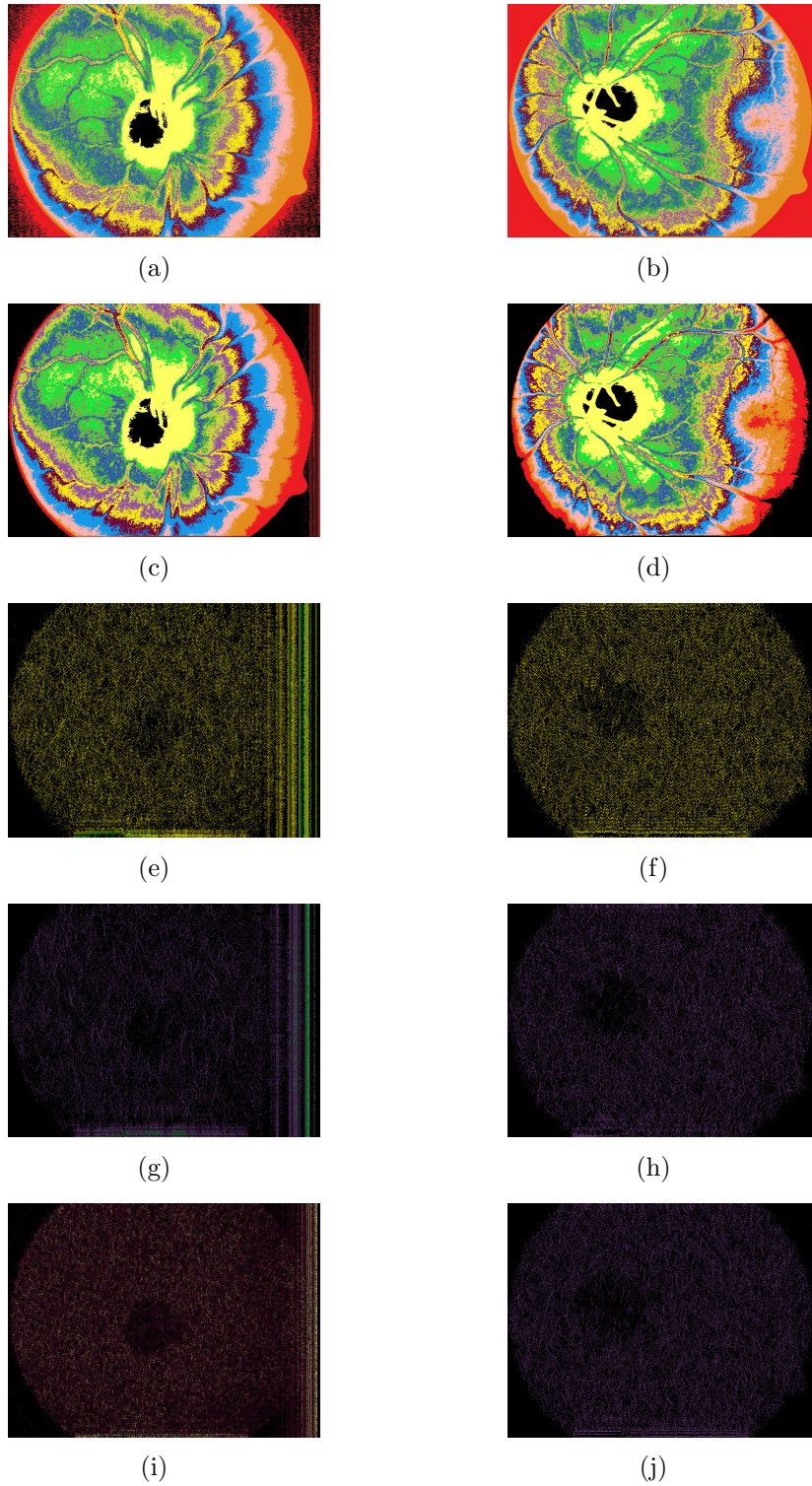


Figure 2.7: Sub-figures (a) and (b) are Gr channel of Figs. 2.2(a) and 2.2(b), respectively. Sub-figures (c), (e), (g), and (i) are EWT components of (a). Similarly, sub-figures (d), (f), (h), and (j) are EWT components of (b).

Recently, it has been employed for the diagnosis of coronary artery disease [48]. In this study, the correntropy is employed as a feature which incorporates the subtle pixel intensity variations from the decomposed EWT components. The correntropy, denoted as $CE(G)$ for lag G , can be expressed as [45, 47, 48]:

$$CE(G) = \left(\frac{1}{X-G+1}\right)^2 \sum_{x_1, x_2=G}^X \mathfrak{T}(t[x_1, x_2] - t[x_1 - G, x_2 - G]) \quad (2.10)$$

where $t[x_1, x_2]$ is the 2D signal, X is number of rows and columns. The Gaussian kernel function $\mathfrak{T}(t[x_1, x_2] - t[x_1 - G, x_2 - G])$, in Equation 2.10, can be expressed as:

$$\mathfrak{T}(t[x_1, x_2] - t[x_1 - G, x_2 - G]) = \frac{1}{\sqrt{2\pi\varepsilon}} \exp\left[-\frac{(t[x_1, x_2] - t[x_1 - G, x_2 - G])^2}{2\varepsilon^2}\right] \quad (2.11)$$

where the Gaussian kernel width is controlled by ε . The number of correntropy features depends on the value of G . In this study, 3 correntropy features are extracted from each decomposed EWT component.

2.2.5 Feature selection and ranking

All the extracted features do not contribute equally in the performance evaluation of the approach. Some of the extracted features possess higher discriminating potential than rest of the features. Inclusion of features with low discriminating capability will affect the performance of the computer-aided methods. Therefore, the proposed approach employs a feature selection technique to select the features with significant discriminating capability. In the proposed approach, Student's t -test algorithm [49, 27, 50] is explored for feature selection and ranking. The t -test discriminates two classes based on population *mean*. Features with high t value are more discriminatory and are ranked in the order of decreasing t value.

2.2.6 Feature normalisation

Skewed data may result in a false alarm and hampers the performance of the system. Feature normalisation brings the data into the desired range and reduces the effect of outliers. In this approach, z -score normalisation [51] is employed to normalise the data. The data is normalised as follows [23]:

$$\hat{d} = \frac{d - \bar{d}}{\tilde{d}} \quad (2.12)$$

where \hat{d} , \bar{d} and \tilde{d} are normalised data, mean and standard deviation of data d , respectively.

Tables 2.1-2.4 list the ranked features with their corresponding t values for R, G, B, and Gr channels, respectively. Where CE_{xy} , in *features* column, denotes y^{th} correntropy feature of x^{th} decomposed EWT component. These ranked features are then fed to the classifier, which is discussed in the next section.

Table 2.1: Ranked correntropy features of R channel of private database.

Features	Normal	Glaucoma	t value
CE_{13}	-0.514 ± 1.153	0.514 ± 0.399	4.611
CE_{12}	-0.412 ± 1.232	0.411 ± 0.408	3.475
CE_{42}	0.318 ± 1.006	-0.318 ± 0.901	2.578
CE_{32}	0.180 ± 1.047	-0.180 ± 0.933	1.407
CE_{43}	-0.079 ± 1.380	0.079 ± 0.342	0.610
CE_{33}	-0.051 ± 1.358	0.051 ± 0.429	0.390

Table 2.2: Ranked correntropy features of G channel of private database.

Features	Normal	Glaucoma	t value
CE_{13}	-0.425 ± 1.255	0.425 ± 0.292	3.611
CE_{12}	-0.365 ± 1.269	0.365 ± 0.386	3.013
CE_{43}	-0.179 ± 1.387	0.179 ± 0.197	1.405
CE_{33}	-0.153 ± 1.398	0.153 ± 0.173	1.187
CE_{42}	0.134 ± 1.238	-0.134 ± 0.682	1.039
CE_{32}	-0.035 ± 1.345	0.035 ± 0.472	0.270

Table 2.3: Ranked correntropy features of B channel of private database.

Features	Normal	Glaucoma	t value
CE ₄₂	0.389 ± 0.980	-0.389 ± 0.872	3.251
CE ₁₃	-0.341 ± 1.322	0.341 ± 0.214	2.790
CE ₂₂	0.339 ± 0.933	-0.339 ± 0.962	2.779
CE ₂₃	0.338 ± 1.055	-0.338 ± 0.827	2.765
CE ₁₂	-0.278 ± 1.331	0.278 ± 0.320	2.225
CE ₃₂	0.168 ± 1.139	-0.168 ± 0.823	1.313

Table 2.4: Ranked correntropy features of Gr channel of private database.

Features	Normal	Glaucoma	t value
CE ₁₃	-0.464 ± 1.234	0.464 ± 0.255	4.039
CE ₁₂	-0.407 ± 1.261	0.407 ± 0.316	3.431
CE ₄₂	0.279 ± 1.073	-0.279 ± 0.849	2.230
CE ₂₃	0.212 ± 1.066	-0.212 ± 0.896	1.669
CE ₃₃	-0.196 ± 1.378	0.196 ± 0.237	1.536
CE ₂₂	0.142 ± 1.104	-0.142 ± 0.879	1.102

2.2.7 Classification

Classifiers have always been employed in the development of computer-aided diagnosis approaches such as diabetes diagnosis using heart rate signals [50], septal defects detection using heart sound signals [52], CAD diagnosis using heart rate signals [48], seizure detection EEG [53, 54, 55, 56, 57] and glaucoma diagnosis using fundus images [23, 24, 25, 26]. In the proposed approach, LS-SVM [58, 59] is employed as a classifier. It is a supervised machine learning algorithm used to discriminate two or more classes using linear or non-linear kernel. The non-linear kernel function transform the linearly inseparable data into linearly separable by projecting it into higher-dimensional space.

Let there be N data points $\{p_n, q_n\}_{n=1}^N$, where $p_n \in \mathbb{R}^m$ is n^{th} input data with $q_n \in \mathbb{R}^m$ is class label corresponding to n^{th} data point. For classification of two classes using LS-SVM, discrimination function can be written as [58]:

$$\kappa(x) = \text{sign} [\Omega^T z(p) + \mathbf{b}] \quad (2.13)$$

where Ω is weight vector of dimension x and \mathbf{b} is a bias and $z(p)$ function maps p into x -dimensional space.

LS-SVM classifier decision function can be determined as [58, 60]:

$$\kappa(x) = \text{sign} \left[\sum_{n=1}^N \mathbf{a}_n q_n \mathbf{K}(p, p_n) + \mathbf{b} \right] \quad (2.14)$$

where $\mathbf{K}(p, p_n)$ is kernel function and \mathbf{a}_n is Lagrange multiplier.

In the proposed approach, RBF [61], Morlet and Mexican-hat wavelet kernels [62, 56] are investigate for the classification performance. These kernels are mathematically expressed as:

- The RBF kernel function is expressed as [61, 63]:

$$\mathbf{K}_{RBF}(p, p_n) = \exp \left[\frac{-\|p - p_n\|^2}{2\sigma_1^2} \right] \quad (2.15)$$

- The expression for Morlet wavelet kernel function is given as [62, 56]:

$$\mathbf{K}_{Morlet}(p, p_n) = \prod_{j=1}^N \cos \left[\omega_0 \frac{(p^j - p_n^j)}{a} \right] \exp \left[\frac{-\|p^j - p_n^j\|^2}{2\sigma_2^2} \right] \quad (2.16)$$

- The Mexican-hat kernel function is expressed as [62, 56]:

$$\mathbf{K}_{Mexican-hat}(p, p_n) = \prod_{j=1}^N \left[1 - \frac{(p^j - p_n^j)^2}{a^2} \right] \exp \left[\frac{-\|p^j - p_n^j\|^2}{2\sigma_3^2} \right] \quad (2.17)$$

where p_n^j represents j_{th} element of n_{th} training set, a represents the scaling parameter of wavelet. The symbols σ_1 , σ_2 , and σ_3 are the kernel parameters of RBF, Morlet and Mexican-hat wavelet kernels, respectively.

2.2.8 Performance parameters & cross-validation

The following parameters are employed to measure the classification performance [64] of the proposed approach:

- Sensitivity (Sn): It is also referred to as true positive rate. It is expressed as a ratio of the number of samples correctly classified as a positive class to the

total number of samples in positive class. It is expressed as:

$$Sn = \frac{Tp}{Tp + Fn} \times 100\% \quad (2.18)$$

- Specificity (Sp): It is also known as the true negative rate. It is the ratio of the number of correctly classified samples of negative class to the total number of negative class samples. It is expressed as:

$$Sp = \frac{Tn}{Tn + Fp} \times 100\% \quad (2.19)$$

- Accuracy (Acc): It is expressed as the ratio of total correctly classified samples by the total number of samples. Mathematically written as:

$$Acc = \frac{Tp + Tn}{Tp + Tn + Fp + Fn} \times 100\% \quad (2.20)$$

The correctly classified samples of the positive and negative class are denoted by Tp and Tn , respectively. On the other hand, Fp and Fn are incorrectly classified samples of negative and positive class, respectively.

Cross-validation is a method which evaluates the performance of the machine learning model. In the proposed approach, K-fold cross-validation strategy [65] is employed to evaluate the classifier performance. In this method, the data is divided into K equal parts. Of the k parts, a single part is retained for testing the model, and the remaining k-1 parts are used as the training data. This process is then repeated K times so that each of the k parts has been exactly used once as the testing data. Further, the final performance metric is obtained by averaging the results of each k part. The performance evaluation of the proposed approach using this method is robust as each of the samples in data has been tested exactly once. In the proposed approach, three-fold and ten-fold cross-validations are explored for performance evaluation.

2.3 Dataset and experimental results

This section describes the fundus image dataset employed to validate the performance of the proposed approach. Further, this section also presents experimental results and discussion.

2.3.1 Dataset

The following datasets are employed in the proposed approach:

1. Private database: This database consists of 30 normal and 30 open-angle glaucoma images. These images are obtained from Kasturba Medical College, Manipal, India. The doctors of ophthalmology department have certified the image quality and its usability. The image is stored in 24-bit JPEG format with a resolution of 560×720 pixels.
2. Public database: It consists of 255 normal and 200 glaucoma images. This database is obtained from Medical Image Analysis Group (MIAG) and is available online publicly at <http://medimrg.webs.u11.es/>. The images are stored in a 24-bit JPEG file format with various resolutions.

2.3.2 Results & discussion

In the proposed approach, the fundus image is separated into R, G, B, and grey channels. Four EWT components are obtained from each channel, and three correntropy features are extracted from each EWT component. Therefore, the length of the feature vector is 12 for each channel of the fundus image. Further, the features are ranked and fed to the LS-SVM classifier. These ranked features are tabulated in Tables 2.1-2.4 for private database. The classifier kernel parameters σ_1 , σ_2 , and σ_3 are varied from 0.1 to 1 with a step size of 0.1. The value of ω_0 is set to 0.3 for Morlet wavelet kernel by trial and error method.

Table 2.5 tabulates the classification performance for different channels along with the number of features and kernel functions using three-fold cross-validation for the private database. Similarly, Table 2.6 tabulates the classification performance for ten-fold cross-validation. It can be observed from Table 2.5 that G channel

2.3. Dataset and experimental results

Table 2.5: Classification performance of the proposed approach using three-fold cross-validation for private database.

Channel/Image	Number of features	Kernel (parameter)	Acc (%)	Sn (%)	Sp (%)
R	6	RBF ($\sigma_1 = 0.9$)	91.67	86.67	96.67
R	6	Morlet ($\sigma_2 = 1$)	90.00	83.33	96.67
R	2	Mexican-hat ($\sigma_3 = 0.3$)	90.00	90.00	90.00
G	4	RBF ($\sigma_1 = 0.3$)	98.33	100	96.67
G	4	Morlet ($\sigma_2 = 0.6$)	98.33	96.67	100
G	4	Mexican-hat ($\sigma_3 = 0.4$)	95.00	96.67	93.33
B	4	RBF ($\sigma_1 = 0.5$)	90.00	83.33	96.67
B	3	Morlet ($\sigma_2 = 0.5$)	88.33	83.33	93.33
B	2	Mexican-hat ($\sigma_3 = .6$)	88.33	83.33	93.33
grayscale	6	RBF ($\sigma_1 = 0.5$)	96.67	93.33	100
grayscale	6	Morlet ($\sigma_2 = 0.9$)	93.33	90.00	96.67
grayscale	5	Mexican-hat ($\sigma_3 = 0.5$)	93.33	93.33	93.33

Table 2.6: Classification performance of the proposed approach using ten-fold cross-validation for private database.

Channel/Image	Number of features	Kernel (parameter)	Acc (%)	Sn (%)	Sp (%)
R	5	RBF ($\sigma_1 = 0.9$)	90.00	83.33	96.67
R	5	Morlet ($\sigma_2 = 1$)	88.33	83.33	93.33
R	2	Mexican-hat ($\sigma_3 = 1$)	86.67	93.33	80.00
G	4	RBF ($\sigma_1 = 0.3$)	96.67	100	93.33
G	4	Morlet ($\sigma_2 = 0.5$)	96.67	96.67	96.67
G	4	Mexican-hat ($\sigma_3 = 0.4$)	95.00	96.67	93.33
B	3	RBF ($\sigma_1 = 0.4$)	88.33	83.33	93.33
B	3	Morlet ($\sigma_2 = 0.7$)	88.33	83.33	93.33
B	3	Mexican-hat ($\sigma_3 = 1$)	90.00	90.00	90.00
grayscale	5	RBF ($\sigma_1 = 0.6$)	93.33	90.00	96.67
grayscale	6	Morlet ($\sigma_2 = 1$)	91.67	86.67	96.67
grayscale	2	Mexican-hat ($\sigma_3 = 0.3$)	90.00	96.67	83.33

obtains maximum classification accuracy of 98.33% with RBF and Morlet wavelet kernels using three-fold cross-validation. Similarly, for ten-fold cross-validation, G channel obtains maximum classification accuracy of 96.67% with RBF and Morlet wavelet kernel. It can also be noticed from both the tables that the RBF obtains the maximum classification accuracy for other channels.

Figs. 2.8 and 2.9 show the plot of accuracy versus kernel function parameters for different channels with three-fold and ten-fold cross-validations, respectively for private database. The highest classification accuracy for corresponding kernel parameter values are marked with an ellipse as illustrated in Figs. 2.8 and 2.9.

The performance of the proposed approach is also evaluated for the public

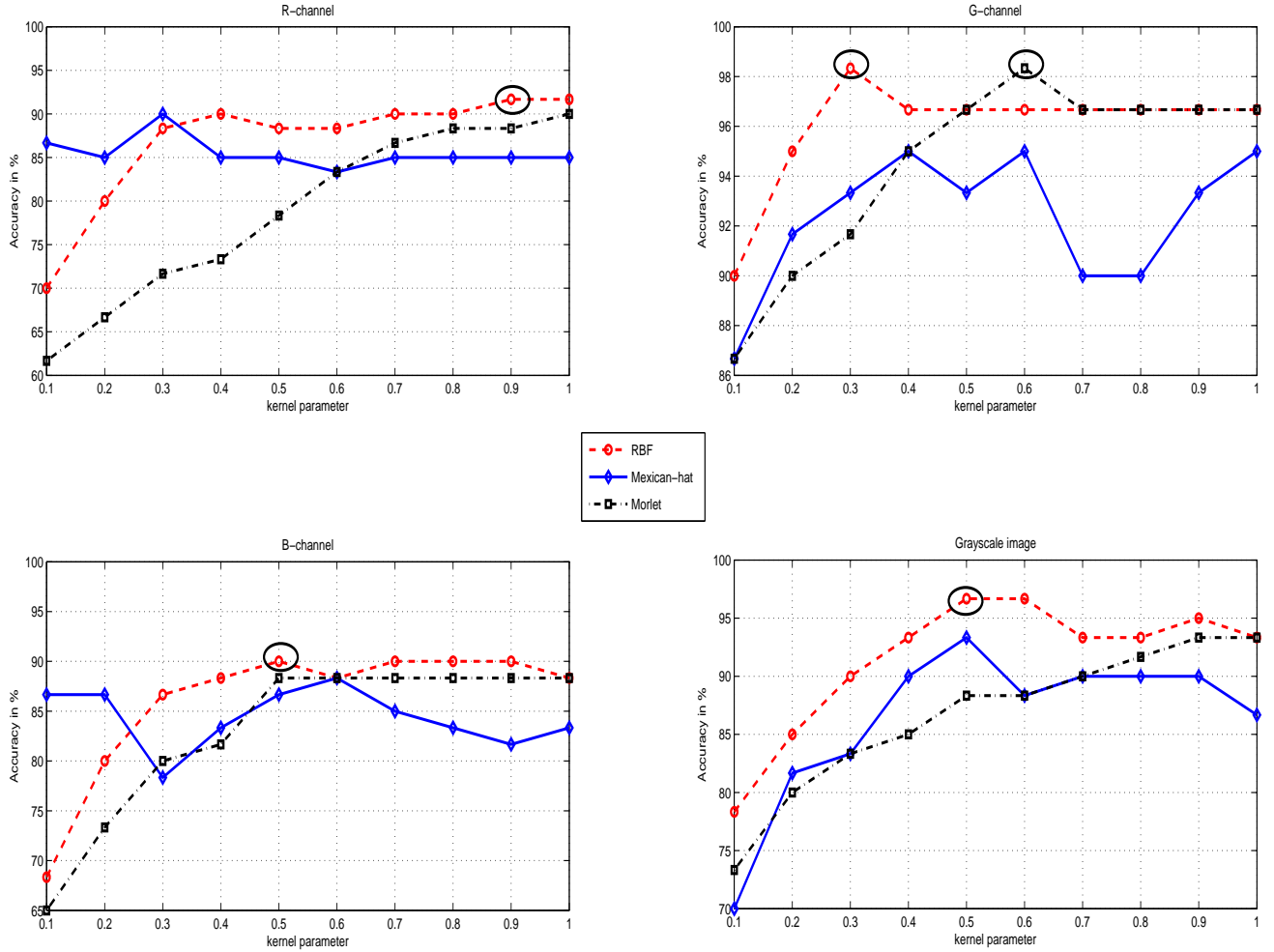


Figure 2.8: Plot of accuracy versus kernel parameters using three-fold cross validation strategy for private database.

database. The classification performance for the public database is tabulated in Tables 2.7 and 2.8 for three-fold and ten-fold cross-validations, respectively. The maximum classification accuracy of 81.32% and 80.66% is obtained using three-fold and ten-fold cross-validations, respectively.

The experimental evaluation suggests that the proposed approach has been found useful for glaucoma diagnosis. The EWT separates the fundus image channels into components of different spatial frequency. In the proposed approach, we have employed the Littlewood-Paley extension of 2D EWT. This decomposes the image data based on the energy separation in frequency spectrum [44]. This energy separation in different frequency components is then captured as the textural features for classification.

Table 2.7: Classification performance of the proposed approach using three-fold cross-validation for public database.

Channel/Image	Number of features	Kernel (parameter)	Acc (%)	Sn (%)	Sp (%)
R	12	RBF ($\sigma_1 = 0.3$)	80.01	75.05	83.92
R	12	Morlet ($\sigma_2 = 1$)	79.78	74.49	83.92
R	1	Mexican-hat ($\sigma_3 = 0.3$)	75.17	62.05	85.49
G	12	RBF ($\sigma_1 = 0.5$)	80.45	75.03	84.71
G	11	Morlet ($\sigma_2 = 1$)	80.44	74.98	84.71
G	2	Mexican-hat ($\sigma_3 = 0.7$)	75.39	60.03	87.45
B	12	RBF ($\sigma_1 = 0.3$)	81.09	78.50	83.14
B	11	Morlet ($\sigma_2 = 0.8$)	81.32	78.99	83.14
B	3	Mexican-hat ($\sigma_3 = .7$)	75.61	57.00	90.20
grayscale	12	RBF ($\sigma_1 = 0.4$)	81.10	77.01	84.31
grayscale	12	Morlet ($\sigma_2 = 1$)	80.44	79.01	81.57
grayscale	3	Mexican-hat ($\sigma_3 = 0.9$)	75.17	63.52	84.31

Table 2.8: Classification performance of the proposed approach using ten-fold cross-validation for public database.

Channel/Image	Number of features	Kernel (parameter)	Acc (%)	Sn (%)	Sp (%)
R	12	RBF ($\sigma_1 = 0.4$)	79.32	71.00	85.80
R	12	Morlet ($\sigma_2 = 1$)	78.70	74.00	82.45
R	2	Mexican-hat ($\sigma_3 = .6$)	74.97	64.50	83.22
G	12	RBF ($\sigma_1 = 0.3$)	80.26	74.00	85.18
G	12	Morlet ($\sigma_2 = 1$)	80.44	74.00	85.51
G	2	Mexican-hat ($\sigma_3 = 0.2$)	75.62	65.50	83.54
B	12	RBF ($\sigma_1 = 0.3$)	80.44	77.50	82.82
B	11	Morlet ($\sigma_2 = 0.9$)	80.66	78.00	82.78
B	3	Mexican-hat ($\sigma_3 = 1$)	74.96	58.00	88.23
grayscale	12	RBF ($\sigma_1 = 0.4$)	80.63	76.00	84.25
grayscale	12	Morlet ($\sigma_2 = .9$)	80.41	78.00	82.25
grayscale	2	Mexican-hat ($\sigma_3 = 0.9$)	74.93	64.00	83.45

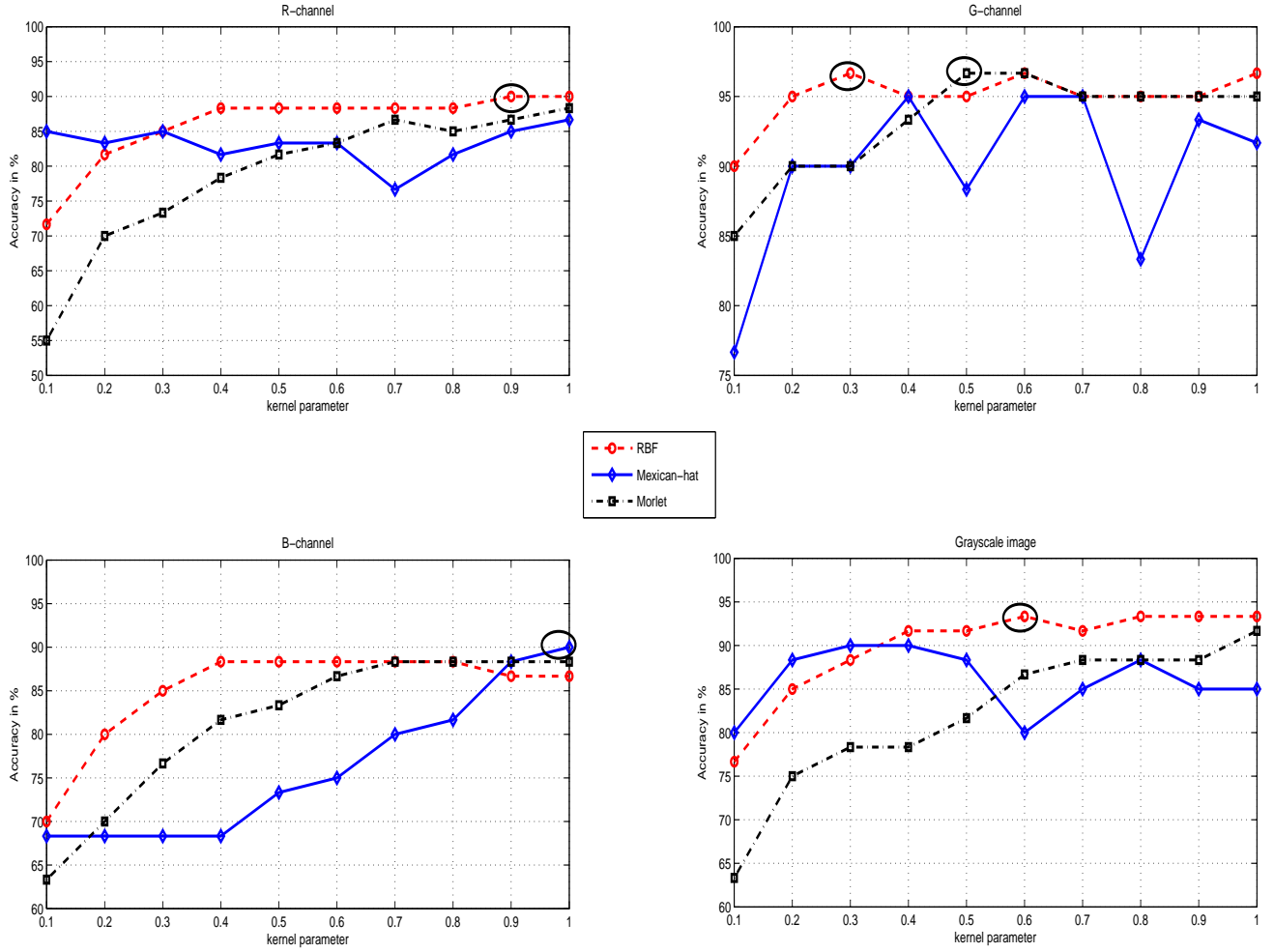


Figure 2.9: Plot of accuracy versus kernel parameters using ten-fold cross validation strategy for private database.

On the other hand, the ridgelet and curvelet extension of 2D EWT decomposes the image data into components based on different angular and radial parameters. Also, in [44], it has been shown that for the same number of decomposed components, Littlewood-Paley extension of 2D EWT effectively separates the frequency information for image type shown in Fig. 2.10(a). Similarly, curvelet and ridgelet work effectively for image type, as shown in Fig. 2.10(b). Therefore, based on the frequency spectrum segmentation technique, we choose Littlewood-Paley for the proposed method as the frequency spectrum of the fundus image (as shown in Fig. 2.10(c)) is closely related to Fig. 2.10(a).

Further, the correntropy successfully incorporates the subtle pixel intensity variations from the decomposed EWT components. The extracted features are then

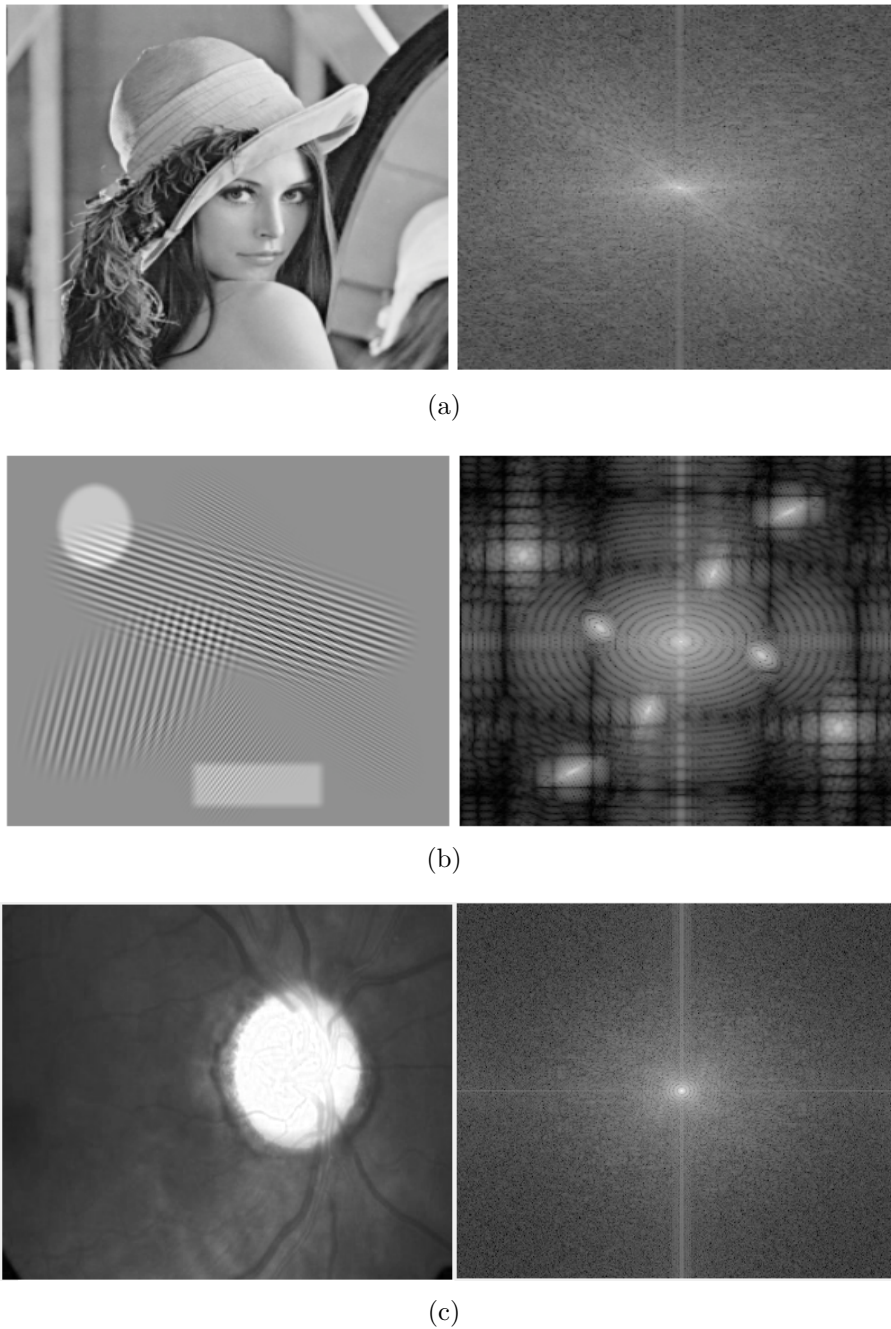


Figure 2.10: (a) Sample image (left) and its Fourier transform (right). (b) Sample image (left) and its Fourier transform (right). (c) Retinal fundus image (left) and its Fourier transform (right) .

classified by SVM with various kernel functions. The kernel parameter is varied from .1 to 1 with a step size of .1. For less or more value of kernel parameter, the kernel function overfits or underfits the training data, respectively. Therefore, instead of fixing the kernel parameter, we have performed our experiments with varying kernel parameter values. From Fig. 2.9 and 2.8, it can be observed that at a particular value of kernel parameter, the kernel function fits the training data

optimally and obtains better classification accuracy (marked by a black ellipse).

From experiments, we have found that the RBF kernel function achieves better performance consistently as compared to Morlet and Mexican-hat wavelet kernels. From Fig. 2.9 and 2.8, it can be observed that in majority of cases, RBF kernel achieves better classification performance compared to other two kernels.

Further, it can be noticed from Table 2.5 and 2.5 that the features extracted from the G channel achieve higher classification performance than other channels. This signifies that the pixel intensity variations in G channel are closely related to the characteristic changes due to glaucoma. The performance of the proposed approach is compared with existing methodologies for glaucoma diagnosis in Table 2.9. It can be noticed from Table 2.9 that the proposed approach achieves better classification performance with comparatively less number of features than the existing methodologies.

2.4 Summary

In this chapter, the adaptive non-stationary signal analysis approach is proposed. Specifically, the EWT based approach has been proposed for automated diagnosis of glaucoma. Further, the approach employs the correntropy as a feature extracted from EWT components. Student's t test is explored for feature selection and ranking based on the t value. Furthermore, the ranked features have been used for the classification. Various kernels have investigated for the classification and experimentally found that RBF and Morlet wavelet kernels yield high classification performance than Mexican-hat wavelet kernel. The experimental results suggest that the proposed approach has been found to be effective for the glaucoma diagnosis. It is also observed that the features extracted from the green channel achieves high accuracy as compared to other channels. This suggests that the pixel variations in the green channel are more prone to detect glaucoma changes.

Table 2.9: Comparison of proposed approach with existing methodologies for automated glaucoma detection.

Authors	Method used	Number of features	Classifier	Acc (%)	Sn (%)	Sp (%)
Kolar et al. [21]	Power spectral features	2	SVM	74	NR*	NR
Nayak et al. [17]	Fundus disk parametes	3	ANN	NR	100	80
Bock et al. [22]	PCA, FFT and spline	90	SVM	80	NR	NR
Acharya et al. [23]	HOS bispectrum	12	RF	91	NR	NR
Dua et al. [24]	Wavelet energy	14	SMO	93.33	NR	NR
Mookiah et al. [25]	HOS and wavelet	35	SVM	95	93.33	96.67
Noronha et. al. [26]	HOS cumulants	13	SVM	92.65	100	92
Acharya et al. [27]	Gabor transform	32	SVM	93.10	89.75	96.20
Proposed approach	2D EWT and correntropy	6	LS-SVM	98.33	100	96.67

*NR=Not Reported

Iterative Variational Mode Decomposition of Fundus Images for Glaucoma Diagnosis

In this chapter, an iterative non-stationary signal analysis approach is proposed for the classification of fundus images. Specifically, the proposed approach explores variational mode decomposition (VMD) as an adaptive non-stationary signal analysis. The VMD is applied iteratively on the fundus images. The features extracted from the VMD components are classified into normal and glaucoma classes.

3.1 Introduction

In the preceding chapter, EWT based approach is proposed for glaucoma diagnosis. Specifically, EWT is an adaptive non-stationary signal decomposition method. It decomposes the signal by creating an adaptive filter bank, based on the segmentation of its Fourier spectrum [43]. The segmentation mainly relies on robust detection of the peaks in the Fourier spectrum [66]. However, the peak detection algorithm fails to estimate the number of prominent peaks under shaky or noisy conditions [67]. Also, the explicit tight construction of filter banks depends on parameter selection, which induces some amount of spectral overlap [66].

On the other hand, VMD is an adaptive and non-recursive method of signal decomposition. It decomposes a given signal into the number of VMD components

which are sparsely separated in the frequency domain. Therefore, in this chapter, the VMD based approach is proposed for the glaucoma diagnosis. The VMD decomposition procedure needs the number of components in advance [68]. To overcome this limitation, the iterative method is adopted in the proposed approach. In this study, the 2D version of VMD has been employed for the iterative decomposition of the fundus image.

The rest of the chapter is structured as follows: The proposed approach is presented in Section 3.2, which describes the iterative VMD process, the feature extraction, and the classification process. Section 3.3 details the fundus image dataset and presents the experimental results of the proposed approach. Finally, Section 3.4 summarises the chapter.

3.2 Proposed approach

This section details the steps involved in the proposed approach. Firstly, the overview of the proposed approach is followed by the data preprocessing step. Further, the iterative VMD process is described along with feature extraction and selection method. The classification process is described at the end of the section.

3.2.1 Overview of the proposed approach

This chapter presents an iterative VMD based approach for the automated diagnosis of glaucoma using fundus images. The proposed approach employs the 2D version of the VMD [69] to decompose fundus images in an iterative manner. Firstly, in the proposed approach, the green (G) channel is obtained from the fundus image. Then, the G channel is decomposed into VMD components iteratively. Further, various entropies and fractal dimension are extracted as features from the VMD components. The extracted features are then ranked using the ReliefF feature selection algorithm. Finally, the extracted features are fed to the LS-SVM classifier for discriminating between glaucoma and non-glaucoma class. The performance of the proposed approach is evaluated using three-fold and ten-fold cross-validation methods. The block diagram of the proposed approach is shown in Fig. 3.1.

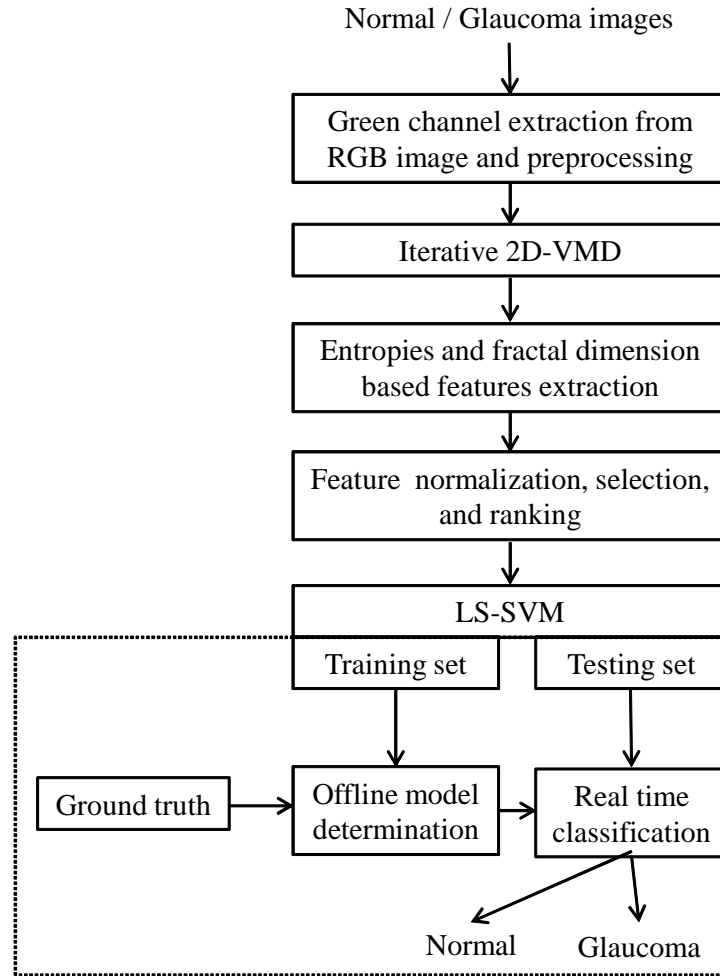


Figure 3.1: Overview of the iterative VMD based approach.

3.2.2 Preprocessing step

Fig. 4.2 shows few sample fundus images. The fundus images have been preprocessed before they are used in the proposed approach. To reduce the computation time, the images are resized to $250 \times (250 * asr)$ by employing bi-cubic interpolation [70] method. To maintain the aspect ratio, the number of columns in the original image is multiplied by the *asr* value. The *asr* is the ratio of the number of columns to the number of rows in the original image. Further, the dynamic range of the fundus images gets affected due uneven illumination of lighting conditions during image acquisition. In order to improve the dynamic range, the fundus images are treated with contrast limited adaptive histogram equalization (CLAHE) [71] [72].

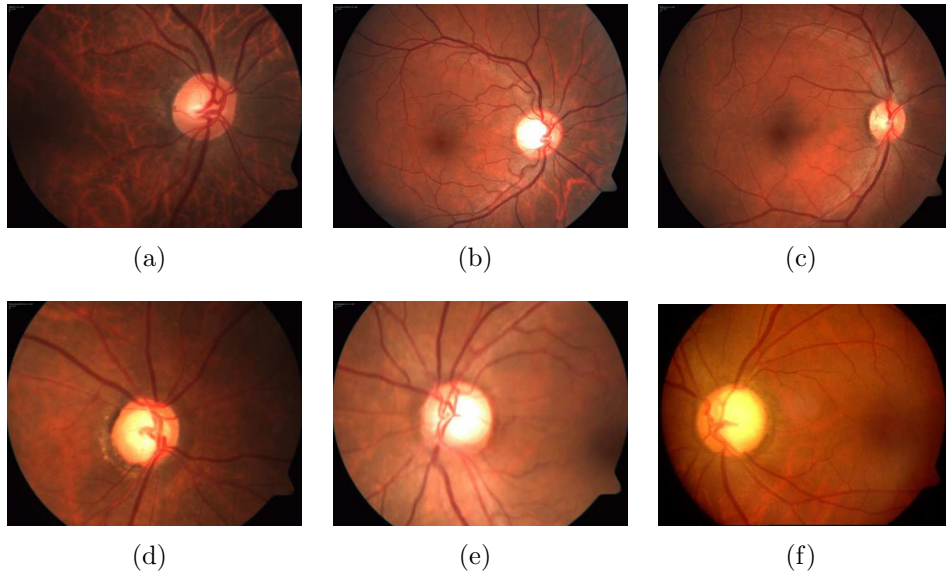


Figure 3.2: Top row: normal fundus images. Bottom row: glaucoma fundus images.

3.2.3 Variational mode decomposition

Variational mode decomposition (VMD) [66], unlike empirical mode decomposition (EMD) [42], is a non-recursive method. The signal decomposition based on EMD highly depends on extremal point finding, interpolation, and stopping criteria. These degrees of freedom and lack of mathematical theory suggest to explore a new robust decomposition method. On the other hand, the VMD is also robust to noise, and improved alternative to the EMD [66].

VMD is an adaptive, and variational technique for the analysis of non-stationary signals [66]. It depends upon the frequency information present in the signal. It decomposes the signal into bandlimited modes, that are centred around a particular frequency and have specific sparsity properties. The VMD decomposes a multi-component signal non-recursively into a discrete number of bandlimited sub-signals. These sub-signals are well sparsely separated in the spectral domain. Each sub-signal after decomposition is bandlimited to centred frequency. The bandwidth of a bandlimited sub-bands are computed as follows [66]:

1. Transform the signal into its analytic counterpart for each sub-band.
2. Exponential term, which is tuned to respective estimated centre frequency, is used to shift the frequency spectrum of each sub-band.
3. The squared L^2 -norm of the gradient is applied to estimate the bandwidth.

For a multi-component signal S , the constrained variational problem for VMD can be formed as [66]:

$$\min_{m_k, \omega_k} \left\{ \sum_k \left\| \partial t \left[\left(\delta(t) + \frac{i}{\pi t} \right) * m_k(t) \right] \exp^{-i\omega_k t} \right\|_2^2 \right\}$$

such that $\sum_k m_k = S$ (3.1)

where m_k and ω_k are the k^{th} decomposed bandlimited VMD component and its center frequency. In Equation (3.1), the constrained problem can be addressed by incorporating quadratic penalty and the Lagrangian multiplier. This equation can be rewritten as [66]:

$$\begin{aligned} \mathfrak{L}(m_k, \omega_k, \beta) = & \alpha \sum_k \left\| \partial t \left[\left(\delta(t) + \frac{i}{\pi t} \right) * m_k(t) \right] \exp^{-i\omega_k t} \right\|_2^2 \\ & + \left\| s(t) - \sum_k m_k(t) \right\|_2^2 + \left\langle \beta(t), s(t) - \sum_k m_k(t) \right\rangle \end{aligned} \quad (3.2)$$

Saddle point of Equation (3.2) with respect to Equation (3.1) can be determined by an alternating direction method of multipliers (ADMM) [66]. The estimate of the k^{th} -mode is updated as follows:

$$\hat{m}_k^{n+1}(\omega) = \frac{\hat{S}(\omega) - \sum_{j \neq k} \hat{m}_j(\omega) + \frac{\hat{\beta}(\omega)}{2}}{1 + 2\alpha(\omega - \omega_k)^2} \quad (3.3)$$

where α is balancing parameter of the data fidelity constraint. The center frequency is updated as center of gravity, which can be written as [66]:

$$\omega_k^{n+1} = \frac{\int_0^\infty \omega |\hat{m}_k(\omega)|^2 d\omega}{\int_0^\infty |\hat{m}_k(\omega)|^2 d\omega} \quad (3.4)$$

In this work, the 2D VMD [69] proposed for images is employed for fundus image decomposition. The 2D-VMD is applied iteratively on G channel of fundus image. The iterative VMD is shown in Fig. 3.3. In the 1st iteration, the fundus image is decomposed into 2 VMD components. Similarly, in rest of the iterations, the

2^{nd} VMD component of the previous iteration is further decomposed into 2 VMD components. In total, there are 5 iterations. Hence, a total of 10 VMD components are obtained from a single G channel of the fundus image. Figs. 3.4 and 3.5 show the iterative VMD components of G channel of normal and glaucoma fundus image, respectively.

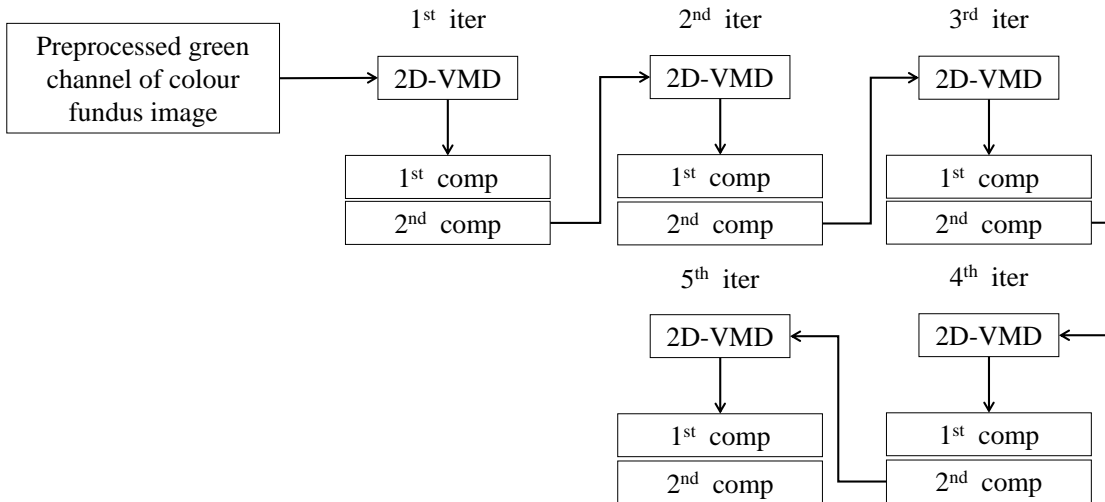


Figure 3.3: Illustration of iterative 2D-VMD. (*iter = iteration, *comp = component)

3.2.4 Feature extraction

Feature extraction process plays an important role in capturing discriminatory information from the data. It replaces the original data by a comparatively less number of discriminatory attribute referred to as features. In the proposed approach, various entropies and fractal dimension are extracted as features from the VMD components. These features incorporates the smoothness, coarseness, and pixel irregularities of the VMD components.

Entropy is the measure of uncertainty and randomness [73]. Equal distribution of pixels intensity values leads to no information and hence zero entropy. In this work, non-Shannon entropies are explored which have higher dynamic range and make better estimation of regularity and scattering [74]. In this approach, entropies such as Renyi entropy (RE) [75], Yager entropy (YE) [74], and Kapur entropy (KE) [75] are extracted from the VMD components. Let p_x denote the probability of pixel value x occurred y number of times and let image size be $r \times c$, then p_x can

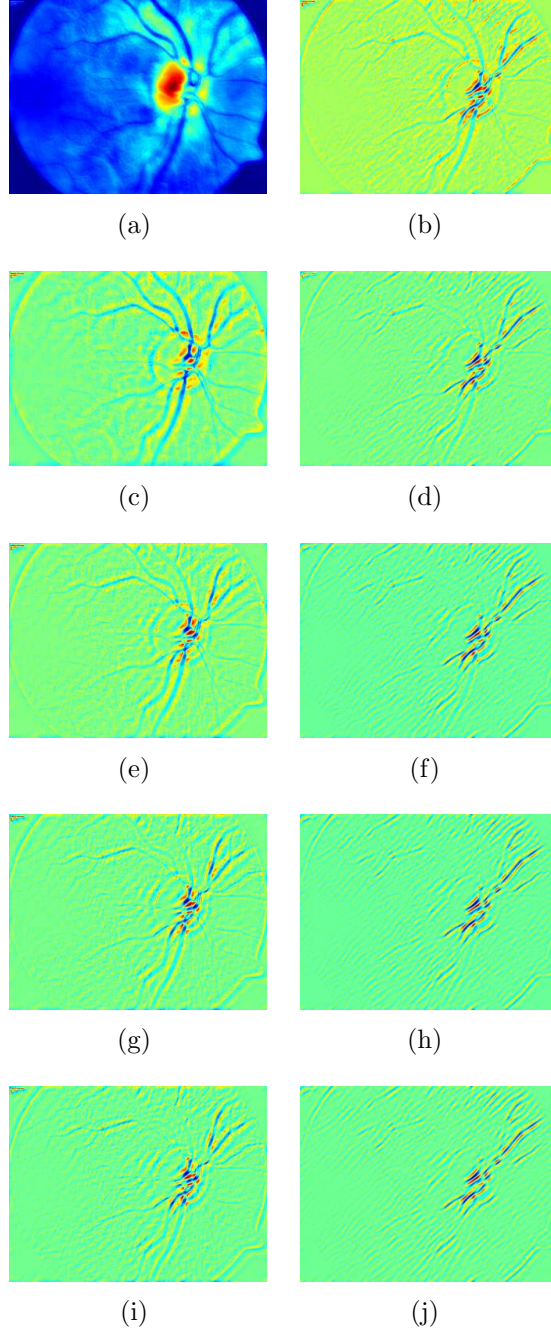


Figure 3.4: Iterative VMD components of G channel of fundus image in Fig. 3.2(a).

be expressed as $p_x = \frac{y}{r \times c}$. The KE, RE, and YE can be expressed as [74]:

$$\text{KE} = \frac{1}{\mathbf{b} - \mathbf{a}} \log_2 \left(\frac{\sum_{x=0}^{X-1} p_x^{\mathbf{a}}}{\sum_{x=0}^{X-1} p_x^{\mathbf{b}}} \right) \quad (3.5)$$

$$\text{RE} = \frac{1}{\mathbf{1} - \alpha} \log_2 \left(\sum_{x=0}^{X-1} p_x^{\alpha} \right) \quad (3.6)$$

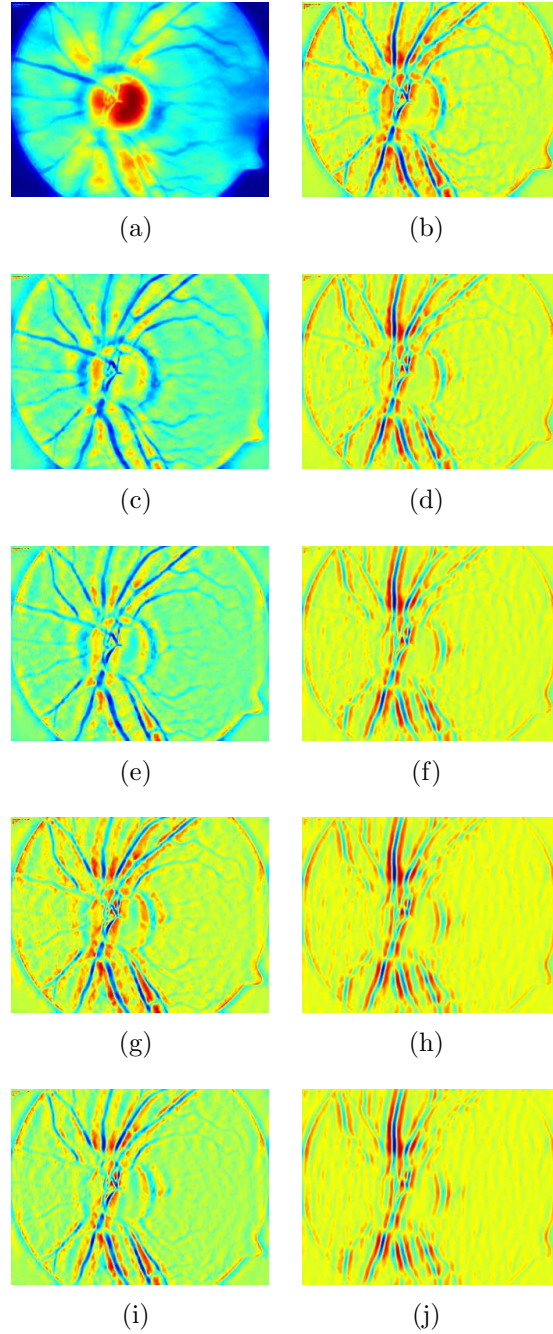


Figure 3.5: Iterative VMD components of G channel of fundus image in Fig. 3.2(e).

$$YE = 1 - \frac{\sum_{x=0}^{X-1} |2p_x - 1|}{|r \times c|} \quad (3.7)$$

Fractal Dimension: Fractals are the objects with self-similarity and irregularity [76]. The FD is a measure of roughness, self-similarity and irregularity. It is very useful for studying texture as it has scale-dependent property [77]. To investigate

the textural differences in the normal and glaucoma images, FD is explored in the proposed approach. The high value of FD indicates higher roughness of the surface texture [78].

If a surface S , scaled up or down by a factor f , is self-similar only if S is a union of non-overlapping copies (S_f) of itself when scaled. The self-similarity measured by FD as [76]:

$$1 = S_f f^{FD} \quad (3.8)$$

which can also be re-written as:

$$FD = \frac{\log(S_f)}{\log\left(\frac{1}{f}\right)} \quad (3.9)$$

where

$$f = \frac{\text{scaled value}}{\text{original scale}} \quad (3.10)$$

Differential box counting (DBC) [77] algorithm is used to determine FD. In this work, the sequential box-counting (SBC) [76] method is employed for computing FD. The modified DBC technique is named as sequential box counting (SBC). In the SBC method, the initial grid size is set to the power of 2 and the final grid is set to image size ($r \times c$). The S_f in Equation 3.8 is the sum of differences of maximum and minimum intensities of each 2×2 grid. This is repeated until the size of the grid is equal to the image size. Previously, the FD is successfully explored for the characterization of ovarian tumour [78] and epileptic seizures [79].

3.2.5 Feature Normalisation

Skewed data may result in a false alarm and may hamper the performance of the classifier. Feature normalisation brings the numeric values of the features within the desired range. In this work, z-score normalisation [51] has been used, which transform the data into *zero* mean and *unit* deviation. If X is data, then the normalised data \hat{X} using z-score procedure can be expressed as [80]:

$$\hat{X} = \frac{X - \text{mean}(X)}{\text{std}(X)} \quad (3.11)$$

where std is standard deviation.

3.2.6 Feature selection

Feature selection is a crucial stage in the computer-aided automated diagnosis. Not all the extracted features behave similarly. Some features with lower discriminatory ability may disturb the performance of the proposed approach [23]. Moreover, training the machine learning algorithm with a large number of features may lead to over-fitting [78]. Therefore, selecting feature subset which has significant discrimination capability will maximise the classification performance of the method.

In the proposed approach, ReliefF feature selection method [81] is employed. This method is an improved version of Relief feature selection method proposed by Kira et al. in [82]. Statistical methods are used in ReliefF feature selection method instead of heuristic search, and it selects statistically relevant features. The input to the ReliefF algorithm is feature vector and class labels. Pseudocode for ReliefF feature selection algorithm is explained in Algorithm 1 [81].

Algorithm 1 ReliefF feature selection algorithm pseudocode

```

initialize  $W[A] := 0.0$ ;
for  $i := 1$  to  $m$  do
    randomly select  $R_i$ ;
    find  $k$  nearest hits  $H_j$ ;
    for each class  $C \neq \text{class}(R_i)$  do
        from class  $C$  find  $k$  nearest misses  $M_j(C)$ ;
    end for
for  $A := 1$  to  $a$  do

```

$$W[A] := W[A] - \sum_{j=1}^k \text{diff}(A, R_i, H_j) / (m.k) + \sum_{C \neq \text{class}(R_i)} \left[\frac{P(C)}{1 - P(\text{class}(R_i))} \sum_{j=1}^k \text{diff}(A, R_i, M_j(C)) \right] / (m.k)$$

```

    end for
end for

```

In ReliefF feature selection method, an instance R_i is randomly selected and

Table 3.1: Results of features ranked using ReliefF method.

Feature	Normal (<i>mean</i> \pm <i>std</i>)	Glaucoma (<i>mean</i> \pm <i>std</i>)
KE_1^1	7.465 \pm 0.121	7.444 \pm 0.162
FD_1^5	1.935 \pm 0.008	1.919 \pm 0.010
FD_1^4	1.949 \pm 0.009	1.930 \pm 0.012
FD_1^3	1.971 \pm 0.012	1.949 \pm 0.017
RE_1^5	0.391 \pm 0.102	0.284 \pm 0.147
FD_2^5	2.098 \pm 0.033	2.029 \pm 0.040
FD_1^2	2.010 \pm 0.016	1.982 \pm 0.024
RE_1^1	6.145 \pm 0.259	5.583 \pm 0.668
RE_2^1	1.375 \pm 0.065	1.285 \pm 0.131
FD_2^4	2.110 \pm 0.032	2.040 \pm 0.040
YE_1^2	0.999 \pm 4.58 $\times 10^{-05}$	0.999 \pm 7.13 $\times 10^{-05}$
KE_1^4	2.078 \pm 0.235	1.828 \pm 0.452
KE_1^3	2.540 \pm 0.260	2.330 \pm 0.530
FD_2^3	2.124 \pm 0.032	2.055 \pm 0.040
KE_1^5	1.753 \pm 0.218	1.480 \pm 0.400
RE_1^4	0.550 \pm 0.121	0.430 \pm 0.191
FD_2^2	2.144 \pm 0.031	2.075 \pm 0.040
RE_1^2	1.127 \pm 0.120	0.978 \pm 0.237

then searches for k nearest neighbors from the same and different classes termed as nearest hits H_j and misses $M_j(C)$, respectively. Depending upon the values of R_i , H_j , and $M_j(C)$, the quality estimation $W[A]$ is updated. Parameter k is user defined and generally set to 10 [81]. The difference between the values of the attribute A for two instances I_1 and I_2 is calculated by $\text{diff}(A, I_1, I_2)$ function. Based on the value of W , the features are ranked and first eighteen features are further selected for classification. Table 3.1 lists the selected eighteen features. Column 1 of Table 3.1 lists the features in the form X_y^z where X represents feature and y and z represent the component and iteration number, respectively.

3.2.7 Classification

Classifiers play an important role in computer-based diagnosis applications. They create a decision boundary to discriminate between two or more classes. Various biomedical signals such as for heart sound [52], electroencephalogram [53], and heart rate [50] have employed support vector machine (SVM) classifier [58, 59]. In the proposed approach, LS-SVM is employed, which is a supervised machine learning algorithm and has previously been used in computer-based glaucoma diagnosis [80]. In this work, to separate non-linear features using LS-SVM, a non-linear kernel function is employed which maps the input feature space into a higher dimensional space in order to make them linearly separable. Specifically, radial basis function (RBF) [61] is investigated as a non-linear kernel function in this work.

3.3 Dataset and experimental results

The fundus image dataset is described in this section. This section also presents experimental results of the proposed approach validated on the described dataset.

3.3.1 Dataset

In this work, the dataset consists of 488 fundus images obtained from Kasturba Medical College, Manipal, India, has been employed for glaucoma diagnosis. The doctors of the ophthalmology department of the college have provided permission for the usage of these fundus images. Sample normal and glaucoma digital fundus images are shown in Fig. 3.2. Moreover, in this study, the online available public database obtained from <http://medimrg.webs.u11.es/> is used to validate our proposed method. This database consists of 255 normal and 200 glaucoma fundus images.

3.3.2 Results & discussion

In the proposed method, VMD is iterated five times, with two VMD components per iteration, which produces ten VMD components per fundus image. Four features are extracted from each VMD component. Therefore, the length of the feature

vector is 40 per fundus image. Further, a subset of eighteen features is selected from the ranked features. The selected features are then fed to the classifier. Accuracy, sensitivity, and specificity are employed as the performance metric in the proposed approach [64]. The kernel parameter σ for RBF kernel is varied from 0.2 to 2 with 0.1 increment. To evaluate the classifier performance, three-fold and ten-fold cross-validation strategies [64] are employed.

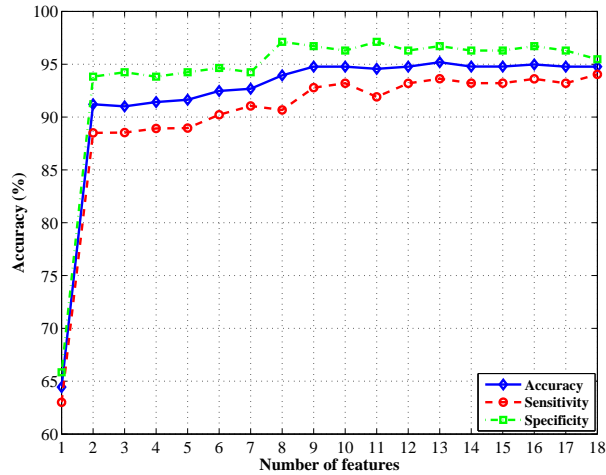
The proposed approach achieves the maximum classification accuracy using the first 13 features. The three-fold and ten-fold cross-validation obtains the classification accuracy of 95.19% and 94.79%, respectively. The plots of performance parameters versus the number of features and kernel parameter are shown in Fig. 3.6 and Fig. 3.7, respectively for three-fold and ten-fold cross-validation strategies.

Further, the proposed method is also evaluated for the public database. The classification accuracy of 81.63% and 81.22% has been obtained for three-fold and ten-fold cross-validation strategies, respectively. The reason for less accuracy of the proposed method on the public database is due to diverse fundus images with different image resolutions and varying illumination changes.

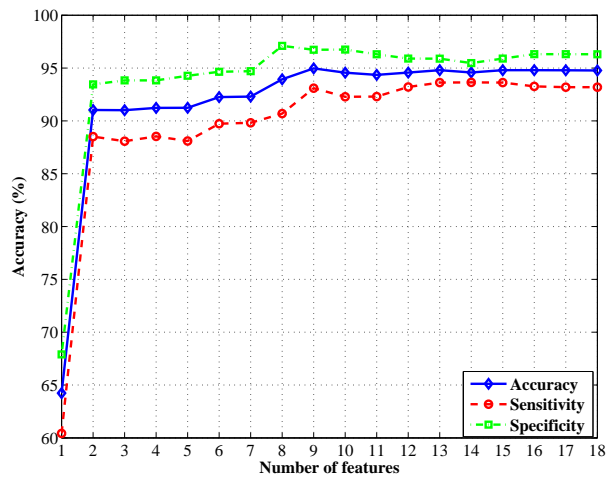
The extracted features from G channel of the fundus image are more effective for glaucoma diagnosis as compared to red (R) and blue (B) channels [21], [80], [83]. They incorporate the subtle variation in pixel intensities that characterises the glaucoma change. Therefore, in the proposed approach, only the G channel of the fundus image is considered for further analysis.

In adaptive decomposition based image analysis, the number of decomposed components play an important role. The VMD has a limitation that it needs the number of components in advance [68]. To overcome this limitation, the iterative method is adopted in the proposed approach. The VMD is applied iteratively, as shown in Fig. 3.3. The iterative process narrows the frequency band of the subsequent VMD component. This narrowing process separates the closely related pixel variations, which are further captured by various entropies and fractal dimension.

The number of iterations is kept 5 in the proposed method. We have also performed our experiments up to 8th iterations. However, the features extracted from those (6th to 8th) iterations does not contribute to the performance enhancement as there is no significant improvement in classification accuracy. Additionally, the



(a)

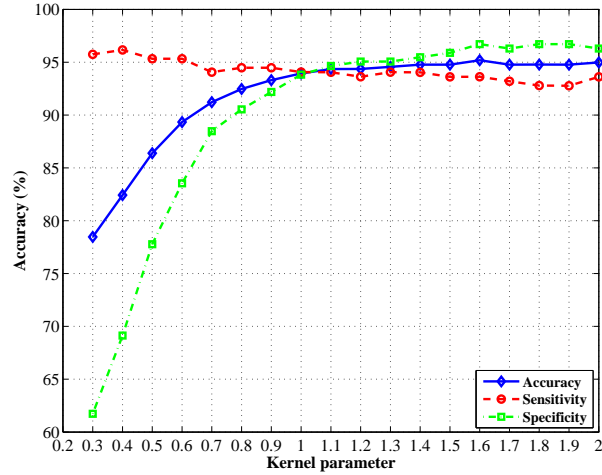


(b)

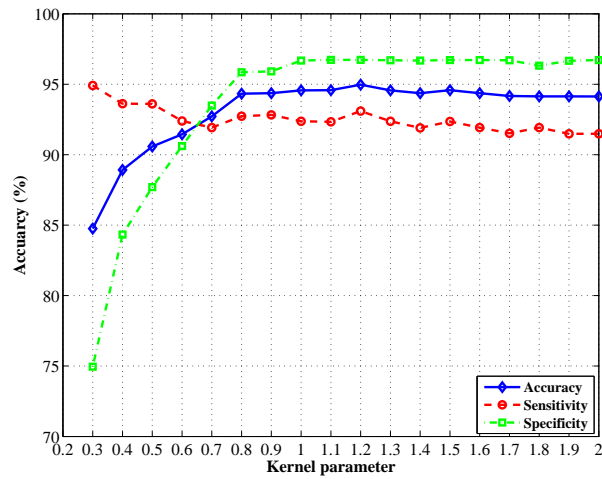
Figure 3.6: Plot of accuracy versus number of features for (a.) three-fold, and (b.) ten-fold cross validation strategies.

feature subset chosen for classification using feature selection does not involve the features extracted from 6th to 8th iterations. Further, an increase in the number of modes will result in more computational time and number of features. Therefore, we have restricted our experiments up to 5 iterations only. Further, the extracted features are ranked, and the subset of features is selected from the ranked features. The feature selection improves the classification performance of the approach by avoiding features with lower discriminating capability.

The experimental results suggest that the features extracted from the iterative VMD components are effective for automated glaucoma diagnosis. In Table 3.1, it can be noted that all feature values are high for a normal class. It means that there is



(a)



(b)

Figure 3.7: Plot of accuracy versus kernel parameter for first-thirteen features with (a.) three-fold, and (b.) ten-fold cross validation strategies.

more pixel variation in the normal class. In glaucoma, due to a large optic cup (OD) which signifies increased white region, pixel variation will be less causing reduction in the feature values. Existing methodologies proposed for automated diagnosis of glaucoma have been presented in Table 3.2. It can be observed from Table 3.2 that the proposed approach achieves better classification performance than the existing state-of-the-art methodologies.

Table 3.2: Comparison table of existing techniques for automated glaucoma detection.

Authors	Method used	Number of images	Number of features	Cross validation	Classifier	Acc (%)	Sn (%)	Sp (%)
Nagarajan et al. [11]	MEVP	399	-	Split test	ANN	94	95	94
Townsend et al. [84]	HRT parameters	200	10	Eight fold & leave-one-out	SVM	87.5	NR*	NR
Kolar et al. [21]	Fractal descriptor	30	2	Split test & leave-one-out	SVM	74	NR*	NR
Nayak et al. [17]	Fundus disk parameters	61	3	Split test	ANN	90	100	80
Bock et al. [22]	PCA, FFT & spline	575	90	Five fold	SVM	80	73	85
Acharya et al. [23]	HOS & texture features	60	12	Five fold	RF	91	NR	NR
Dua et al. [24]	DWT & texture features	60	14	Ten fold	SMO	93	NR	NR
Mookiah et al. [25]	HOS & wavelet energy feature	60	13	Three fold	SVM	95	93.33	96.67
Noronha et al. [26]	HOS cumulant features	272	35	Ten fold	Naïve Bayesian	92.60	100	92
Acharya et al. [27]	Gabor transformation & texture and entropy features	510	23	Ten fold	SVM	93.10	89.75	96.20
Maheshwari et al. [80]	EWT & correntropy	60	6	Ten fold & three fold	LS-SVM	96.67	100	93.33
Proposed methodology	VMD, entropy & fractal dimension	488	13	Ten fold & Three fold	LS-SVM	94.79	93.62	95.88
						95.19	93.62	96.71

*NR=Not Reported

3.4 Summary

In this chapter, an iterative VMD-based approach is proposed for automated diagnosis of glaucoma. The G channel of fundus image is decomposed into VMD components iteratively. Further, various entropies and fractal dimension have been extracted as the features. Further, the extracted features are ranked and only significant features with high discriminating capability are selected and fed to the classifier. The experimental results suggest that the features extracted from iterative VMD components have been found to be effective for glaucoma diagnosis. Specifically, Renyi entropy, Kapur entropy, and fractal dimension efficiently capture the subtle variation in the pixel intensities in the VMD decomposed components. Hence, the proposed approach has been validated on 488 fundus images and obtains better classification performance than the state-of-the-art glaucoma diagnosis approaches.

Local Bit-Level Texture Descriptor for Glaucoma Diagnosis

In this chapter, unlike grey-level texture descriptor, the local bit-level texture descriptor is developed for glaucoma diagnosis. The proposed approach employs bit-plane slicing (BPS) followed by local binary pattern (LBP), which generates LBP images. Further, the features are extracted from the LBP images and fed to the classification process. Finally, the decision level fusion is explored to combine the predictions of different classifiers.

4.1 Introduction

In Chapters 2 and 3, EWT and VMD based methodologies have been proposed for glaucoma diagnosis, respectively. Both EWT and VMD decomposes the signal into a number of time-frequency components. In EWT, the Fourier axis segmentation in noisy conditions fails to estimate prominent peaks. This results in irrelevant EWT components [67]. On the other hand, VMD has a limitation that it needs the number of components in advance [68]. To overcome this limitation, the iterative approach is proposed. However, these signal decomposition techniques are computationally complex as they involve a large number of complicated steps to decompose a signal.

In this chapter, the local bit-level texture descriptor is proposed. The proposed approach employs BPS and local binary patterns (LBPs). The computation of LBP is simple and involve less number of operations [85], which makes the proposed

approach computationally efficient.

Other sections of the chapter are organised as follows: The proposed approach is described in Section 4.2, which elaborates BPS followed by LBP description, feature extraction, and the classification process. The fundus image dataset is described in Section 4.3, which also presents experimental results and discussion. Finally, the chapter is summarised in Section 4.4.

4.2 Proposed approach

This section starts with an overview of the proposed approach. Then, it discusses the preprocessing step followed by BPS method, and the LBP based feature extraction process. At last, the classification process is discussed.

4.2.1 Overview of the proposed approach

In this chapter, local bit-level texture descriptor is developed for glaucoma diagnosis. This approach employs BPS, followed by LBP. Initially, the BPS split each preprocessed fundus image channel into bit planes. Then, the LBP images are obtained from the bit planes of each channel. Further, corresponding to each channel, the features are extracted from LBP images and are subjected to normalization and ranking. The ranked feature vectors of each channel are then fed to separate classifiers. The performance of the proposed approach is investigated on 2^{nd} and 3^{rd} order polynomial kernels. Finally, to combine the individual predictions of classifiers, the decision level based fusion has been employed. The block diagram of the proposed methodology is illustrated in Fig. 4.1.

4.2.2 Preprocessing of fundus images

A few sample images are shown in Fig. 4.2. The proposed methodology starts with a preprocessing step. Firstly, the fundus image is resized to 360×480 pixels to decrease the computation time. Secondly, the resized fundus image is separated into the red (R), green (G), and blue (B) channels. Finally, each of these channels goes through contrast limited adaptive histogram equalization (CLAHE) [71] [72]

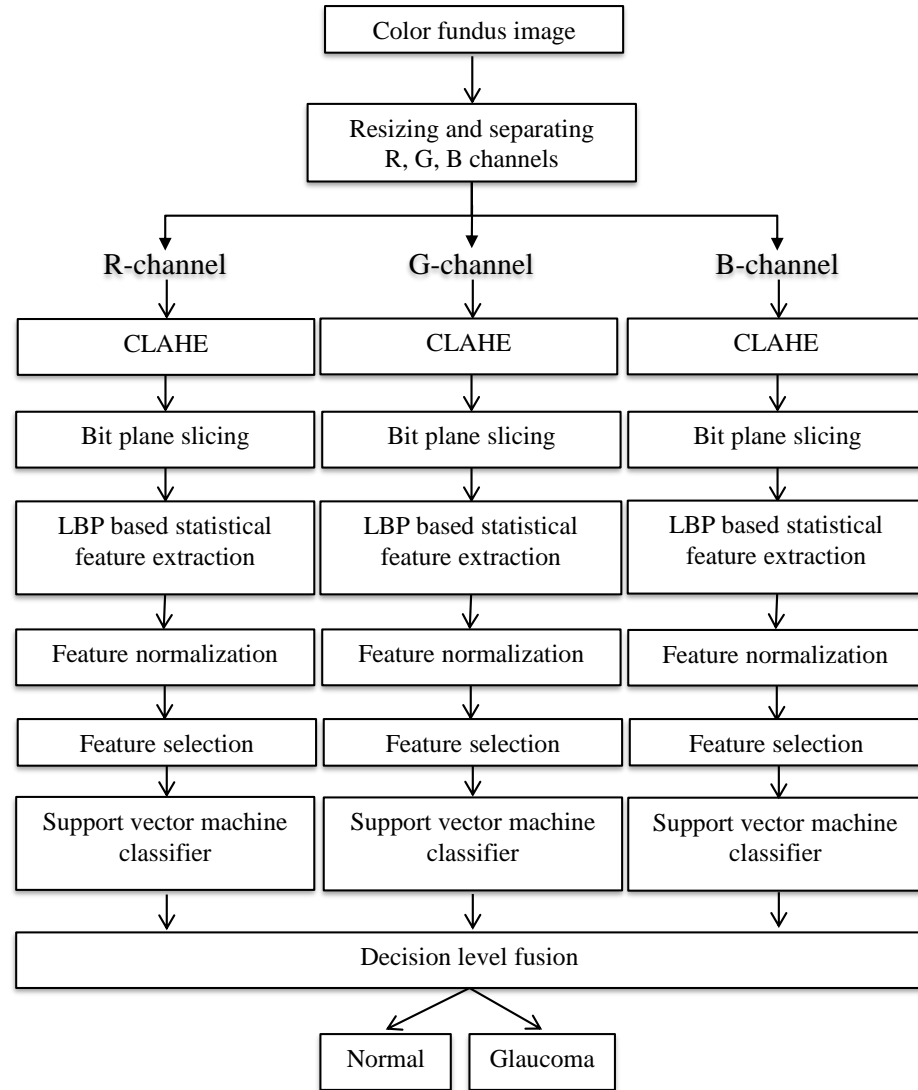


Figure 4.1: Block diagram of the local bit-level texture descriptor approach.

to overcome the problem of uneven lighting conditions at the time of fundus image acquisition.

4.2.3 Bit plane slicing

BPS [71] is a technique which splits a grey image into the bit planes. In general, a 256-level grey-scale image is composed of 8-bits and therefore BPS splits it into 8 bit planes. Correspondingly, each R, G, and B channel is a 8-bit grey-scale image which splits into 8 bit planes. BPS is useful for analyzing the relative importance of each bit plane, which can be processed further to extract the discriminating information. Fig. 4.3 shows the bit planes of the R channel of glaucoma image shown in Fig. 4.2(e). Fig. 4.3(a) shows the 1st bit plane that corresponds to least significant bit

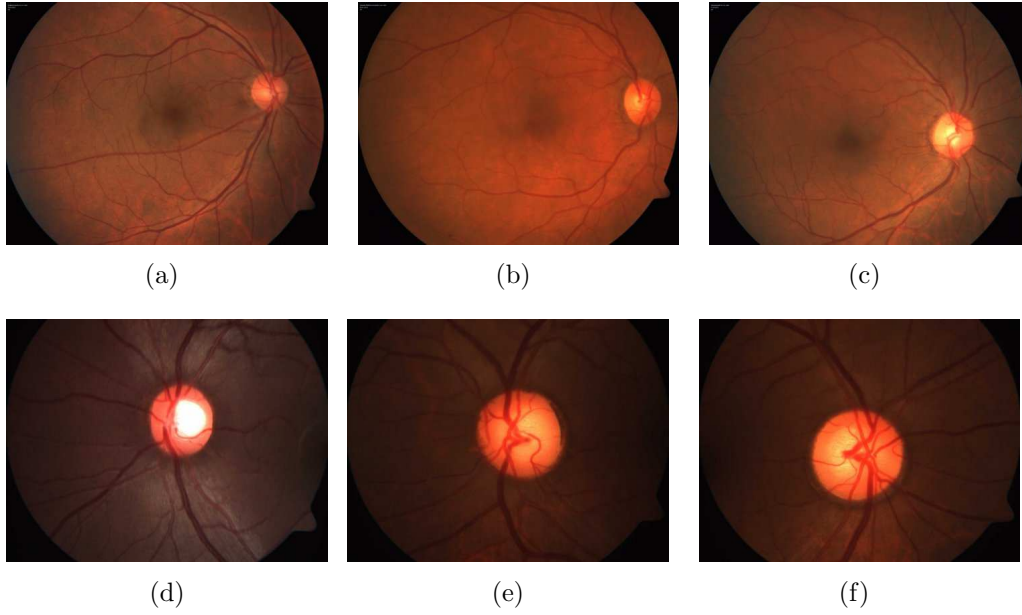


Figure 4.2: Sample fundus images: normal (top row) and glaucoma (bottom row) class.

(LSBs) plane. Similarly, Figs. 4.3(b) - 4.3(h) show the remaining bit planes.

4.2.4 Local binary patterns based feature extraction

The analysis of two-dimensional texture has been investigated extensively for applications involving image classification. In real world, textures are often irregular due to orientation, scale, lightening conditions [85]. Most of the discriminating problems rely heavily on how effectively the variations in texture is captured.

The LBP [85] is a simple and effective image texture descriptor that has been widely used for diverse applications. To capture the local changes in each of the bit planes, LBP is employed. LBP is computed by performing logical operations in the local neighbourhood of a predefined window. More specifically, the computation of LBP involves two steps. In the first step, each of the neighbouring pixels is thresholded against the centre pixel value to generate a binary pattern. In the second step, the binary pattern is converted into its equivalent decimal value. This decimal value is considered the LBP of the corresponding centre pixel.

Since the bit planes are already in binary form, the second step is directly performed to compute the LBP. Mathematically, it is computed as follows:

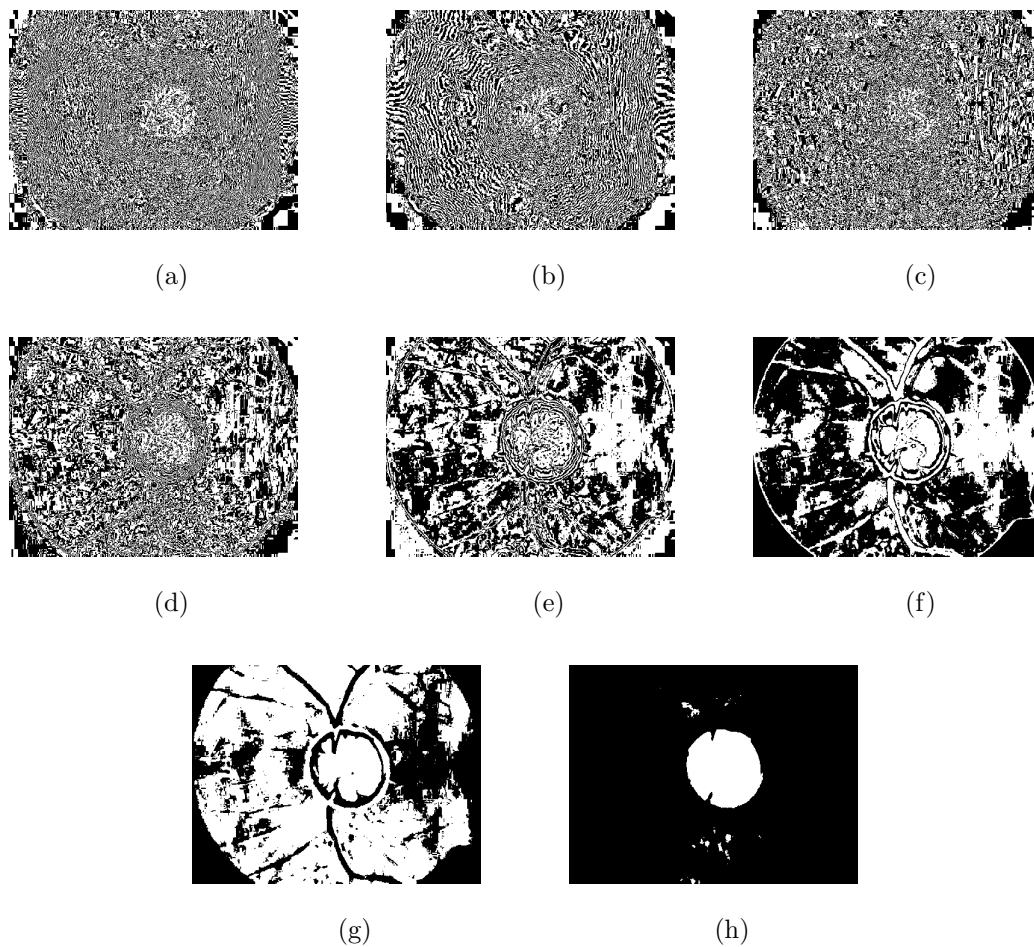


Figure 4.3: Bit planes of R channel of Fig. 4.2(e).

$$\text{LBP}_{N,L} = \sum_{n=0}^{N-1} x_n * 2^n \quad (4.1)$$

where x_n is the binary value of the neighbouring pixels. N and L in Eq. 4.1 is the number of local neighbours and the size of the square window, respectively. In the experiments, the value of N and L is set to 8 and 3, respectively. In this work, LBPs are extracted from each of the bit planes. Hence, this process generates a 2D LBP array or an LBP image from each of the bit planes. Fig. 4.4 shows the LBP images of the corresponding bit planes in Fig. 4.3.

LBP is an efficient descriptor that characterises local variation in grey levels, which is useful for texture-based classification problems. The LBP images computed from bit planes incorporate local bit-level changes. More often, the statistical analysis of texture has been found to be effective in capturing the underlying discriminating information present in the form of randomness and variability. Specifically, non-Shannon entropies and fractal dimension are computed from the LBP image as statistical features. These features are further detailed below.

Entropy

Entropy measures the variation in texture as an information content in the image [73]. Uniform distribution of pixel values leads to zero information content in an image. The proposed approach investigates non-Shannon entropies such as Kapur entropy (KE) [75], and Renyi entropy (RE) [75] to determine the texture randomness associated with LBP image. These entropies provide a higher dynamic range that makes a better estimate of randomness. The mathematical expressions for KE and RE are given below [74]:

$$\text{KE} = \frac{1}{\mathbf{b} - \mathbf{a}} \log_2 \left(\frac{\sum_{i=0}^{I-1} p_i^{\mathbf{a}}}{\sum_{i=0}^{I-1} p_i^{\mathbf{b}}} \right) \quad (4.2)$$

$$\text{RE} = \frac{1}{\mathbf{1} - \alpha} \log_2 \left(\sum_{i=0}^{I-1} p_i^{\alpha} \right) \quad (4.3)$$

where p_i denote the probability of occurrence of i^{th} LBP value. If a LBP value occur m number of times, then p_i is computed as:

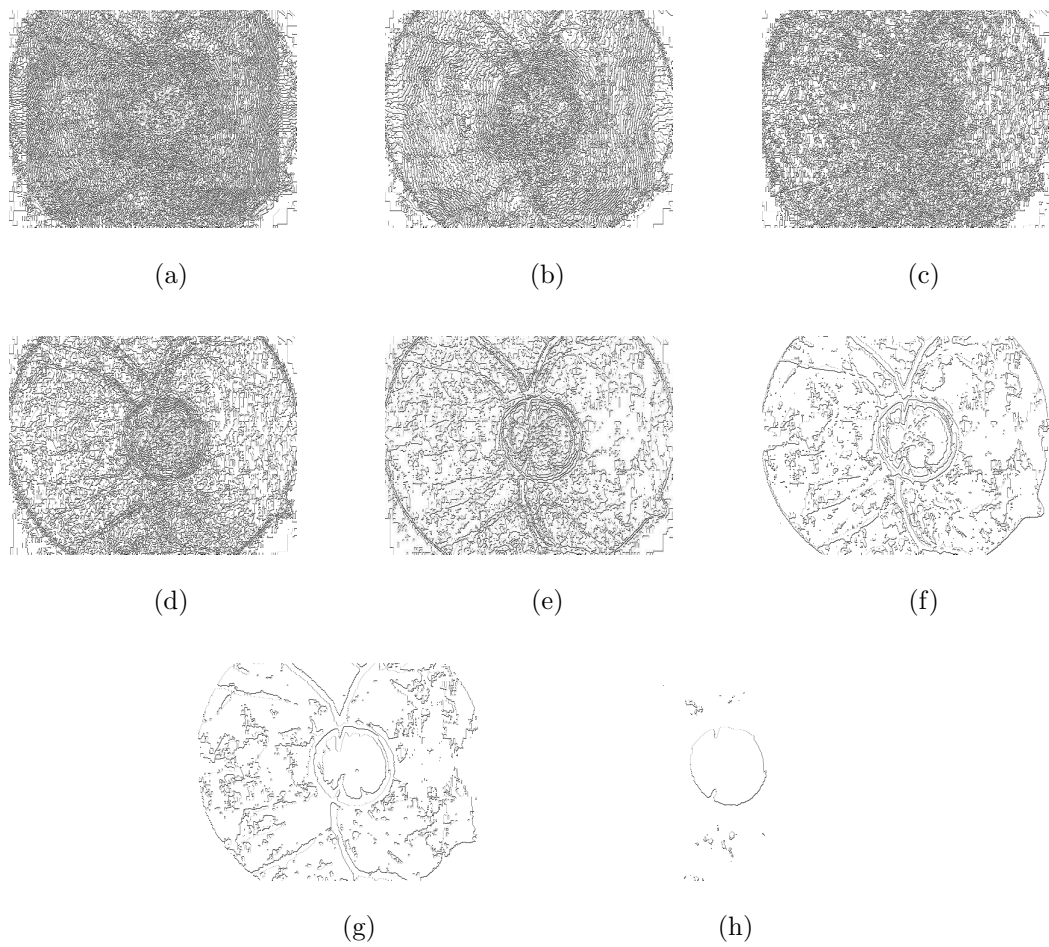


Figure 4.4: LBP images of bit planes shown in Fig. 4.3.

$$p_i = \frac{m}{r \times c} \quad (4.4)$$

where r and c denotes the number of rows and columns of LBP vector, respectively.

Fractal Dimension

A fractal is the smallest unit which repeats itself into self-similar patterns that manifest at every scale [79]. They are used to analyze random phenomena. FD is a measure of roughness and self-similarity. Of late, fractal dimension (FD) has been found to be effective in the diagnosis of ovarian tumour [78], and epileptic seizures [79]. In this work, the sequential box-counting (SBC) [76] method is employed for computing FD.

4.2.5 Feature normalization

The performance of machine learning algorithms may get affected by the skewed data, which can result in a false alarm. This issue can be rectified by employing data normalisation, which brings the skewed data to a desired numeric scale. In the proposed approach, z-score normalisation [51] is employed to transform the data into zero mean and unit standard deviation.

4.2.6 Feature Selection

Feature selection helps in improving the performance of the computer-aided diagnosis systems. Some of the extracted features do not contribute significantly to the performance due to their low discriminating ability. In this work, the Student's t -test [49, 50] is investigated for feature selection. Student's t -test generates t value for each of the features. The t value represents the discriminating capability of the corresponding feature. A high t value indicates higher discriminating capability. Therefore, these features are arranged in descending order of their corresponding t values. Tables 4.1, 4.2 and 4.3 show the first twenty features and their corresponding t values for R, G, and B channels, respectively. In *features* column, subscript denotes the bit plane number.

Table 4.1: Features extracted with t values for R channel.

Features	Normal ($mn \pm std$)	Glaucoma ($mn \pm std$)	t value
RE ₄	0.04 ± 0.008	0.02 ± 0.008	49.60
KE ₄	0.52 ± 0.033	0.40 ± 0.058	48.45
RE ₃	0.06 ± 0.005	0.03 ± 0.011	47.92
KE ₅	0.41 ± 0.043	0.28 ± 0.065	43.67
RE ₂	0.05 ± 0.006	0.03 ± 0.010	43.06
KE ₃	0.57 ± 0.016	0.48 ± 0.059	42.16
RE ₅	0.02 ± 0.006	0.008 ± 0.005	40.35
KE ₆	0.29 ± 0.046	0.18 ± 0.054	40.09
KE ₂	0.55 ± 0.023	0.55 ± 0.062	40.01
FD ₅	3.87 ± 0.010	3.84 ± 0.023	37.93
FD ₄	3.89 ± 0.005	3.87 ± 0.016	36.57
FD ₆	3.83 ± 0.019	3.77 ± 0.037	35.69
KE ₇	0.19 ± 0.042	0.12 ± 0.044	35.24
RE ₁	0.06 ± 0.004	0.04 ± 0.011	34.11
KE ₈	0.15 ± 0.030	0.09 ± 0.033	34.01
RE ₆	0.008 ± 0.003	0.003 ± 0.002	33.10
FD ₇	3.75 ± 0.03	3.68 ± 0.052	32.33
KE ₁	0.58 ± 0.013	0.52 ± 0.046	31.44
FD ₃	3.90 ± 0.003	3.88 ± 0.014	29.56
RE ₈	0.0017 ± 0.0008	0.0006 ± 0.0005	28.69

mn : mean & std : standard deviation

Table 4.2: Features extracted with t values for G channel.

Features	Normal ($mn \pm std$)	Glaucoma ($mn \pm std$)	t value
RE ₃	0.05 \pm 0.006	0.03 \pm 0.011	50.89
KE ₄	0.52 \pm 0.038	0.40 \pm 0.056	49.62
RE ₄	0.04 \pm 0.008	0.02 \pm 0.007	49.30
RE ₁	0.05 \pm 0.007	0.03 \pm 0.009	47.14
KE ₅	0.42 \pm 0.043	0.29 \pm 0.064	46.56
KE ₆	0.30 \pm 0.041	0.18 \pm 0.058	45.73
KE ₃	0.57 \pm 0.019	0.47 \pm 0.058	45.21
KE ₁	0.56 \pm 0.024	0.46 \pm 0.053	43.89
RE ₅	0.02 \pm 0.006	0.008 \pm 0.005	43.36
KE ₂	0.50 \pm 0.038	0.39 \pm 0.057	42.73
RE ₂	0.04 \pm 0.008	0.02 \pm 0.007	41.89
RE ₆	0.01 \pm 0.003	0.003 \pm 0.002	40.39
FD ₄	3.89 \pm 0.006	3.87 \pm 0.018	38.43
FD ₅	3.87 \pm 0.013	3.83 \pm 0.029	35.98
FD ₆	3.82 \pm 0.024	3.75 \pm 0.048	35.92
FD ₂	3.89 \pm 0.006	3.87 \pm 0.014	34.07
KE ₈	0.16 \pm 0.050	0.07 \pm 0.048	32.88
FD ₃	3.90 \pm 0.003	3.88 \pm 0.017	32.18
FD ₁	3.90 \pm 0.003	3.88 \pm 0.009	30.96
FD ₈	3.55 \pm 0.116	3.34 \pm 0.127	30.83

mn: mean & *std*: standard deviation

Table 4.3: Features extracted with t values for B channel.

Features	Normal ($mn \pm std$)	Glaucoma ($mn \pm std$)	t value
RE ₃	0.06 ± 0.006	0.03 ± 0.011	55.14
RE ₁	0.05 ± 0.007	0.03 ± 0.010	54.65
KE ₁	0.56 ± 0.027	0.45 ± 0.053	50.88
RE ₄	0.04 ± 0.009	0.02 ± 0.008	50.26
KE ₄	0.53 ± 0.037	0.40 ± 0.056	50.10
KE ₃	0.57 ± 0.019	0.46 ± 0.061	48.23
KE ₂	0.48 ± 0.042	0.36 ± 0.059	45.54
KE ₅	0.42 ± 0.046	0.29 ± 0.061	45.20
RE ₂	0.03 ± 0.008	0.015 ± 0.006	43.64
RE ₅	0.02 ± 0.006	0.008 ± 0.005	41.02
FD ₄	3.89 ± 0.005	3.86 ± 0.021	40.10
KE ₆	0.30 ± 0.061	0.17 ± 0.063	39.38
FD ₂	3.88 ± 0.007	3.86 ± 0.017	38.96
FD ₁	3.90 ± 0.003	3.88 ± 0.013	36.93
FD ₅	3.87 ± 0.012	3.82 ± 0.034	35.73
FD ₃	3.90 ± 0.003	3.87 ± 0.021	33.98
RE ₆	0.01 ± 0.004	0.002 ± 0.002	32.24
KE ₇	0.20 ± 0.043	0.13 ± 0.051	29.09
FD ₇	3.76 ± 0.061	3.58 ± .0167	28.98
KE ₈	0.10 ± 0.048	0.04 ± 0.035	25.33

mn : mean & std : standard deviation

4.2.7 Classification

In this work, the support vector machine (SVM) classifier is employed to discriminate the two classes. SVM classifier [86] is a supervised machine learning algorithm which is widely used for classification. Supervised machine learning algorithm needs labelled data in the training stage for mapping input-output pairs. In this work, SVM classifier with polynomial kernel function of order 2^{nd} and 3^{rd} have been investigated. In the proposed approach, the ranked features obtained from each of R, G, and B channels are fed to three SVM classifiers separately for automated classification.

4.2.8 Decision level fusion

In order to effectively combine the information obtained from the three different SVM classifiers, the decision level fusion scheme is explored in the proposed approach. Decision level fusion combines the decisions made by multiple classifiers. In the proposed methodology, each of the three SVM classifiers generates a binary decision to predict the normal or glaucoma class. In this fusion scheme, a query image belonging to a normal or glaucoma class depends upon the maximum number of predictions made by the classifiers in favour of that particular class.

4.3 Dataset and experimental results

This section details the fundus image dataset employed in the proposed approach followed by the experimental results and the discussion.

4.3.1 Database

The database used for performance evaluation of the proposed approach consists of 1426 retinal colour fundus images, out of which 589 belong to the normal class, and the rest belong to the glaucoma class. Images in this database have been collected by Kasturba Medical College, Manipal, India. The ethical approval has been obtained from the doctors in Ophthalmology department for using the database in this work. Sample fundus images are shown in Fig. 4.2.

4.3.2 Results & discussion

In this approach, 8 LBP images are obtained from 8 bit planes corresponding to each of the channels. Further, three features are extracted per LBP image. Therefore, the length of the feature vector is 24 for each channel. For validating the performance of the proposed approach, 10-fold cross-validation [65] has been explored. The commonly used measures such as accuracy, sensitivity, and specificity [64] have been used as the performance metric. Classification performance of our approach investigate for different kernel parameters, and decision level fusion method for each channel are reported in Table 4.4.

Table 4.4: Classification performance for different channels, and order of polynomial kernel function.

Decision based on	Kernel parameter (polynomial order)	Accuracy (%)	Sensitivity (%)	Specificity (%)
R channel	2 nd	98.36	96.78	99.52
R channel	3 rd	98.60	97.97	99.05
G channel	2 nd	98.95	98.83	99.05
G channel	3 rd	98.98	98.20	99.52
B channel	2 nd	98.81	98.99	98.70
B channel	3 rd	98.74	98.33	99.05
Decision level fusion	2 nd	99.16	98.99	99.29
Decision level fusion	3rd	99.30	98.84	99.64

It can be observed from Table 4.4 that the minimum classification accuracy of 98.36% is obtained by the R channel. On the other hand, the G channel individually achieves a maximum classification accuracy of 98.98%. In addition, this table also shows the performance obtained using the decision level fusion scheme. The proposed approach achieves a maximum classification accuracy of 99.30% for decision level fusion with 3rd order polynomial SVM kernel. The plots of classification performance versus the number of features with 2nd order and 3rd order polynomial kernel function are shown in Fig. 4.5 and Fig. 4.6, respectively. It can be observed from the Tables 4.1, 4.2, and 4.3 that due to high t value of the extracted features, the proposed obtains high classification accuracy.

Table 4.5 compares the proposed approach with other existing approaches for glaucoma diagnosis. The proposed approach obtains highest classification performance with a comparatively large number of fundus image in a dataset. Generally,

LBP is an efficient grey-level texture operator. However, in the proposed approach, it is explored to capture local bit-level changes in bit planes. The statistical features extracted from LBP images have been found to be highly discriminatory, and favourable for the classification process. Specifically, these entropies have been previously found to be effective for human seizure detection [87], identification of focal Electroencephalogram (EEG) signals [88], and characterization of fatty liver disease [89]. The advantage of these entropies lies in their generality and flexibility due to the parameters involved, which enable several measurements of uncertainty. Fractal dimension is an indicator of the surface roughness and has previously been employed for thyroid lesion classification in ultrasound images [90]. The proven effectiveness of these features motivated us to explore them for fundus image based glaucoma diagnosis.

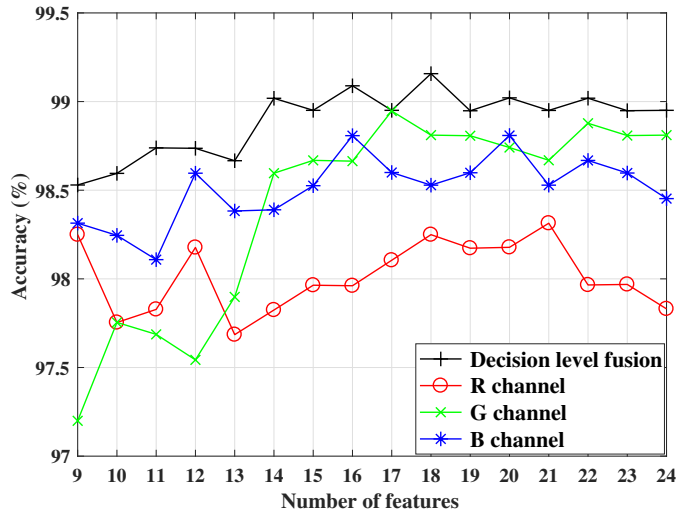
It can be noted from Table 4.1, 4.2 and 4.3 that the mean value of features for normal cases are higher as compared to glaucoma cases. This is because the normal image has more variations in terms of pixel intensities. In glaucoma case, the pixel intensity variations are less due to loss in retinal nerve fibres [80]. Also, the variability in entropy values of the normal class is more as compared to glaucoma as it has large optic disc (white region).

The local bit-level texture analysis has been found to be effective for glaucoma diagnosis. The experimental results suggest that the features extracted from the green channel achieve better classification performance as compared to other channels. This advocate that the pixel variations in the green channel are more prone to characterise glaucoma changes.

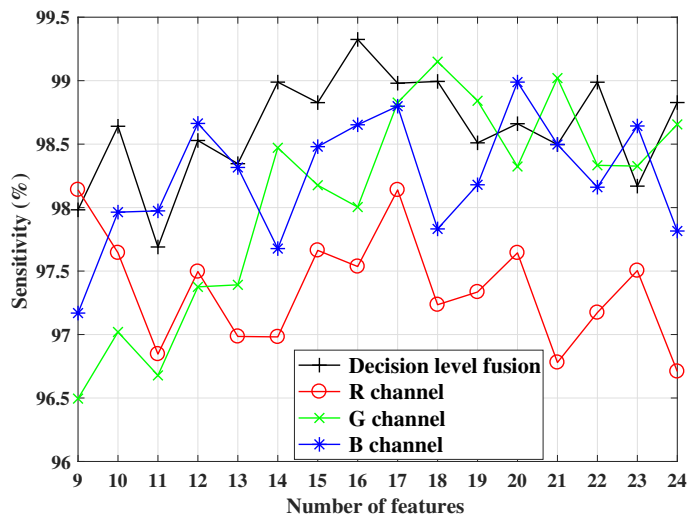
4.4 Summary

This chapter presents a local bit-level texture descriptor for the diagnosis of glaucoma. The proposed approach employs bit-plane slicing followed by local binary patterns. Further, various features have been extracted from LBP images of different channels. Furthermore, the extracted features are ranked and fed to the classifier. The SVM classifier with 2^{nd} and 3^{rd} order polynomial kernel has been investigated for performance execution of the approach. At last, The decision level

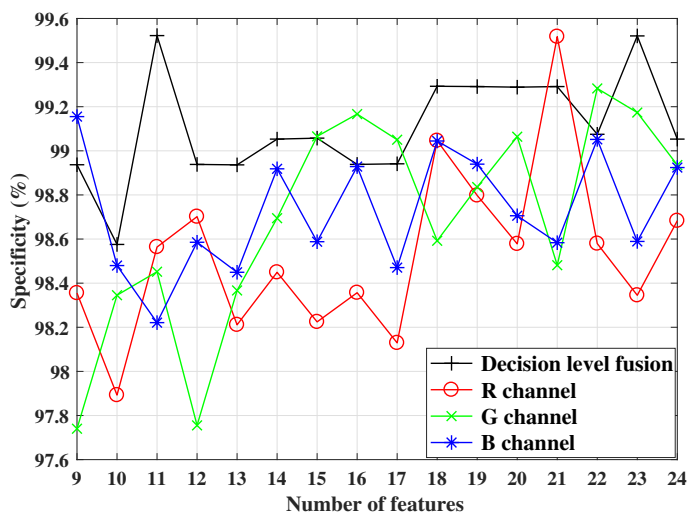
fusion technique combines the classifier predictions obtained for the features extracted from different channels. The experimental results suggest that the decision level fusion improves the classification performance of the proposed approach. The proposed approach experimentally achieves better classification performance than the existing state-of-the-art glaucoma diagnosis methodologies. Therefore, it can be concluded that the proposed approach has been experimentally found to be effective for glaucoma diagnosis.



(a)

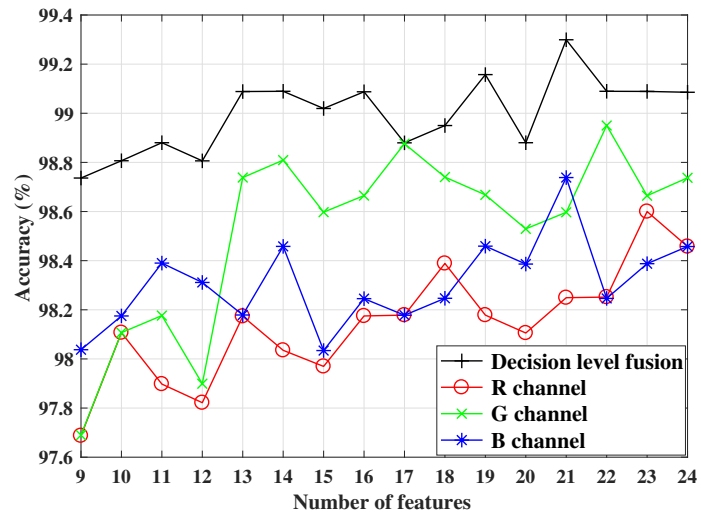


(b)

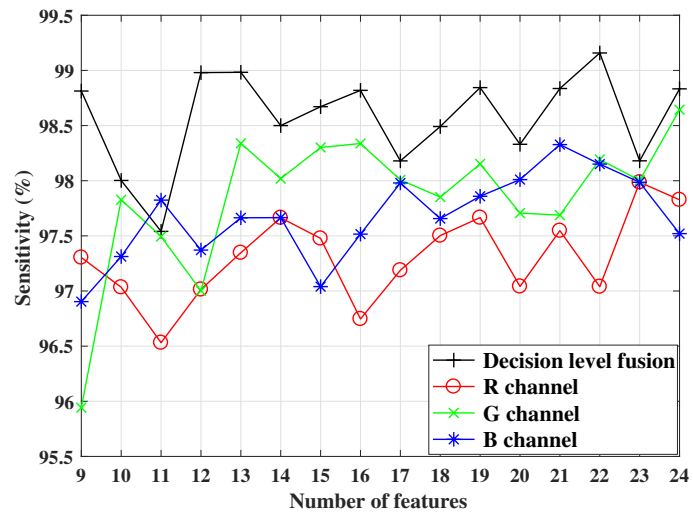


(c)

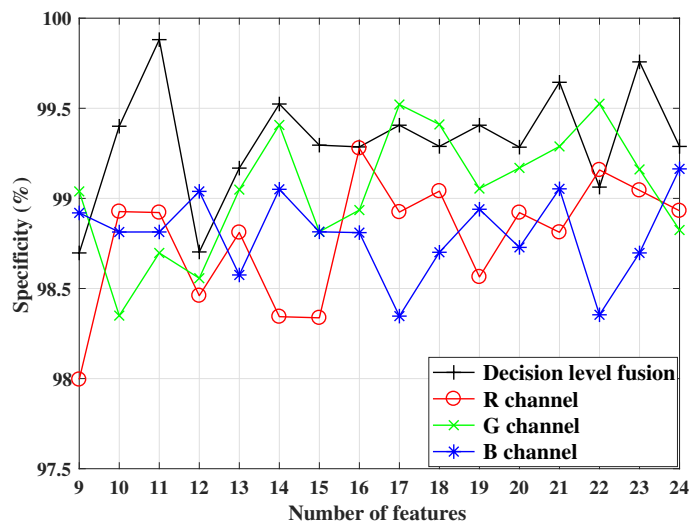
Figure 4.5: Plot of classification performance versus number of features for 2^{nd} order polynomial kernel.



(a)



(b)



(c)

Figure 4.6: Plot of classification performance versus number of features for 3rd order polynomial kernel.

Table 4.5: A comparative summary of the existing methods for automated glaucoma diagnosis.

Authors	Method	Number of images	Classifier	Performance parameters (%)
Nayak et al. [17]	Fundus disk parameters	61	ANN	ac: 90.00 sn: 100 sp: 80.00
Huang et al. [14]	Retinal nerve fiber layer thickness	165	ANN	AROC: 0.932 sn: 83.54 sp: 93.02
Bock et al. [22]	Principal component analysis (PCA), fast Fourier transform (FFT) & spline interpolation	575	SVM	ac: 80.00 sn: 73.00 sp: 85.00
Acharya et al. [23]	Higher order spectra (HOS) & texture features	60	RF	ac: 91.00 sn: NR sp: NR
Dua et al. [24]	Discrete wavelet transform (DWT) & texture features	60	SMO	ac: 93.00 sn: NR sp: NR
Mookiah et al. [25]	HOS & wavelet energy feature	60	SVM	ac: 95.00 sn: 93.33 sp: 96.67
Noronha et al. [26]	HOS cumulant features	272	Naïve Bayesian	ac: 92.60 sn: 100 sp: 92.00
Acharya et al. [27]	Gabor transformation & texture and entropy features	510	SVM	ac: 93.10 sn: 89.75 sp: 96.20

Papers	Method	Number of images	Classifier	Performance parameters (%)
Maheshwari et al. [80]	Empirical wavelet transform (EWT) & correntropy	60	LS-SVM	ac: 98.33 sn: 100 sp: 96.67
Maheshwari et al. [91]	Variational mode decomposition (VMD), entropy & fractal dimension	488	LS-SVM	ac: 95.19 sn: 93.62 sp: 96.71
Acharya et al. [1]	Local configuration pattern (LCP) & texton	702	KNN	ac: 95.70 sn: 96.20 sp: 93.70
Raghavendra et al. [92]	Non parametric spatial envelop energy spectrum	1000	SVM	ac: 97.00 sn: 97.80 sp: 95.80
Raghavendra et al. [4]	Deep CNN	1426	CNN	ac: 98.13 sn: 98.00 sp: 98.30
Proposed method	BPS & LBP	1426	SVM	ac: 99.30 sn: 98.84 sp: 99.64

*NR = Not reported, ac = accuracy, sn = sensitivity, sp = specificity, AROC = Area under receiver operating characteristics

CNN-based Approach for Glaucoma Diagnosis

This chapter presents an approach which integrates automatic feature extraction and the classification process. Specifically, in this chapter, a convolutional neural network (CNN) based approach is proposed for automated glaucoma diagnosis. Further, the proposed approach employs the local binary pattern (LBP) based data augmentation and transfer learning.

5.1 Introduction

In previous chapters, the approaches proposed for computer-aided diagnosis of glaucoma using fundus images typically involves the extraction of discriminating features from fundus images, and the classification of the extracted features. More specifically, the fundus images are initially pre-processed and followed by image analysis techniques. These techniques convert the image into simpler yet meaningful discriminatory representations referred to as features. The most discriminatory subset of features is then obtained from the feature set. Finally, the ranked features are then fed to the classifiers for discriminating between normal and glaucoma class.

However, an efficient selection of the feature extraction method and the classifier is necessary to develop an effective computer-aided diagnosis system [4]. The optimal selection of this combination is cumbersome. Further, the design of such hand-crafted features for effective diagnosis is strongly related to the expert knowledge

and have restricted representation power [4]. Also, there may arise a possibility that the computer-aided method developed for a small dataset may not work for a large dataset, and thus it may not show the discriminative ability [4].

Therefore, there is a need for a technique which can extract meaningful features automatically from the data and classifies them. Recently, CNN has gained popularity among various computer-aided diagnosis system [4], [29], [31], [30]. It integrates both, automatic feature extraction and the classification process. In this chapter, a CNN based approach is proposed for automated diagnosis of glaucoma using fundus images.

The remaining chapter is structured as follows: Section 5.2 presents the CNN architecture followed by the brief description on transfer learning and the data augmentation techniques. Section 5.3 presents the dataset description and discusses experimental results. Finally, Section 5.4 summarises the chapter.

5.2 Proposed approach

Firstly, this section presents the overview of the proposed approach, which is followed by the description of CNN architecture. Next, the transfer learning technique is presented, and the data augmentation process is described at last.

5.2.1 Overview of the proposed approach

The block diagram of the proposed approach is shown in Fig. 5.1. In this chapter, a CNN-based approach is proposed for glaucoma diagnosis. Specifically, transfer learning technique is explored in this approach. This technique employs a pre-trained CNN model, which is developed for other similar tasks. In this study, Alexnet has been investigated as a pre-trained CNN model. Further, the fundus image dataset is split into training and testing set. The colour fundus images of training and testing set are separated into red (R), green (G) and blue (B) channels. To increase the size of the training set, data augmentation is employed. Specifically, LBP-based data augmentation is employed, as shown in data augmentation block in Fig. 5.1. The augmented data is then further employed to train the CNN model. During the testing stage, the R, G, and B channels of test image are fed to the trained model,

which provide three decisions, as shown in Fig. 5.1. Finally, these decisions are then combined using the decision level fusion technique.

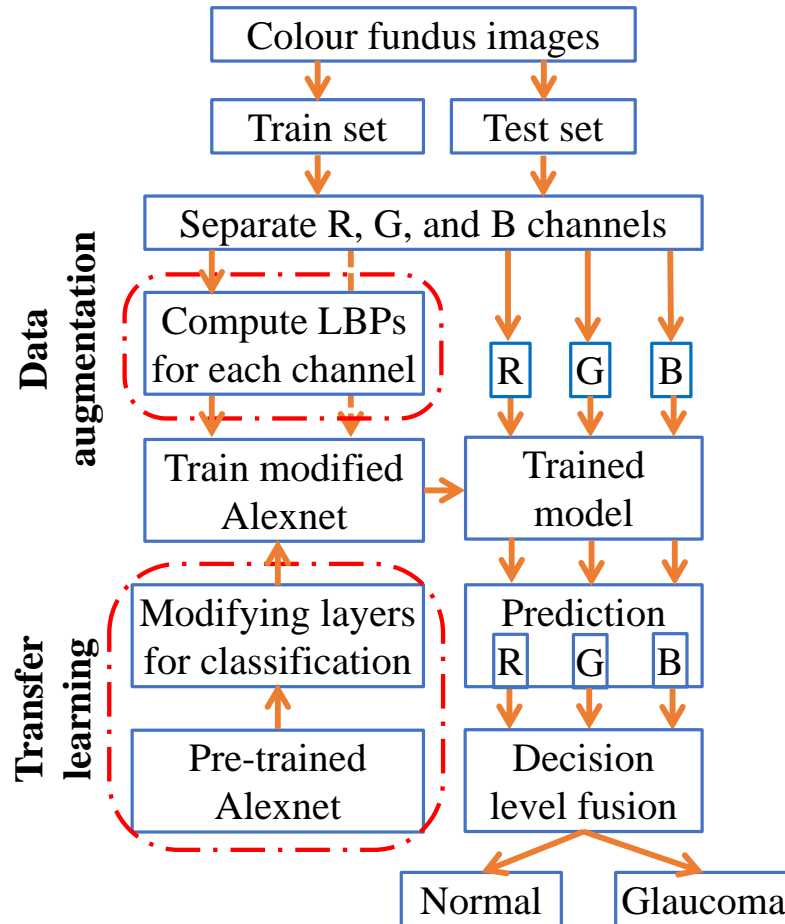


Figure 5.1: Overview of the CNN-based proposed approach.

5.2.2 Convolutional neural network

CNN is the advanced neural network architecture, which is explored in many computer vision applications such as face recognition [28], segmentation [32], and classification based approaches [29], [30]. Generally, the traditional methods for glaucoma diagnosis involve a two-step process: feature extraction followed by the classification process. Whereas, CNN is a single-step process which integrates both, the automatic feature extraction, and the classification.

The neural network is inspired by the human brain and is used in machine learning. It is composed of the input layer, the hidden layer/layer's, and the output layer. The hidden layer is a set of neurons which are connected with the neurons

in the previous layer. The neurons learn by adjusting their weights. When an unexpected output is obtained for a given set of input, the weights are adjusted by the back-propagation algorithm to achieve the desired output. Initially, the neural networks are designed for 1D data. For 2D data such as images, the design of a neural network involves large a number of parameters, which makes the network complex. This results in slow training and induces the chances of over-fitting. This limitation is overcome with the evolution of CNN.

CNN, on the other hand, is a multi-layered neural network which is developed for the image analysis and classification task. CNN employs neurons which are arranged in a 3D pattern having width, height, and number of filter layers. The CNN architecture is composed of one or multiple repetitions of the following layers:

1. Input layer: This is the first layer of CNN. It holds and passes the raw data to next layer for further processing.
2. Convolutional layer: This layer performs a dot product between the filter and local image region. It is referred to as the learning layer. It preserves the information in the local neighbourhood.
3. Rectified linear unit (ReLU): This is an activation function used to thresholding the output of previous layer. It is written as $\max(0, x)$. This function returns 0 if x is less than 0, and x otherwise.
4. Max-pooling layer: It reduces the spatial dimension of the data received from the previous layer.
5. Fully connected layer: In this layer, the neurons are fully connected with the neurons of the previous layer.
6. Soft-max layer: This layer brings the data in the range 0 - 1. It is a normalized exponential function.
7. Output layer: This layer provides the output prediction. It contains the loss function and label of the input data.

5.2.3 Transfer learning

Training an entire CNN model from scratch requires a very large dataset and a capable GPU based hardware. Practically, it is not feasible to train a complete CNN network from scratch due to hardware limitation and the small size of the dataset. To overcome this limitation, transfer learning technique is explored in this work. Transfer learning employs a pre-trained CNN model, which is developed for other similar tasks. This pre-trained model is then trained on new data by changing certain design parameters [93].

Training a pre-trained CNN model on a new dataset is about adjusting the layer weights. Specifically, in the proposed approach, Alexnet [94] is investigated as a pre-trained CNN model, and is re-trained via transfer learning. The network architecture of Alexnet contains eight learning layers, out of which five are convolution layers, and three are fully-connected layers. Originally, Alexnet is capable of classifying 1000 classes. However, in the proposed approach, Alexnet is modified to perform binary classification. For this purpose, the last three layers, namely the fully-connected layer, the soft-max layer, and the classification layer, are modified to train them from scratch. However, the remaining layers need to adjust their corresponding weights according to new training data. Table 5.1 lists the layers of the modified Alexnet. Fig. 5.2 shows the modified Alexnet architecture used in this work.

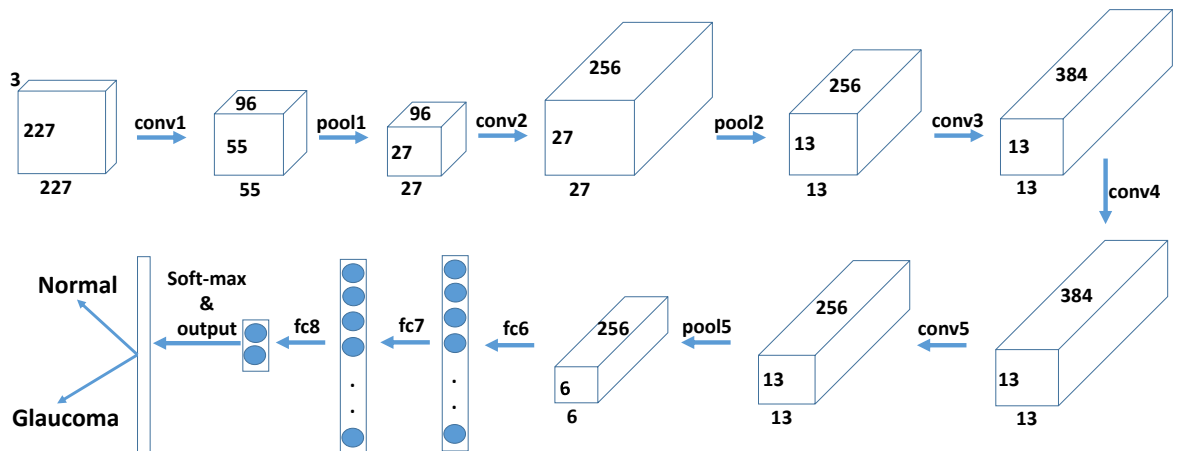


Figure 5.2: Modified Alexnet architecture via transfer learning.

Table 5.1: Architecture of modified Alexnet CNN model.

Layers	Layer label	Layer parameters
Image Input	data	Sz: 227x227x3
Convolution	conv1	Nf: 96, Sz: 11x11x3, St: 4, Pd=0
ReLU	relu1	-
Cross Channel Normalization	norm	-
Max Pooling	pool1	Sz: 3x3, St:2
Convolution	conv2	Ft: 256, Sz: 5x5x48, St:1, Pd:2
ReLU	relu2	-
Cross Channel Normalization	norm2	-
Max Pooling	pool2	Sz: 3x3, St:2
Convolution	conv3	Nf: 384. Sz: 3x3x256, St: 1, pd:1
ReLU	relu3	-
Convolution	conv4	Fn: 384, Sz: 3x3x192, St:1 Pd:1
ReLU	relu4	-
Convolution	conv5	Fn: 256, Sz: 3x3x192, St:1, Pd: 1
ReLU	relu5	-
Max Pooling	pool5	Sz = 3x3, St:2, Pd:0
Fully Connected	fc6	Sz = 4096
ReLU	relu6	-
Dropout	drop6	50%
Fully Connected	fc7	Sz: 4096
ReLU	relu7	-
Dropout	drop7	50%
Fully Connected	fc8	Sz: 2
Softmax	prob	-
Classification Output	output	cross-entropy

5.2.4 Data augmentation

In order to prevent the CNN model from over-fitting, a large number of labelled data is required to train the CNN model [94]. As the size of the training data available for this task is small, data augmentation method is employed to increase the size of training data. Data augmentation employ operations such as cropping, scaling, translation, shear, zooming, rotation, and reflection. However, in the proposed approach, any of the above-described operations are not employed for data augmentation. Instead, the LBPs [85] of R, G, and B channels of the training data

are computed. The LBP-based data augmentation block is shown in Fig. 5.1. The computed LBPs of each channel is a 2D vector, so it is referred to as LBP images in the rest of the chapter.

5.3 Dataset & experimental results

In this section, the fundus image dataset employed in the proposed approach and the experimental results are presented.

5.3.1 Dataset

The publicly available RIM-ONE database is employed to validate the proposed approach. The dataset contains 455 colour fundus images with 255 normal and 200 glaucoma images. This database is obtained from medical image analysis group (MIAG) and is available at <http://medimrg.webs.ull.es/>. The fundus images in the dataset are stored in JPEG format with different resolutions.

5.3.2 Results & discussion

The fundus image database is divided into training (80%) and testing (20%) data. The experiments have also been validated with 70:30 and 90:10 data split into training:testing. In order to train the model, values of the parameters involved are initialized as follows: learning rate is set to 0.0001, stochastic gradient descent with momentum (SGDM) optimizer is used as a solver, the number of images in a batch is 20, and the number of epochs is 80.

Initially, the images in the training and testing data are separated into R, G, and B channels. Then, LBP-based data augmentation is employed by obtaining LBP images of individual channels of training data. Further, the augmented data is fed to the modified CNN model for training. While testing, the trained Alexnet model generates predictions for R, G, and B channels of the test image. These three individual predictions are further combined using decision level fusion technique [95]. In order to access the performance of the proposed approach, the commonly used parameters are employed, such as accuracy, sensitivity and specificity [64].

The experiments are repeated 20 times, therefore, the classification performances are tabulated in the form of *maximum – mean – minimum* value in Table 5.2.

Table 5.2 tabulates classification performances for 70:30, 80:20 and 90:10 training:testing data split. It can be observed from the Table 5.2 that the R channel individually achieves a maximum classification accuracy of 99.10%, 98.90% and 95.58% for 70:30, 80:20 and 90:10 training:testing data split, respectively. The B channel obtains minimum performance. The experiments have also been performed without employing LBP based data augmentation for 80:20 training:testing data split. The classification performance without LBP based data augmentation is tabulated in Table 5.3. It can be observed from Table 5.3 that the experiments performed with LBP-based data augmentation achieve better classification performance as compared to the experiments performed without employing data augmentation.

Table 5.2: Classification performance for LBP-based data augmentation.

Data split (training:testing)	Performance of	Accuracy (%) (max-mean-min)	Sensitivity (%) (max-mean-min)	Specificity (%) (max-mean-min)
90 : 10	R channel	98.90 - 94.28 - 92.30	100 - 97.25 - 90.19	97.50 - 90.50 - 82.50
	G channel	94.50 - 91.37 - 90.11	100 - 96.27 - 90.19	97.50 - 86.00 - 75.00
	B channel	93.40 - 91.42 - 90.11	98.03 - 94.80 - 92.15	92.50 - 87.12 - 82.50
	Decision level fusion	96.70 - 93.40 - 92.30	100 - 96.69 - 92.15	97.50 - 88.75 - 85.00
80 : 20	R channel	95.58 - 92.86 - 91.91	100 - 95.68 - 90.79	95.00 - 89.33 - 86.67
	G channel	92.65 - 90.69 - 88.97	100 - 94.80 - 89.47	95.00 - 85.67 - 75.00
	B channel	92.65 - 89.55 - 88.33	98.68 - 93.22 - 86.84	90.0 - 84.33 - 76.67
	Decision level fusion	94.11 - 92.24 - 91.17	100 - 95.26 - 88.15	96.67 - 88.41 - 81.67
70 : 30	R channel	99.10 - 96.00 - 93.33	100 - 97.20 - 92.00	100 - 94.50 - 90.00
	G channel	98.95 - 95.00 - 93.33	100 - 98.60 - 92.00	100 - 89.00 - 70.00
	B channel	98.60 - 94.33 - 93.33	100 - 96.20 - 92.00	100 - 92.00 - 85.00
	Decision level fusion	100 - 96.00 - 93.33	100 - 98.00 - 92.00	100 - 93.50 - 85.00

Table 5.3: Classification performance without LBP based data augmentation for 80:20 training:testing data split.

LBP based data augmentation	Channel	Accuracy (%) (max-mean-min)
Yes	R	98.90 - 94.28 - 92.30
	G	94.50 - 91.37 - 90.11
	B	93.40 - 91.42 - 90.11
No	R	94.51 - 92.97 - 92.31
	G	93.41 - 91.10 - 90.11
	B	93.41 - 90.44 - 89.01

Table 5.4: A comparative summary of the existing methods for automated glaucoma diagnosis for public database.

Authors	Method	Classifier/ CNN architecture	Performance (%)
Acharya et al. [92]	Non parametric spatial envelop energy pattern	SVM	ac: 93.62 sn: 87.50 sp: 98.43
Bander et al. [35]	Deep CNN based feature extraction	SVM	ac: 88.20 sn: 90.8 sp: 85
Allan et al. [34]	Deep CNN	Google-net	ac: 86.20 sn: - sp: -
Maheshwari et al. [80]	Empirical wavelet transform based correntropy features	LS-SVM	ac: 81.32 sn: - sp: -
Kirar et al. [96]	Discrete & empirical wavelet transform	LS-SVM	ac: 83.57 sn: 86.40 sp: 80.80
Maheshwari et al. [91]	Variational mode decomposition based entropy and fractal features	SVM	ac: 81.62 sn: - sp: -
Proposed method	Local binary pattern & Deep CNN transfer learning	Alexnet	ac: 98.90 sn: 100 sp: 97.50

*NR = Not reported, ac = accuracy, sn = sensitivity, sp = specificity, AROC = Area under receiver operating characteristics

Table 5.4 presents a brief description of the existing methodologies developed for automated glaucoma diagnosis using public database.

The proposed CNN-based approach self-extract the meaningful features from the data by performing a series of convolutional operations. The variety of filters are convolved with the input data at different layers of the CNN model. These many convolution operations extract the features from the input fundus images. As the image travels down the CNN network, the layers break down the fundus image into low-level features, which are used for the classification between the normal and glaucoma class. The features plot of the last layers is shown in Fig. 5.3.

LBP-based data augmentation has been in this work. The LBP is simple and effective feature descriptor employed for texture-based image classification [36], [37]. Further, to demonstrate the effectiveness of LBP-based data augmentation, t-Distributed Stochastic Neighbor Embedding (t-SNE) [97] method is explored to visualise the non-LBP and LBP features learned by the CNN model. The t-SNE

is a non-linear dimensionality reduction technique which is well-suited for embedding high-dimensional data for visualisation in a low-dimensional space of two or three dimensions [97]. It preserves the local variances of the data to be visualised. In simpler terms, t-SNE provides the intuition of how the data is arranged in a high-dimensional space.

In this method, we have employed t-SNE to visualise the high-dimensional features learned by various layers of the pre-trained CNN model from retinal fundus image dataset. Fig. 5.3 shows the t-SNE visualisation of the features learned by conv5 layer (left), fc6 layer(middle), and fc7 layer (right). It can be observed from Fig. 5.3 that as the features pass through subsequent layers, the discrimination between normal and glaucoma class increases. However, the t-SNE visualisation clearly indicates that the features extracted from LBP based augmented data are more discriminatory as compared to features extracted from non-augmented data. Therefore, it can be observed from the t-SNE plot that the transfer learning of pre-trained CNN network, i.e., Alexnet and LBP based data augmentation is effective in glaucoma diagnosis using retinal fundus images. Table 5.5 describes the legends used in Fig. 5.3.

Table 5.5: Description of legends used in Fig. 5.3.

Legend	Feature corresponding to
×	Glaucoma data (glc)
o	Normal data (nrm)
Δ	Local binary pattern (LBP) of glc data (LBP glc)
*	LBP of nrm data (LBP nrm)

The experiments have also been performed without employing LBP based data augmentation to training data. The result of which is tabulated in Table 5.3. It can be observed from Fig. 5.3 that due to good inter-class discrimination capability of LBP images, the classification performance of the CNN model improves by employing LBP based data augmentation.

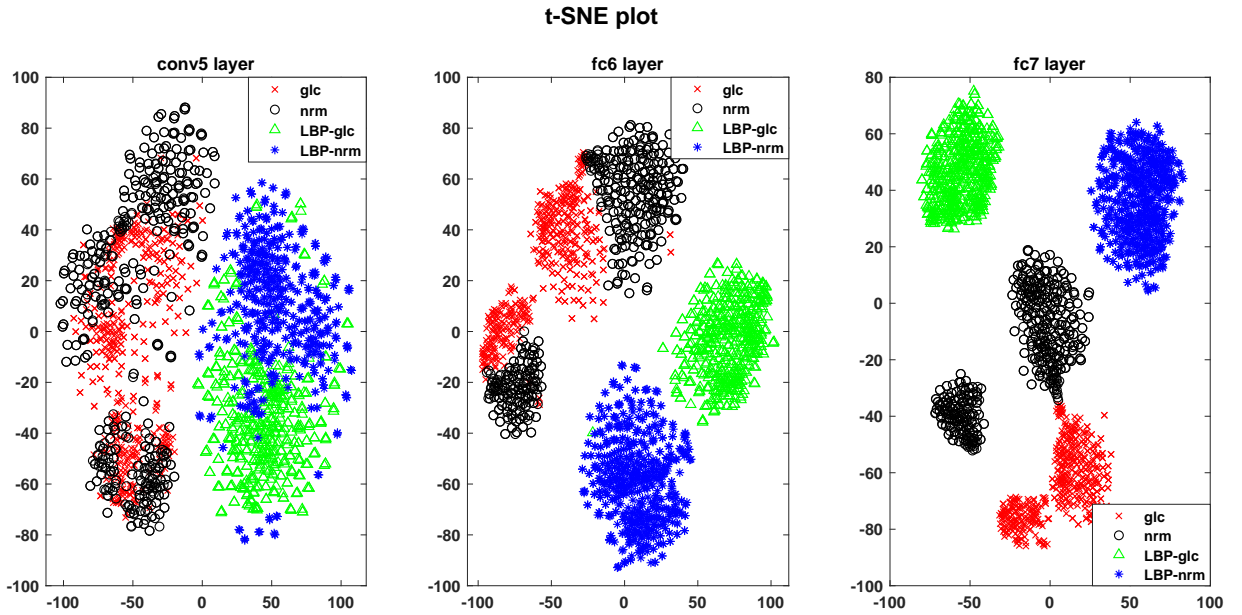


Figure 5.3: The t-SNE plot of: features learned by *conv5* layer (left), output of *fc6* (middle) and *fc7* (right) layers of the modified CNN model.

5.4 Summary

This chapter proposed a CNN based approach for automated glaucoma diagnosis. The transfer learning technique has been employed to re-train the pre-trained CNN model. Transfer learning is employed to overcome the limitation of having advance and GPU-based capable hardware. To prevent the CNN model from overfitting, LBP-based data augmentation technique is employed. The experimental results suggest that the performance of the proposed approach improves by employing LBP-based data augmentation. The approach obtains promising classification performance. Therefore, the proposed approach can help in reducing the burden on experts and assists them during mass screening.

Conclusions and Future Scope

This chapter presents concluding remarks on the main contributions of the thesis and discusses some directions for future research.

6.1 Conclusions

In Chapter 2, the adaptive non-stationary image analysis technique has been investigated for glaucoma diagnosis. Specifically, the EWT based approach has been proposed in this study. The correntropy is extracted as the feature from EWT components of R, G, B, and Gr channels of fundus image. To validate the classification performance, three-fold and ten-fold cross-validation is employed. The experiments have been validated on the dataset of 60 fundus images. The experimental results demonstrated that the features extracted from the G channel obtain maximum classification performance when compared to other channels. The experiments suggest that the correntropy features extracted from G channel incorporate the subtle pixel intensity changes that characterise glaucoma change in the fundus image. The experimental results suggest that the adaptive approach is effective for glaucoma diagnosis.

In Chapter 3, the iterative approach has been investigated on fundus images for glaucoma diagnosis. Specifically, the VMD based iterative approach has been proposed. Only the G channel of the fundus image is considered in this work. The features extracted from the G channel have been experimentally found to be effective for glaucoma diagnosis in the approach proposed in chapter 2. Various

entropies and fractal dimension features have been extracted from the decomposed VMD components obtained by the iterative process. The proposed approach is evaluated on the dataset of 488 fundus images. The iterative process repeatedly decomposes the previous VMD component and narrows the spatial frequency band of new VMD component. The features extracted from narrow-band VMD components incorporate the pixel changes due to glaucoma in fundus images. The experimental results approve the effectiveness of the iterative approach for glaucoma diagnosis.

In Chapter 4, the local bit-level texture descriptor has been developed for automated glaucoma diagnosis. In this approach, BPS is followed by LBP. The LBP images are obtained from the bit planes of R, G, and B channels. Further, the entropies and fractal dimension are extracted as the features from LBP images. In the proposed approach, the decision level fusion technique is explored to combine the individual classifier predictions of the features extracted from different channels. The proposed method is validated on the dataset of 1426 fundus images. The experimental results suggest that the features extracted from the G channel obtain better classification performance than the features of other channels. The G channel features capture the subtle pixel variations that characterise glaucoma. The experiments also support the statement made for the approach proposed in Chapter 2 that the features extracted from G channel deliver promising classification performance. Further, the decision level fusion technique combines the feature predictions of different channels and achieves highest classification performance. Unlike grey-level texture feature descriptor, the experimental results suggest that local bit-level texture descriptor has been found useful for glaucoma diagnosis.

In Chapter 5, CNN based approach is investigated for glaucoma diagnosis. Computer-aided diagnosis methods generally involve feature extraction and the classification process. The design of such hand-crafted features are time-consuming, require field expertise, and have limited representation capability. On the other hand, the CNN integrated automatic feature extraction and classification. In the proposed approach, Alexnet has been explored as a pre-trained CNN model, which is re-trained via transfer learning. However, to prevent the model from over-fitting, LBP-based data augmentation technique has been employed. The approach is evaluated on the public dataset of 455 fundus images. Further, the experiments have been repeated 20

times to validate the performance of the approach. The experimental results suggest that the LBP-based data augmentation improves the classification performance of the proposed approach. Experimentally, the proposed approach in this study has been found effective for glaucoma diagnosis.

In summary, various approaches have been investigated for glaucoma diagnosis. The advanced image analysis techniques and machine learning algorithms have been explored. The proposed approaches have been validated on various fundus image datasets. In general, the implementation of computer-aided diagnosis approaches involves image analysis and the classification process. The image analysis techniques convert the images into simpler yet meaningful representations which are further classified. Image analysis typically involves image processing and feature extraction. In the proposed approaches, the extracted features from the fundus images have been found to be useful for glaucoma diagnosis as they incorporate the characteristics changes in fundus image due to glaucoma condition.

6.2 Future scope

This section presents the future directions of this thesis. In this thesis, various advanced image analysis and machine learning algorithms based approaches are proposed for glaucoma diagnosis. In future, the research work in this thesis can be extended as follows:

The approaches proposed in this thesis needs to be tested on a huge dataset. The experimental evaluation of the proposed approaches on a large and diverse dataset will provide more reliable performance. In general, for biomedical applications, there is very less number of publicly available datasets. Moreover, these datasets consist of less number of fundus images. In future, collaboration with hospitals can be made to collect a large number of fundus images under the supervision of experts. To make the dataset more diversified, the fundus image data can be collected from people of different age groups belonging to various geographical regions.

The proposed approaches aid clinicians during mass-screening. Also, an application can be developed for a portable device. This device can be made accessible at nearest health centres in areas where experts are not available for initial glaucoma

screening. This device will help to detect glaucoma symptoms in early stages for people residing in rural areas. Also, the work-load of clinicians will be reduced as now they have to consider cases only with glaucoma symptoms.

In future, the proposed approaches can be explored for the diagnosis of other diseases such as diabetes retinopathy, fatty liver disease, thyroid cancer, and ovarian cancer. Fundus image is employed for the diagnosis of diabetic retinopathy. Similarly, the ultrasound image is employed for the diagnosis of fatty liver, ovarian and thyroid cancer. As the diagnosis of these diseases involves image analysis methods, the proposed approaches can be investigated for their diagnosis.

References

- [1] U. R. Acharya, S. Bhat, J. E. Koh, S. V. Bhandary, and H. Adeli, “A novel algorithm to detect glaucoma risk using texton and local configuration pattern features extracted from fundus images,” *Computers in Biology and Medicine*, vol. 88, pp. 72–83, 2017.
- [2] X. Chen, Y. Xu, S. Yan, D. W. K. Wong, T. Y. Wong, and J. Liu, “Automatic feature learning for glaucoma detection based on deep learning,” in *Medical Image Computing and Computer-Assisted Intervention (MICCAI)*, 2015, pp. 669–677.
- [3] A. A. Salam, T. Khalil, M. U. Akram, A. Jameel, and I. Basit, “Automated detection of glaucoma using structural and non structural features,” *SpringerPlus*, vol. 5, no. 1, p. 1519, Sep 2016.
- [4] U. Raghavendra, H. Fujita, S. V. Bhandary, A. Gudigar, J. H. Tan, and U. R. Acharya, “Deep convolution neural network for accurate diagnosis of glaucoma using digital fundus images,” *Information Sciences*, vol. 441, pp. 41–49, 2018.
- [5] M. J. Greaney, D. C. Hoffman, D. F. Garway-Heath, M. Nakla, A. L. Coleman, and J. Caprioli, “Comparison of optic nerve imaging methods to distinguish normal eyes from those with glaucoma,” *Investigative Ophthalmology and Visual Science*, vol. 43, no. 1, pp. 140–145, 2002.
- [6] T. Lim, S. Chattopadhyay, and U. R. Acharya, “A survey and comparative study on the instruments for glaucoma detection,” *Medical Engineering & Physics*, vol. 34, no. 2, pp. 129–139, 2012.
- [7] P. Sharma, P. A. Sample, L. M. Zangwill, and J. S. Schuman, “Diagnostic tools for glaucoma detection and management,” *Survey of Ophthalmology*, pp. 17–32, 2008.
- [8] Y. C. Tham, X. Li, T. Y. Wong, H. A. Quigley, T. Aung, and C. Y. Cheng, “Global prevalence of glaucoma and projections of glaucoma burden through 2040: A systematic review and meta-analysis,” *Ophthalmology*, vol. 121, no. 11, pp. 2081–2090, 2014.
- [9] H. A. Quigley and A. T. Broman, “The number of people with glaucoma worldwide in 2010 and 2020,” *British Journal of Ophthalmology*, vol. 90, no. 3, pp. 262–267, 2006.

- [10] Y. Hagiwara, J. E. W. Koh, J. H. Tan, S. V. Bhandary, A. Laude, E. J. Ciaccio, L. Tong, and U. R. Acharya, "Computer-aided diagnosis of glaucoma using fundus images: A review," *Computer Methods and Programs in Biomedicine*, vol. 165, pp. 1–12, 2018.
- [11] R. Nagarajan, C. Balachandran, D. Gunaratnam, A. Klistorner, and S. Graham, "Neural network model for early detection of glaucoma using multi-focal visual evoked potential (M-VEP)," *Investigative Ophthalmology and Visual Science*, vol. 43, no. 13, p. 3902, 2002.
- [12] E. A. Essock, Y. Zheng, and P. Gunvant, "Analysis of GDx-VCC polarimetry data by wavelet Fourier analysis across glaucoma stages," *Investigative Ophthalmology and Visual Science*, vol. 46, no. 8, pp. 2838–2847, 2005.
- [13] M. Huang, H. Chen, and J. Huang, "Glaucoma detection using adaptive neuro-fuzzy inference system," *Expert Systems with Applications*, vol. 32, no. 2, pp. 458–468, 2007.
- [14] M. Huang, H. Chen, W. Huang, and Y. Tsai, "Linear discriminant analysis and artificial neural network for glaucoma diagnosis using scanning laser polarimetry-variable cornea compensation measurements in taiwan chinese population," *Graefe's Archive for Clinical and Experimental Ophthalmology*, vol. 248, no. 3, pp. 435–441, Mar 2010.
- [15] C. Bowd, K. Chan, L. M. Zangwill, M. H. Goldbaum, T. Lee, T. J. Sejnowski, and R. N. Weinreb, "Comparing Neural Networks and Linear Discriminant Functions for Glaucoma Detection Using Confocal Scanning Laser Ophthalmoscopy of the Optic Disc," *Investigative Ophthalmology & Visual Science*, vol. 43, no. 11, pp. 3444–3454, 11 2002.
- [16] M. B. Merickel, M. D. Abramoff, M. Sonka, and X. Wu, "Segmentation of the optic nerve head combining pixel classification and graph search," in *Medical Imaging: Image Processing*, vol. 6512, 2007.
- [17] J. Nayak, U. R. Acharya, P. S. Bhat, N. Shetty, and T. C. Lim, "Automated diagnosis of glaucoma using digital fundus images," *Journal of Medical Systems*, vol. 33, no. 5, pp. 337–346, 2009.
- [18] N. V. Swindale, G. Stjepanovic, A. Chin, and F. S. Mikelberg, "Automated analysis of normal and glaucomatous optic nerve head topography images," *Investigative Ophthalmology and Visual Science*, vol. 41, no. 7, pp. 1730–1742, 2000.
- [19] G. D. Joshi, J. Sivaswamy, and S. R. Krishnadas, "Depth discontinuity-based cup segmentation from multiview color retinal images," *IEEE Transactions on Biomedical Engineering*, vol. 59, no. 6, pp. 1523–1531, 2012.
- [20] M. Balasubramanian, S. Zabic, C. Bowd, H. W. Thompson, P. Wolenski, S. S. Iyengar, B. B. Karki, and L. M. Zangwill, "A framework for detecting glaucomatous progression in the optic nerve head of an eye using proper orthogonal decomposition," *IEEE Transactions on Information Technology in Biomedicine*, vol. 13, no. 5, pp. 781–793, 2009.

- [21] R. Kolar and J. Jan, "Detection of glaucomatous eye via color fundus images using fractal dimensions," *Radio Engineering*, vol. 17, no. 3, pp. 109–114, 2008.
- [22] R. Bock, J. Meier, L. G. Nyúl, J. Hornegger, and G. Michelson, "Glaucoma risk index: Automated glaucoma detection from color fundus images," *Medical Image Analysis*, vol. 14, no. 3, pp. 471–481, 2010.
- [23] U. R. Acharya, S. Dua, X. Du, S. V. Sree, and C. K. Chua, "Automated diagnosis of glaucoma using texture and higher order spectra features," *IEEE Transactions on Information Technology in Biomedicine*, vol. 15, no. 3, pp. 449–455, 2011.
- [24] S. Dua, U. R. Acharya, P. Chowriappa, and S. V. Sree, "Wavelet based energy features for glaucomatous image classification," *IEEE Transactions on Information Technology in Biomedicine*, vol. 16, no. 1, pp. 80–87, 2012.
- [25] M. R. K. Mookiah, U. R. Acharya, C. M. Lim, A. Petznick, and J. S. Suri, "Data mining technique for automated diagnosis of glaucoma using higher order spectra and wavelet energy features," *Knowledge-Based Systems*, vol. 33, pp. 73–82, 2012.
- [26] K. P. Noronha, U. R. Acharya, K. P. Nayak, R. J. Martis, and S. V. Bhandary, "Automated classification of glaucoma stages using higher order cumulant features," *Biomedical Signal Processing and Control*, vol. 10, pp. 174–183, 2014.
- [27] U. R. Acharya, E. Ng, L. W. J. Eugene, K. P. Noronha, L. C. Min, K. P. Nayak, and S. V. Bhandary, "Decision support system for the glaucoma using Gabor transformation," *Biomedical Signal Processing and Control*, vol. 15, pp. 18–26, 2015.
- [28] S. Lawrence, C. L. Giles, Ah Chung Tsoi, and A. D. Back, "Face recognition: a convolutional neural-network approach," *IEEE Transactions on Neural Networks*, vol. 8, no. 1, pp. 98–113, Jan 1997.
- [29] M. Talo, U. B. Baloglu, O. Yildirim, and U. R. Acharya, "Application of deep transfer learning for automated brain abnormality classification using mr images," *Cognitive Systems Research*, vol. 54, pp. 176–188, 2019.
- [30] A. Das, U. R. Acharya, S. S. Panda, and S. Sabut, "Deep learning based liver cancer detection using watershed transform and gaussian mixture model techniques," *Cognitive Systems Research*, vol. 54, pp. 165–175, 2019.
- [31] U. B. Baloglu, M. Talo, O. Yildirim, R. S. Tan, and U. R. Acharya, "Classification of myocardial infarction with multi-lead ecg signals and deep cnn," *Pattern Recognition Letters*, vol. 122, pp. 23–30, 2019.
- [32] M. Kallenberg, K. Petersen, M. Nielsen, A. Y. Ng, P. Diao, C. Igel, C. M. Vachon, K. Holland, R. R. Winkel, N. Karssemeijer, and M. Lillholm, "Unsupervised deep learning applied to breast density segmentation and mammographic risk scoring," *IEEE Transactions on Medical Imaging*, vol. 35, no. 5, pp. 1322–1331, 2016.

- [33] X. Chen, Y. Xu, D. W. Kee Wong, T. Y. Wong, and J. Liu, "Glaucoma detection based on deep convolutional neural network," in *37th Annual International Conference of the IEEE Engineering in Medicine and Biology Society (EMBC)*, 2015, pp. 715–718.
- [34] A. Cerentini, D. Welfer, M. C. d'Ornellas, C. J. P. Haygert, and G. N. Dotto, "Automatic identification of glaucoma using deep learning methods," in *MED-INFO 2017: Precision Healthcare through Informatics*, 2017, vol. 245, pp. 318–321.
- [35] B. Al-Bander, W. Al-Nuaimy, M. A. Al-Tae, and Y. Zheng, "Automated glaucoma diagnosis using deep learning approach," in *14th International Multi-Conference on Systems, Signals Devices (SSD)*, 2017, pp. 207–210.
- [36] Z. Guo, L. Zhang, and D. Zhang, "A completed modeling of local binary pattern operator for texture classification," *IEEE Transactions on Image Processing*, vol. 19, no. 6, pp. 1657–1663, June 2010.
- [37] S. Liao, M. W. K. Law, and A. C. S. Chung, "Dominant local binary patterns for texture classification," *IEEE Transactions on Image Processing*, vol. 18, no. 5, pp. 1107–1118, May 2009.
- [38] T. Ahonen, A. Hadid, and M. Pietikainen, "Face description with local binary patterns: Application to face recognition," *IEEE Transactions on Pattern Analysis and Machine Intelligence*, vol. 28, no. 12, pp. 2037–2041, Dec 2006.
- [39] L. Fei, B. Zhang, Y. Xu, D. Huang, W. Jia, and J. Wen, "Local discriminant direction binary pattern for palmprint representation and recognition," *IEEE Transactions on Circuits and Systems for Video Technology*, 2019.
- [40] R. Yan and R. X. Gao, "Hilbert-Huang Transform-Based Vibration Signal Analysis for Machine Health Monitoring," *IEEE Transactions on Instrumentation and Measurement*, vol. 55, no. 6, pp. 2320–2329, 2006.
- [41] Z. Luo, T. Liu, S. Yan, and M. Qian, "Revised empirical wavelet transform based on auto-regressive power spectrum and its application to the mode decomposition of deployable structure," *Journal of Sound Vibration*, vol. 431, pp. 70–87, 2018.
- [42] N. E. Huang, Z. Shen, S. R. Long, M. C. Wu, H. H. Shih, Q. Zheng, N.-C. Yen, C. C. Tung, and H. H. Liu, "The empirical mode decomposition and the hilbert spectrum for nonlinear and non-stationary time series analysis," *Proceedings of the Royal Society of London A: Mathematical, Physical and Engineering Sciences*, vol. 454, no. 1971, pp. 903–995, 1998.
- [43] J. Gilles, "Empirical wavelet transform," *IEEE Transactions on Signal Processing*, vol. 61, no. 16, pp. 3999–4010, 2013.
- [44] J. Gilles, G. Tran, and S. Osher, "2D empirical transforms. Wavelets, ridgelets, and curvelets revisited," *SIAM Journal on Imaging Sciences*, vol. 7, no. 1, pp. 157–186, 2014.

- [45] A. Gunduz and J. C. Principe, "Correntropy as a novel measure for nonlinearity tests," *Signal Processing*, vol. 89, no. 1, pp. 14–23, 2009.
- [46] I. Santamaria, P. Pokharel, and J. Principe, "Generalized correlation function: Definition, properties, and application to blind equalization," *IEEE Transactions on Signal Processing*, vol. 54, no. 6, pp. 2187–2197, 2006.
- [47] W. Liu, P. Pokharel, and J. Principe, "Correntropy: Properties and applications in non-Gaussian signal processing," *IEEE Transactions on Signal Processing*, vol. 55, no. 11, pp. 5286–5298, 2007.
- [48] S. Patidar, R. B. Pachori, and U. R. Acharya, "Automated diagnosis of coronary artery disease using tunable-Q wavelet transform applied on heart rate signals," *Knowledge-Based Systems*, vol. 82, pp. 1–10, 2015.
- [49] J. F. Box, "Guinness, Gosset, Fisher, and small samples," *Statistical Science*, vol. 2, no. 1, pp. 45–52, 1987.
- [50] U. R. Acharya, K. S. Vidya, D. N. Ghista, W. J. E. Lim, F. Molinari, and M. Sankaranarayanan, "Computer aided diagnosis of diabetic subjects by heart rate variability signals using discrete wavelet transform method," *Knowledge-Based Systems*, vol. 81, pp. 56–64, 2015.
- [51] M. H. Dunham, *Data Mining: Introductory and Advanced Topics*. Prentice Hall PTR, USA, 2002.
- [52] S. Patidar, R. B. Pachori, and N. Garg, "Automatic diagnosis of septal defects based on tunable-Q wavelet transform of cardiac sound signals," *Expert Systems with Applications*, vol. 42, no. 7, pp. 3315–3326, 2015.
- [53] R. Sharma, R. B. Pachori, and U. R. Acharya, "Application of entropy measures on intrinsic mode functions for the automated identification of focal electroencephalogram signals," *Entropy*, vol. 17, no. 2, pp. 669–691, 2015.
- [54] R. Sharma and R. B. Pachori, "Classification of epileptic seizures in EEG signals based on phase space representation of intrinsic mode functions," *Expert Systems with Applications*, vol. 42, no. 3, pp. 1106–1117, 2015.
- [55] R. B. Pachori, R. Sharma, and S. Patidar, "Classification of normal and epileptic seizure EEG signals based on empirical mode decomposition," in *Complex System Modelling and Control Through Intelligent Soft Computations*, 2015, vol. 319, pp. 367–388.
- [56] V. Bajaj and R. B. Pachori, "Classification of seizure and nonseizure EEG signals using empirical mode decomposition," *IEEE Transactions on Information Technology in Biomedicine*, vol. 16, no. 6, pp. 1135–1142, 2012.
- [57] R. B. Pachori and S. Patidar, "Epileptic seizure classification in EEG signals using second-order difference plot of intrinsic mode functions," *Computer Methods and Programs in Biomedicine*, vol. 113, no. 2, pp. 494–502, 2014.
- [58] J. A. K. Suykens and J. Vandewalle, "Least squares support vector machine classifiers," *Neural Processing Letters*, vol. 9, no. 3, pp. 293–300, 1999.

References

- [59] J. Suykens, T. V. Gestel, J. D. Brabanter, B. D. Moor, and J. Vandewalle, *Least squares support vector machines*. World Scientific Publication, Singapore, 2002.
- [60] S. Li, W. Zhou, Q. Yuan, S. Geng, and D. Cai, “Feature extraction and recognition of ictal EEG using EMD and SVM,” *Computers in Biology and Medicine*, vol. 43, no. 7, pp. 807–816, 2013.
- [61] A. H. Khandoker, D. T. H. Lai, R. K. Begg, and M. Palaniswami, “Wavelet based feature extraction for support vector machines for screening balance impairments in the elderly,” *IEEE Transactions on Neural Systems and Rehabilitation Engineering*, vol. 15, no. 4, pp. 587–597, 2007.
- [62] M. Zavar, S. Rahati, M. R. Akbarzadeh-T, and H. Ghasemifard, “Evolutionary model selection in a wavelet-based support vector machine for automated seizure detection,” *Expert Systems with Applications*, vol. 38, no. 9, pp. 10 751–10 758, 2011.
- [63] L. Zhang, W. Zhou, and L. Jiao, “Wavelet support vector machine,” *IEEE Transactions on Systems, Man, and Cybernetics, Part B: Cybernetics*, vol. 34, no. 1, pp. 34–39, 2004.
- [64] A. T. Azar and S. A. El-Said, “Performance analysis of support vector machines classifiers in breast cancer mammography recognition,” *Neural Computing and Applications*, vol. 24, no. 5, pp. 1163–1177, 2014.
- [65] R. Kohavi, “A study of cross-validation and bootstrap for accuracy estimation and model selection,” in *International Joint Conference on Artificial intelligence*, vol. 14, no. 2, 1995, pp. 1137–1145.
- [66] K. Dragomiretskiy and D. Zosso, “Variational mode decomposition,” *IEEE Transactions on Signal Processing*, vol. 62, no. 3, pp. 531–544, 2014.
- [67] Y. Hu, F. Li, H. Li, and C. Liu, “An enhanced empirical wavelet transform for noisy and non-stationary signal processing,” *Digital Signal Processing*, vol. 60, pp. 220–229, 2017.
- [68] J. Lian, Z. Liu, H. Wang, and X. Dong, “Adaptive variational mode decomposition method for signal processing based on mode characteristic,” *Mechanical Systems and Signal Processing*, vol. 107, pp. 53–77, 2018.
- [69] K. Dragomiretskiy and D. Zosso, “Two-dimensional variational mode decomposition,” in *Energy Minimization Methods in Computer Vision and Pattern Recognition*, 2015, pp. 197–208.
- [70] R. Keys, “Cubic convolution interpolation for digital image processing,” *IEEE Transactions on Acoustics, Speech, and Signal Processing*, vol. 29, no. 6, pp. 1153–1160, 1981.
- [71] R. C. Gonzalez and R. E. Woods, *Digital Image Processing (3rd Edition)*. Prentice-Hall, Inc., USA, 2006.

- [72] K. Zuiderveld, *Graphics Gems IV*. Academic Press Professional, Inc., USA, 1994, ch. Contrast Limited Adaptive Histogram Equalization, pp. 474–485.
- [73] M. Mookiah, U. R. Acharya, R. J. Martis, C. K. Chua, C. Lim, E. Ng, and A. Laude, “Evolutionary algorithm based classifier parameter tuning for automatic diabetic retinopathy grading: A hybrid feature extraction approach,” *Knowledge-Based Systems*, vol. 39, pp. 9–22, 2013.
- [74] U. R. Acharya, M. R. K. Mookiah, J. E. Koh, J. H. Tan, S. V. Bhandary, A. K. Rao, H. Fujita, Y. Hagiwara, C. K. Chua, and A. Laude, “Automated screening system for retinal health using bi-dimensional empirical mode decomposition and integrated index,” *Computers in Biology and Medicine*, vol. 75, pp. 54–62, 2016.
- [75] A. Pharwaha and B. Singh, “Shannon and non-shannon measures of entropy for statistical texture feature extraction in digitized mammograms,” in *World Congress on Engineering and Computer Science*, vol. 2, 2009.
- [76] M. K. Biswas, T. Ghose, S. Guha, and P. K. Biswas, “Fractal dimension estimation for texture images: A parallel approach,” *Pattern Recognition Letters*, vol. 19, no. 3–4, pp. 309–313, 1998.
- [77] B. B. Chaudhuri and N. Sarkar, “Texture segmentation using fractal dimension,” *IEEE Trans. Pattern Anal. Mach. Intell.*, vol. 17, no. 1, pp. 72–77, 1995.
- [78] U. R. Acharya, S. V. Sree, L. Saba, F. Molinari, S. Guerriero, and J. S. Suri, “Ovarian tumor characterization and classification using ultrasound—a new online paradigm,” *Journal of Digital Imaging*, vol. 26, no. 3, pp. 544–553, 2013.
- [79] M. Sharma, R. B. Pachori, and U. R. Acharya, “A new approach to characterize epileptic seizures using analytic time-frequency flexible wavelet transform and fractal dimension,” *Pattern Recognition Letters*, vol. 94, pp. 172–179, 2017.
- [80] S. Maheshwari, R. B. Pachori, and U. R. Acharya, “Automated diagnosis of glaucoma using empirical wavelet transform and correntropy features extracted from fundus images,” *IEEE Journal of Biomedical and Health Informatics*, vol. 21, no. 3, pp. 803–813, 2017.
- [81] I. Kononenko, “Estimating attributes: Analysis and extensions of relief,” in *European Conference on Machine Learning*, 1994, pp. 171–182.
- [82] K. Kira and L. A. Rendell, “The feature selection problem: Traditional methods and a new algorithm,” in *Association for the Advancement of Artificial Intelligence*, vol. 2, 1992, pp. 129–134.
- [83] U. R. Acharya, M. R. K. Mookiah, J. E. Koh, J. H. Tan, K. Noronha, S. V. Bhandary, A. K. Rao, Y. Hagiwara, C. K. Chua, and A. Laude, “Novel risk index for the identification of age-related macular degeneration using radon transform and dwt features,” *Computers in Biology and Medicine*, vol. 73, pp. 131–140, 2016.

- [84] K. Townsend, G. Wollstein, D. Danks, K. Sung, H. Ishikawa, L. Kagemann, M. Gabriele, and J. Schuman, "Heidelberg retina tomograph 3 machine learning classifiers for glaucoma detection," *British Journal of Ophthalmology*, vol. 92, no. 6, pp. 814–818, 2008.
- [85] T. Ojala, M. Pietikainen, and T. Maenpaa, "Multiresolution gray-scale and rotation invariant texture classification with local binary patterns," *IEEE Transactions on Pattern Analysis and Machine Intelligence*, vol. 24, no. 7, pp. 971–987, 2002.
- [86] C. J. Burges, "A tutorial on support vector machines for pattern recognition," *Data Mining and Knowledge Discovery*, 1998.
- [87] A. Feltane, G. F. B. Bartels, J. Gaitanis, Y. Boudria, and W. Besio, "Human seizure detection using quadratic rényi entropy," in *6th International IEEE/EMBS Conference on Neural Engineering (NER)*, 2013, pp. 815–818.
- [88] R. Sharma, R. B. Pachori, and U. R. Acharya, "Application of entropy measures on intrinsic mode functions for the automated identification of focal electroencephalogram signals," *Entropy*, vol. 17, no. 2, pp. 669–691, 2015.
- [89] U. R. Acharya, U. Raghavendra, H. Fujita, Y. Hagiwara, J. E. Koh, T. J. Hong, V. K. Sudarshan, A. Vijayanathan, C. H. Yeong, A. Gudigar, and K. H. Ng, "Automated characterization of fatty liver disease and cirrhosis using curvelet transform and entropy features extracted from ultrasound images," *Computers in Biology and Medicine*, vol. 79, pp. 250–258, 2016.
- [90] U. R. Acharya, S. V. Sree, M. M. R. Krishnan, F. Molinari, R. Garberoglio, and J. S. Suri, "Non-invasive automated 3d thyroid lesion classification in ultrasound: A class of thyroscanTM systems," *Ultrasonics*, vol. 52, no. 4, pp. 508–520, 2012.
- [91] S. Maheshwari, R. B. Pachori, V. Kanhangad, S. V. Bhandary, and U. R. Acharya, "Iterative variational mode decomposition based automated detection of glaucoma using fundus images," *Computers in Biology and Medicine*, vol. 88, pp. 142–149, 2017.
- [92] U. Raghavendra, S. V. Bhandary, A. Gudigar, and U. R. Acharya, "Novel expert system for glaucoma identification using non-parametric spatial envelope energy spectrum with fundus images," *Biocybernetics and Biomedical Engineering*, vol. 38, no. 1, pp. 170–180, 2018.
- [93] S. J. Pan and Q. Yang, "A survey on transfer learning," *IEEE Transactions on Knowledge and Data Engineering*, vol. 22, no. 10, pp. 1345–1359, Oct 2010.
- [94] A. Krizhevsky, I. Sutskever, and G. E. Hinton, "Imagenet classification with deep convolutional neural networks," in *Advances in Neural Information Processing Systems 25*, 2012, pp. 1097–1105.
- [95] S. Maheshwari, V. Kanhangad, R. B. Pachori, S. V. Bhandary, and U. R. Acharya, "Automated glaucoma diagnosis using bit-plane slicing and local binary pattern techniques," *Computers in Biology and Medicine*, vol. 105, pp. 72–80, 2019.

References

- [96] B. S. Kirar and D. K. Agrawal, “Computer aided diagnosis of glaucoma using discrete and empirical wavelet transform from fundus images,” *IET Image Processing*, vol. 13, no. 1, pp. 73–82, 2019.
- [97] L. van der Maaten and G. Hinton, “Visualizing high-dimensional data using t-sne,” *Journal of Machine Learning Research*, vol. 9, pp. 2579–2605, 2008.

List of Publications

Journals (accepted):

1. S. Maheshwari, R. B. Pachori and U. R. Acharya, "Automated Diagnosis of Glaucoma Using Empirical Wavelet Transform and Correntropy Features Extracted From Fundus Images," *IEEE Journal of Biomedical and Health Informatics*, vol. 21, no. 3, pp. 803-813, May 2017.
2. S. Maheshwari, R. B. Pachori, V. Kanhangad, S. V. Bhandary, U. R. Acharya, "Iterative variational mode decomposition based automated detection of glaucoma using fundus images," *Computers in Biology and Medicine*, vol. 88, pp. 142-149, 2017.
3. S. Maheshwari, V. Kanhangad, R. B. Pachori, S. V. Bhandary, U. R. Acharya, "Automated Glaucoma Diagnosis Using Bit-plane Slicing and Local Binary Pattern Techniques," *Computers in Biology and Medicine*, vol. 105, pp. 72-80, 2018.

Journals (in submission):

1. S. Maheshwari, V. Kanhangad, R. B. Pachori, "CNN-based approach for automated glaucoma diagnosis employing transfer learning and LBP-based data augmentation," to be submitted to *Biomedical Signal Processing and Control*.